DOCTOR OF PHILOSOPHY

Wave-induced liquefaction processes in marine sediments

Xu, Haixia

Award date:
2012

Awarding institution:
University of Dundee

DOCTOR OF PHILOSOPHY

Wave-induced liquefaction processes in marine sediments

Haixia Xu

2012

University of Dundee

Wave-Induced Liquefaction Processes in Marine Sediments

Haixia Xu

A thesis submitted for the degree of Doctor of Philosophy

Division of Civil Engineering

The University of Dundee

October 2012

TABLE OF CONTENTS

LIST OF FIGURES

LIST OF TABLE

NOTATION

a_j	Amplitude of the displacement of the jth layer, $j = 1, \cdots, N$
a_n	Amplitude of the nth wave component
A_j	Coefficients, $j = 1, \cdots, N$
B_j	Coefficients, $j = 1, \cdots, N$
C_j	Coefficients, $j = 1, \cdots, N$
c_v	Coefficient of Consolidation
D	Seabed depth
D_j	Coefficients, $j = 1, \cdots, N$
d_j	Thickness of the *j*th liquefied soil layer, $j = 1, \cdots, N$
$\dot{e}_{ij}$	Deviator part of strain rate tensor
Ei_j	Coefficients, $i = 1, \cdots, 4$, $j = 1, \cdots, N$
f	Mean accumulation pore pressure
g	Acceleration due to gravity
G	Elastic modulus

H	Wave height
H_z	Mean wave height
H_{rms}	Root mean squared wave height
h	Fluid depth
K	Hydraulic conductivity of soil
k	Darcy coefficient of permeability
k_z	Soil permeability
k_n	Related by the dispersion relation
K_0	Coefficient of earth pressure at rest
L	Wave length
M	Constrained modulus
M_D	Constrained modulus at the bottom of seabed
M_j	Coefficients, $j = 1, \cdots, N$
N	Total number of layers
N_r	Size of random smaple
N_s	Scale factor

N/N_l	Ratio of cyclic loading to the cyclic number to liquefaction
P	Probability density
$\hat{\mathrm{p}}_\mathrm{j}$	Dynamic wave pressure of the jth layer, $j = 1, \cdots, N$
P_b	Wave pressure at the seabed surface
R	Soil material parameters
t	Time
T	Wave period
u_0	Amplitude of fluid pressure oscillation just over the soil surface
$\tilde{u}_0$	Fluid pressure oscillation at the level of the soil surface ($z = 0$)
$\tilde{u}_L$	Fluid pressure oscillation at the depth of the liquefaction front ($z = z_L$)
$\hat{u}_j$	Horizontal velocity
u_e	Wave-induced pressure fluctuation
$u_e^{(1)}$	Oscillatory pore pressure
$\bar{u}_e^{(1)}$	Average of oscillatory pore pressure
$u_e^{(2)}$	Residual pore pressure

u_g	Pore pressure due to cyclic loading
$\widehat{w}_j$	Vertical velocity
x	Spatial co-ordinate in the horizontal direction
X_r	Variable uniformly distributed on (0, 1)
z	Spatial co-ordinate in the vertical direction
z_L	Location of the liquefaction front
Δz	Increment of sub-liquefied soil layer
α	Soil material parameters
β	Soil material parameters
η	Elevation of water surface
θ	Shape factor
σ_{ij}	Deviator part of stress tensor
σ_0'	Vertical effective stress of soil
σ_h'	Horizontal effective stress
σ_v'	Vertical effective stress at a given location
σ_{v0}'	The initial vertical effective stress

σ_x'	Effective normal stresses in the x-direction
σ_y'	Effective normal stresses in the y-direction
σ_z'	Effective normal stresses in the z-direction
σ_{zm}'	Distribution is compressed by the rigid bottom
$\Delta\sigma_v$	Wave-induced change in the total vertical stress
γ_s	Unit weight of soil
γ_w	Unit weight of water
γ'	Submerged unit weight of the soil
λ_j	Coefficients, $j = 1, \cdots, N$
μ	Dynamic viscosity after yield
μ'	Equivalent Newtonian viscosity
μ_a	Apparent viscosity
ν_j	Kinematic viscosity
ρ_1	Density of the seawater layer
ρ_j	Density of the *j*th liquefied soil layer
κ	Current wave number

κ_r	Real part of the wave number
κ_i	Imaginary part of the wave number
κ_0	Initial wave number
μ_e	Dynamic Viscosity
μ_1	Viscosity of liquefied soil in the viscoelastic state
μ_2	Viscosity of liquefied soil in the viscoplastic state
μ_r	Poisson's ratio
τ	Maximum cyclic shear stress of the soil
τ_y	Yield stress
χ	Cyclic stress ratio
υ^p	Plastic volumetric strain
ω	Angular frequency
ω_n	Related by the dispersion relation
Φ	Partial drainage factor
ξ	Wave loading cycle
$\Delta\xi$	Increment of wave loading cycle

ϕ_n	Phase
$\lvert\Pi_e\rvert$	Objective of the deformation-rate tensor

ACKNOWLEDGEMENTS

It took nearly four years to finish this thesis. Many people have given me precious helps without which I cannot go thought this hard work.

My deepest appreciation goes to my supervisor, Prof. Ping Dong. During these years, his enthusiasm and broad view on research has had a great impact on me. I've learned a lot from him, both in the disciplines of research and about the attitude for life. He provided me great deal of freedom to explore different ideas, and at the same time gave me constructive suggestions, guidance, and encouragement. It was a distinct privilege for me to work with Prof. Dong.

I extend a special thank to Prof. Dongsheng Jeng. I experienced a frustration in my second year. Fortunately, Prof. Dongsheng Jeng gave me not only much comments in seminar discussion using his sharp mind but also some useful materials which are really instructive for my study. Prof. Jeng has also become a good source for advice on all aspects of my work.

I would like to especially express my gratitude to my husband Huijie Zhang who has been a colleague for five years and is a constant source of help and great ideas. He is always closest to my joys and sorrows and always standing by me.

I am indebted to my parents, without whose tolerance, love and support I would undoubtedly have failed to get this far. My mother and mother-in-law took turn to be the baby sitter which helped me go through this tough time.

The author gratefully acknowledges the financial support provided to her by the University of Dundee and Chinese Scholarship Council.

I hereby certify that the work embodied in this dissertation is the result of original research and has not been submitted for a higher degree to any other University or Institution

_____

Haixia Xu

ABSTRACT

An investigation for seabed liquefaction induced by progressive water waves is vital for the protection of marine structures from damage to the structure foundations. The residual liquefaction in sedimentary seabed has been found to be of progressive nature and experiments have also demonstrated that the liquefied soil behaves as a visco-elastic-plastic material. Building on the previous research, this work develops various numerical models to re-examine the key factors which influence the progressive liquefaction processes.

To investigate the effect of randomness of wave height on seabed liquefaction, ensemble modelling approach is adopted in a two-layer inviscid fluid flow model, whereby the liquefied soil is treated as inviscid heavy fluid. Probabilistic study of soil liquefaction processes indicates that the random wave-induced liquefaction depth is much larger than that corresponding to regular waves with Equivalent Wave Height. The larger liquefaction depth in random waves is shown to be due to the fact that the highest waves rather than average waves in the wave series tend to dominate the liquefaction extent. It is also shown that the time needed for liquefaction to reach the bottom of investigated domain can vary considerably in the case of random wave time series. The longer period of low waves between the large waves will delay the time for the maximum liquefaction depth to be reached within the simulation time considered. The current design practice, which is entirely based on the regular wave models, can under-estimate the liquefaction depth and lead to unsafe design. It is recommended that the evaluation of liquefaction potential due to random waves should be based on the

appropriate extreme values in the wave height distribution rather than average values such as significant wave height or root-mean-square wave height.

Secondly, a two-layer viscous fluid model representing a visco-elastic-plastic liquefied soil is constructed. The upper seawater and liquefied soil were treated as viscous fluid and described by the linearized Navier-Stokes and continuity equations. Simulation results confirmed that shear stress solved from infinite seabed solution can lead to significant errors and underestimate the liquefaction depth. The viscosity of liquefied soil computed by the present model reveals a clear state change, i.e., from viso-elastic stage to visco-plastic stage, due to the increasing deformation rate of liquefied soil layer. The strain rate dependent viscosity can influence the liquefaction process relative to constant viscosity although not very strongly. Deeper liquefaction is more likely to take place in shallower water under the same wave loading. Smaller soil permeability prevents residual pore pressure dissipation and consequently enhances the liquefaction.

Finally, the two-layer viscous model is extended to a multi-layer model in order to investigate the effect of stratification of liquefied soil layer. It is found that the liquefaction depth estimated using the N-layer model is sensitive to water content, which is contrary to that predicted by the two-layer model. The continuously increasing liquefied soil density is found to overcome the numerical difficulty in achieving a convergent viscosity. The predicted liquefied soil viscosity, liquefaction depth and interface wave amplitude are all different from that predicted by constant water content model. The sensitivity of liquefaction to both wave and soil parameters are enhanced by the stratification of liquefied soil viscosity and density. The thickness of seabed is also found to affect liquefaction but the trend is not monotonic. There seems to be a critical

seabed thickness, at which the effect of seabed thickness on liquefaction reverses. Below the critical thickness, the liquefaction depth is smaller due to the relatively short drainage distance in thinner seabed but beyond the critical thickness, increasing seabed thickness damps the wave energy and consequently prevents the liquefaction. Seabed liquefaction is very sensitive to the soil plastic model parameters contained in the residual pore pressure build-up equation. Therefore, a reliable procedure for quantifying these parameters is extremely important.

PUBLICATION

Xu, Haixia and Dong, Ping. 2010. A probabilistic analysis of random wave-induced liquefaction. *Ocean Engineering*. 38, 860–867.

Chapter 1 Introduction

Over the world, a large part of population and industry are concentrated around the coast and more and more exploration activities take place in coastal area and offshore. Marine structures such as breakwaters, pipeline, oil drilling platforms, and wind turbines are constructed to protect coastal community, facilitate marine transport or to generate energy.

Exposed to fluctuations of water pressure induced by water waves, the sea floor around or beneath marine structures will undergo periodic shear deformation. Along with the rearrangement of soil grains, the pore water will be compressed. As a result, the pore water pressure builds up in the case of an 'undrained' soil, which leads to reduction in the soil shear strength. When the water wave is sufficiently severe and under specific conditions of seabed properties, the soil may even be liquefied if the accumulated pore pressure exceeds the overburden pressure. In this situation, the soil grains will become unbound and completely free from frictional contact, and the soil will move like a liquid (Sumer *et al.*, 1999) under the prevailing current and wave actions. In coastal engineering, wave-induced liquefaction has been identified as a major cause for damage in marine structures as the result of foundation failures (Zen *et al.*, 1991; Sakai, 1999; Gomyo, 1995) due to submarine flow slides, liquefaction of loosely packed backfills around underwater pipelines and instability around the toe of composite or offshore breakwaters as illustrated in Fig. 1.1.

The topic of wave-induce seabed response and liquefaction in seabed has receive numerous attentions since the 1970's. The cyclic loading due to ocean waves has been confirmed to cause liquefaction to the seabed (Bjerrum, 1973; Lee and Focht, 1975).

The mechanism of wave-induced liquefaction is theoretically established by a number of researchers, for example Nataraja and Gill (1983), Okusa (1985) as well as Zen and Yamazaki (1990). Most investigations into the response of soil to progressive wave loading were carried out by means of numerical analyses and centrifuge tests (Sassa and Sekiguchi, 1999; Sassa and Sekiguchi, 2001; Sassa *et al.*, 2001), and model scale wave flume tests (Sumer *et al.*, 1999; Sumer *et al.*, 2004; Teh *et al.*, 2003). There are also some analytical approximations available for predicting liquefaction potential of a free seabed namely, without being disturbed by marine structures.

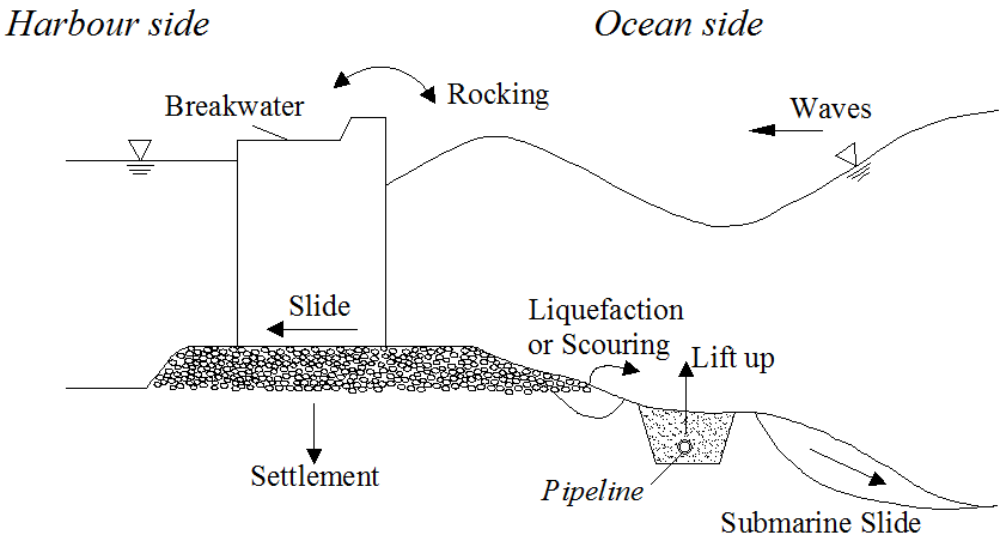

Fig. 1.1 Geo-hazards in water fronts associated with ocean waves

Despite these studies, the understanding of wave-seabed interaction is still far from complete. For example, it is well known that after the occurrence of liquefaction the liquefied soil loses its supporting power but it remains unclear how the fluid-like liquefied seabed may affect the physics of wave-seabed interaction. Takahashi *et al.* (1994) and Kioka *et al.* (1998) have proposed that artificially liquefied zones of sand or mud could be used to dampen out destructive energy of water waves in harbours. Sassa and Sekiguchi (1999) and Sassa *et al.* (2001) have demonstrated the progressive nature

of liquefaction under progressive waves using both experimental and numerical approaches. The theoretical model proposed by Sassa *et al*. (2001) was an extension of Lamb's two-layer fluid system theory (Lamb, 1932). The completely liquefied soil was assumed to be inviscid fluid above and below which are a clear water layer and a sub-liquefied (not become liquefied yet) seabed layer which was modelled by a poro-elastoplastic model. Liu *et al.* (2009) also took the sea water-liquefied soil as a two-layer system. However, they employed the linearized Navier-Stokes equation to describe the fluid system and prescribed a constant viscosity for the liquefied soil layer. Furthermore, the wave-induced shear stress in seabed was computed by a finite depth seabed model rather than an infinite depth seabed in Sassa *et al*. (2001). In the aforementioned works, it was shown that wave energy is dissipated as the liquefaction front advances downward. Therefore, the liquefied soil desires a rational modelling method by which both the wave behaviour and the pressure exerted by the completely liquefied soil on sub-liquefied seabed can be estimated more accurately.

However, the existing investigations into the wave-induced seabed liquefaction based on two-layer fluid system are restricted to regular waves. In reality, the gravity water waves are always random. The random wave induced soil response and the final liquefaction depth frequently exceed the results under the corresponding representative regular waves and the same soil characteristics. Moreover, the two-layer fluid system employed in the current literature assumes the liquefied soil layer as an inviscid or viscous fluid with a constant viscosity neglecting the fact that the liquefied soil not only behaves like a heavy viscous fluid its viscosity also varies with the rate of shear strain in a way similar to the response of rate-dependent fluid mud to wave actions. Therefore it is instructive to apply the concepts and rheological models originated from studying

fluid mud to the modelling of liquefied soil. Finally, as the strain rate of liquefied soil tends to change with depth the method of two-layer system is clearly unable to account for these changes and the impact of this approximation on the predicted liquefaction processes need be quantified.

This thesis aims to examine the aspects mentioned above in the seabed liquefaction caused by progress waves. To address the problem a clear knowledge on ocean wave characteristics, wave-induced seabed response (pore pressure and shear stress), properties of liquefied soil and wave-seabed interaction analysis is required.The thesis is organized as followings:

In Chapter 2, some previous works related to such issues are briefly reviewed.

In Chapter 3, a two-layer inviscid fluid system for wave-liquefied soil is constructed. After Sassa *et al.* (2001), analytic solution to wave-induced shear stress for infinite poro-elastic seabed and the same residual pore water storage equation for excess pore pressure build-up are employed. The model is verified by comparison with the wave tank centrifuge tests on progressive sandy seabed liquefaction.

In Chapter 4, based on ensemble modelling method, a probabilistic analysis of progressive liquefaction is performed. By performing multiple runs of a liquefaction model using randomly generated wave series from a given wave distribution, the liquefaction depth and time are determined in the form of probability distributions so as to reveal the variability and uncertainties involved in wave-induced liquefaction. Prediction of pore pressure, seabed shear stress and wave pressure are calculated using the model established in chapter 3.

In Chapter 5, the inviscid two-layer fluid system for wave-liquefied soil is re-examined. To account for viscosity of liquefied soil, a viscous two-layer fluid system based on governing equations of linearized Navier-Stokes equations is constructed. Liquefied soil is modelled using a visco-elasto-plastic rheological model and wave-induced soil shear stress is obtained from analytical solution for a finite thick seabed to give a more accurate description.

In Chapter 6, two-layer viscous wave model in chapter 4 is extended to multi-layer system. A semi-analytical method is used to solve the system whose number of layer automatically increases as liquefaction front advances down. Thereby, variation of shear strain rate and viscosity of liquefied soil along depth is accommodated. Based on the newly established model, a series of comparison with two-layer model are carried out.

Chapter 7 is the concluding chapter of the thesis. In this chapter the major findings of the investigation are summarised and recommendations for further work are given.

Chapter 2 Literature Review

2.1 Wave-Induced liquefaction

2.1.1 Regular and irregular progressive waves

From a physical viewpoint, there exists a great variety of water waves, which can be generated by wind, moving ship, earthquake or submarine explosions. The scope of this study is limited to the progressive wave. A simplest regular progressive wave is the kind of wave that can be defined by a sine or cosine function. In order to fully specify a regular wave we need its amplitude, a, its wavelength, *L*, its period, *T* as characteristic parameters. The elevation of water surface depends on the two variables position, *x*, and time, *t* can be expressed as

$$\eta(x,t) = a\sin\left(\frac{2\pi}{T}t - \frac{2\pi}{L}x\right) \tag{2.1}$$

The water motion can be described by fluid mechanics, primarily consisting of mass, momentum and energy conservation equations. For the small amplitude wave, a series of linearization or other simplicity are acceptable and the associated theory is termed as 'linear wave theory'.

Random wave

However, the sea is never regular. It is not simply of the uniform waves, of constant height and length, proceeding in a steady and reliable sequence. Rather, a true sea is a random phenomenon where the wave characteristics such as height, length, are continually changing (Walter, 1968).

Mathematical treatment of random wave

Longuet-Higgins (1952) proposed the classical sea spectra simplified solutions with an attempt to decompose the complex sea into simple wave elements. His basic idea was random wave can be taken as a collection of a great number of regular waves with different characteristics. For illustration, combining of a small number of regular waves with different lengths and heights is shown in Fig. 2.1.

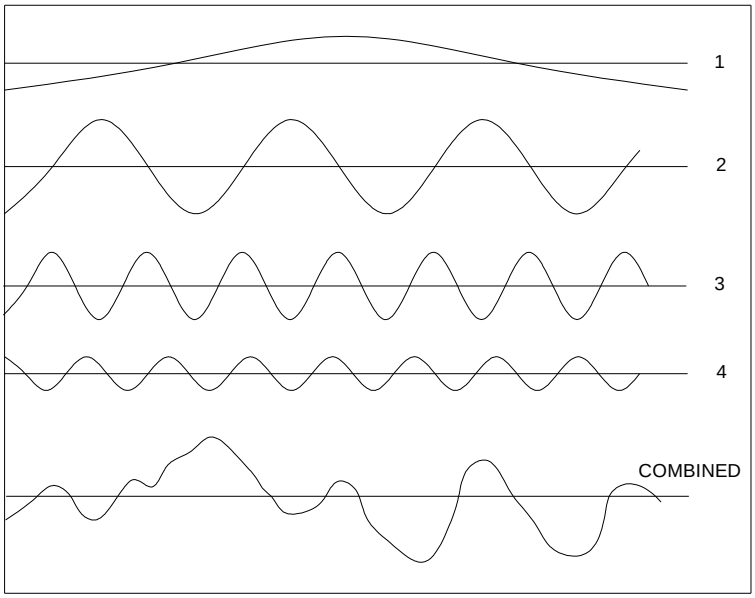

Fig. 2.1 Wave pattern combining four regular waves (Walter, 1968)

Mathematically, the random linear progressive waves are interpreted as the superposition of a series of regular waves as

$$\eta(x,t) = \sum_{n=1}^{N} a_n \sin(\omega_n t - k_n x + \phi_n) \tag{2.2}$$

where a_n is the amplitude of the nth wave component, k_n is the wave number , ω_n is wave angular frequency. k_n and ω_n are related by the dispersion relation and ϕ_n is the phase.

In fact, the most distinctive feature of the irregular sea is that it has no set pattern that can be repeated from one interval to any other. But its total energy must necessarily be the sum of the energies of all the regular waves that make up the wave surface. Thus, the intensity of the sea is characterized by its total energy. By virtue of the so-called "wave spectrum", it can be known how the total energy of the sea is distributed over the frequency range of the wave components. The wave heights can be predicted by various statistical methods.

Seabed response to random waves

To date, only a few studies have been carried out to consider the variations of soil responses inside the marine sediments under random wave loadings. Sumer *et al.* (1999) performed experimental tests to investigate the effect of irregular wave on soil response, and they found that the process of build-up of pore pressure in irregular waves occurs in much the same way as in the case of the regular wave.

Regarding the dynamic response of seabed caused by random wave, Wang *et al.* (2005) developed a finite element model to numerically examine the effects of random waves on the wave-induced pore pressure and effective stress based on the dynamic model of Zienkiewicz *et al.* (1980). Recently, Liu and Jeng (2006) developed an analytical solution for the random wave-induced soil response (instantaneous pore pressure and soil stress) within an infinite soil thickness. Difference on the soil response

between regular and random wave loadings, together with the effects of several soil characteristics, was investigated.

Later, Liu and Jeng (2007) continued to establish a semi-analytical solution for the random wave-induced soil response within a finite seabed thickness. The influence of random wave loading on the soil response is investigated by comparing with the corresponding representative regular wave results through a parametric study, which includes the effect of the degree of saturation, soil permeability, wave height, wave period and seabed thickness. The distribution of quantities of seabed response was found to have the similar trend for random wave and regular wave. However, the magnitude in results of random wave is much larger. The random wave can lead to a deeper liquefaction depth than regular wave. The effect of soil thickness was also conducted which demonstrated that the pore pressure at seabed bottom increases due to the presence of impervious boundary and a larger maximum effective normal stress was also observed for the finite thick seabed than the infinite seabed. However, further increasing the seabed thickness will obtain soil responses approaching the results under the infinite soil depth.

Ensemble modelling method

Ensemble prediction is a technique in which several forecasts are produced based on an ensemble of different realisations of model variables, such as initial conditions, forcing and/or model parameters. The advantages of an ensemble prediction system (EPS) are well known. Amongst its benefits are greater reliability for the solution, the generation of several possible predictions and the probabilities associated with them as well as the capability of predicting extreme events.

The ensemble method employed in atmospheric modelling has an analogue for ocean wave prediction. From the present point of view, a wave ensemble prediction system (WEPS) can essentially go in two directions to produce ensemble solutions or members: (a) to create perturbations of the forcing wind fields or/and (b) to generate perturbations of the initial wave spectrum. These approaches are described and analysed by Farina (2002) and some potential benefits of wave ensemble prediction are presented in Janssen (2000) and Hoffschildt *et al.* (1999) where the ECMWF wave ensemble forecasts, operational since June 1998, are employed.

There are two well-known methods to describe irregular waves: spectral analysis and wave train analysis. Although the spectral approach is currently the most mathematically appropriate approach for analyzing a time-dependent, three-dimensional sea surface record, it is exceedingly complex and at present few measurements are available that could fully tap the potential of this method. Alternatively, wave-by-wave (wave train) analysis can be used to treat irregular waves. In this analysis method, a time-history of the sea surface at a point is used and statistics of the record are developed. The undulation in the time-history of the surface must be divided into a series of segments, which will then be considered as individual waves. The height and period of each wave will be measured. Once this is done for every segment of the record, statistical characteristics of the record can be estimated, and the statistics of the record are compiled. Two of the most important parameters necessary for adequately quantifying a given sea state are characteristic height and characteristic period. In general, probability density for the wave period is narrower than that of wave height, and the spread lies mainly in the range 0.5 to 2.0 times the mean wave period.

In this study, the probabilistic analysis of wave-induced seabed liquefaction is based on the wave train analysis. Instead of representing random waves by a single representative wave, an ensemble of different wave heights and their sequences are used to carry out multiple numerical predictions. Since the time of concern is very short (at the scale of minutes), the wave period is assumed to be constant.

2.1.2 **Liquefaction mechanisms and prediction**

Liquefaction definition

Seabed liquefaction is the state where the seabed has lost all its structural strength due to the increase of effective stress or excess pore pressure due to cyclic loading. The seabed behaves as a heavy liquid with no rigidity, and can therefore flow. When water waves propagate in the ocean, significant dynamic wave pressures and variation of stress within sea floor could be generated. With excess pore pressure and diminishing vertical effective stress, part of the seabed may become unstable or even liquefied. Once liquefaction occurs, the unbounded soil particles are vulnerable to be carried away as a fluid by any prevailing bottom current or mass transport subjected to the action of ocean waves (Jeng, 2003).

Liquefaction mechanisms

As observed by Zen and Yamazaki (1990) and Nago *et al.* (1993) in the laboratory and field measurements, wave-induced liquefaction can occur by two different mechanisms depending on the pore pressure: oscillating (momentary) liquefaction and residual (progressive) liquefaction (see Fig. 2.2). The oscillating liquefaction occurs when the oscillating excess pore pressure exceed the critical value. It is always accompanied by the amplitude damping and phase lag in the pore pressure. The residual

liquefaction is caused by the residual pore pressure (build-up of the excess pore pressure) due to tendency of seabed to contract under cyclic wave loading. This type of soil liquefaction is similar to that caused by earthquakes (Seed and Rahman, 1978). The oscillating liquefaction is more important for unsaturated marine sediment and deep water region while the residual liquefaction prevails for the relatively shallower water and large wave (Jeng *et al.*, 2007a) .

A typical time history of wave-induced pore pressure is illustrated in Fig. 2.2.

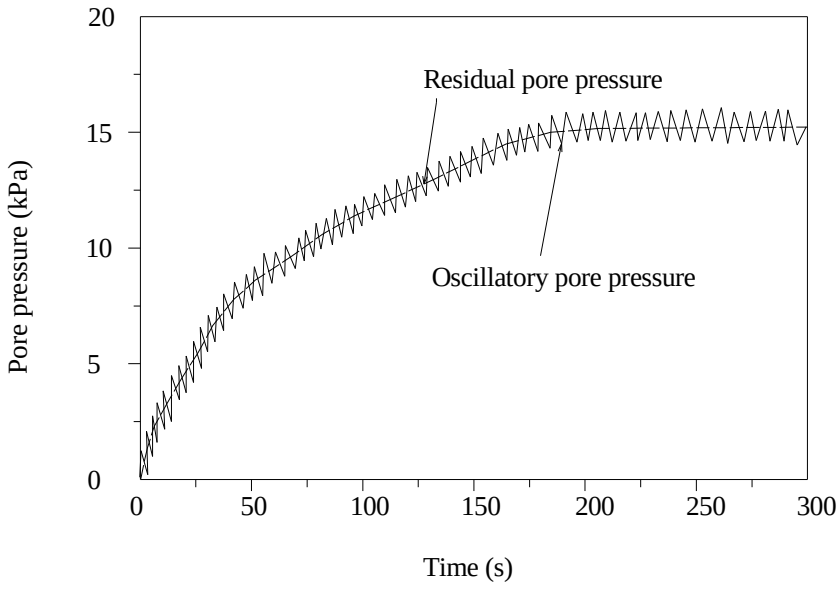

Fig. 2.2 Schematic illustration of wave-induced pore pressure in seabed

Liquefaction criteria

There exist mainly two different criteria that have been used to define the transient liquefied state. The first one is based on the concept of effective stress, as given by Okusa (1985) for 2D cases, in which a liquefied state is reached when the vertical effective normal stress is greater than the submerged weight of the soil deposits. This criterion was extended to the 3D case by Tsai (1995) as

$$\frac{1}{3}\left[-(\gamma_s-\gamma_w)(1+2K_0)z-\left(\sigma_x'+\sigma_y'+\sigma_z'\right)\right]\leq 0 \tag{2.3}$$

where $\gamma_s$and γ_w are the unit weight of soil and water, σ_x', σ_y' and σ_z' are the effective normal stresses in the x-, y-, and z-direction, respectively. K_0 is the coefficient of earth pressure at rest and z is the vertical coordinate (upward positive with the original located at surface of seabed) .

The second criterion is based on the concept of excess pore pressure, as suggested by Zen and Yamazaki (1990) for the 2D case. Liquefaction is assumed to take place when the geostatic pressure is less than the wave-induced effective mean normal stress. This was modified by Jeng (1997) to the 3D case as

$$\frac{1}{3}\left[(\gamma_s-\gamma_w)(1+2K_0)z+\left(P_b-u_e^{(1)}\right)\right]\leq 0 \tag{2.4}$$

In which P_b is the wave pressure at the seabed surface and $u_e^{(1)}$ is the wave-induced oscillatory pore pressure.

Jeng (1997) examined the above two criteria for several different cases, together with the field data from Zen *et al.* (1991). He concluded that the criterion suggested by Okusa (1985) and Tsai (1995) may only be suitable for a seabed with large thickness. He also found that no liquefaction occurs in a saturated seabed unless at least one of the following conditions is met: very shallow water or large wave or seabed with very low permeability.

Regarding the criteria for residual liquefaction, Sassa *et al.* (2001) employed a simple one as

$$\frac{u_e^{(2)}}{\sigma_0'} = 1 \tag{2.5}$$

where σ_0' is the initial vertical effective stress of soil and $u_e^{(2)}$ the residual pore pressure.

Pre-liquefaction: potential

Nataraja *et al.* (1980) suggested a simplified procedure for ocean wave-induced liquefaction analysis and concluded that the existing data on cyclic shear strength of liquefiable soils under seismic loading could be used to estimate the cyclic shear strength under wave loading conditions.

Then, Nataraja and Gill (1983) summarized the features of the simplified procedure for ocean wave-induced liquefaction analysis and examined the procedure by using data from four projects.

Ishihara *et al.* (1984) proposed a methodology for evaluating the magnitude of cyclic stress and wave-induced liquefaction on the basis of design storm parameters. For some typical several storm conditions, liquefaction in a medium dense deposit of sand with 70% relative density (i.e., the ratio of the difference between the void ratios of a cohesionless soil in its loosest state and existing natural state to the difference between its void ratio in the loosest and densest states.) could extend down to a depth of 17.7 m at a location of 14 m water depth.

Umehara *et al.* (1985) proposed a method to evaluate liquefaction resistance for partially drained conditions (somewhere between the perfectly undrained and drained idealized conditions). Their results indicated that soil strength increases owing to partial

drainage and the strength can be well represented by the relative density and a coefficient of drainage effect.

Maeno *et al.* (1989) compared the empirical formula for wave-induced liquefaction proposed by Maeno and Hasegawa (1987) with the theoretical solution of Yamamoto *et al.* (1978). They pointed out that the liquefaction depth predicted by the theoretical solution was considerably less than that given by the empirical formula for small waves. But an agreement was observed for the case of large waves (wave steepness greater than 0.2). They also concluded that wave height and period play an important role in the wave-induced liquefaction.

Tsotsos *et al.* (1989) developed a numerical model for the evaluation of pore pressure generation and liquefaction potential in the sea floor due to cyclic wave action. The analysis included the development of both transient and residual pore-water pressures, and the simultaneous partial pressure dissipation. They have shown that soil permeability had a significant influence on pore-water pressure generation and liquefaction because high permeability prevented the development of excess pore-water pressure.

Sakaki *et al.* (1992), using Mei and Foda's (1981) boundary layer approximation, examined the wave-induced momentary liquefaction. They concluded that the excess pore pressure increases as the soil stiffness $G\beta$ increases. The maximum liquefaction depth reached around half of the wave height in surf zone conditions.

Rahman (1991) investigated two mechanisms of wave induced liquefaction for the non-cohesive sediments. Employing Okusa (1985)'s criteria for liquefaction, it was

found that liquefaction potential would increase with increasing wave period. Lower degree of saturation tends to increase the chance of transient liquefaction.

Jeng and Zhang (2005) and Zhang and Jeng (2005) established an integrated three-dimensional model, incorporating a wave model and a soil model, to investigate the wave-induced liquefaction potential in the Gold Coast region in Australia. Both non-breaking and breaking waves were considered in their model. Jeng *et al.* (2007a) derived an analytical solution for residual pore pressure for homogenous, isotropic and infinite seabed. Based on the solution, a parametric analysis was performed to verify the applicable range of two liquefaction mechanisms. They concluded that the residual mechanism is more important for large waves or shallower water. Using the criterion of liquefaction as shown in Eq. (2.5), Jeng *et al.* (2007a) proposed a formula to predict the liquefaction depth:

$$z = z_L = \frac{2}{\lambda}\sqrt{\frac{1}{2} - \frac{\gamma'(1+2K_0)c_v\lambda^2}{6A}} \tag{2.6}$$

Note that Eq. (2.6) is only valid under the condition of $\frac{1}{2} - \frac{\gamma'(1+2K_0)c_v\lambda^2}{6A} > 0$; otherwise, it means no liquefaction occurs. Based on this formula, a numerical example for the prediction of maximum liquefaction depth (z_L) is presented in Fig. 2.3, where ε is the ratio of amplitude of the oscillatory pore pressure and residual pore pressure. In the example, the relative water depth (h/L) varies from shallow water ($h/L = 0.05$) to intermediate water ($h/L = 0.3$). As the water depth increases, the maximum wave steepness for inducing soil liquefaction will increase, which will enhance the

liquefaction potential. The figure also indicates that the maximum residual liquefaction depth will increase as the wave steepness increases.

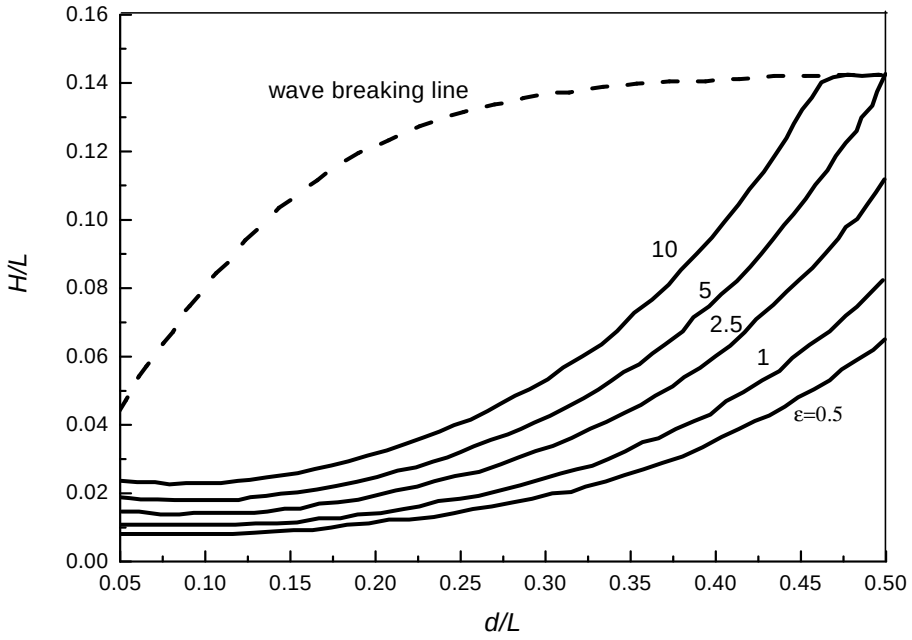

Fig. 2.3 Distribution of critical wave steepness versus relative water depth for various values of amplitude ratios (Jeng *et al.*, 2007a)

Post-liquefaction: progressive nature

All the aforementioned models focus on the liquefaction potential estimation without considering the effects of liquefied seabed on the whole liquefaction procedure. Sassa and Sekiguchi (1999) carried out a series of centrifuge wave tank tests. They found residual liquefaction only takes place when a critical cyclic stress ratio is reached. The threshold ratio for progressive wave is lower than for standing wave. Moreover, the wave-induced liquefaction of the sand beds was of a progressive nature. Sassa *et al.* (2001) modelled the liquefied soil as heavy inviscid fluid and used a system of two-layer fluid overlying the sub-liquefied seabed to simulate the wave-seabed interaction. The numerical model demonstrated the progressive nature of residual liquefaction

processes and well reproduced the final liquefaction depth as measured in Sassa and Sekiguchi (1999). Furthermore, the decreasing wave number during the liquefaction process indicated the wave energy is more effectively damped out with the liquefaction front advances downward. This demonstrated the influence of completely liquefied soil on the development and final depth of liquefaction. However, when determining the stress ratio, Sassa *et al.* (2001) adopted an analytical solution of wave-induced shear stress for infinite thickness poro elastic seabed. This could lead to significant errors. Another weakness of the model is that the assumption of liquefied soil as a heavy inviscid fluid fails to capture the viscosity property of liquefied soil, which has been proven in experiments.

2.2 Wave-induced seabed response

As stated in the liquefaction mechanism, the wave-induced pore pressure is a dominant factor in the assessment of liquefaction. In turn, the build-up of residual pore pressure depends on the dynamic shear stress caused by the cyclic wave loading. Herein, the previous researches for the seabed response to water wave, i.e., shear stress and pore pressure are reviewed first.

2.2.1 Wave-induced stress in seabed and oscillatory pore pressure

Theoretical development

Numerous wave-seabed interaction models have been developed with various assumptions since the 1940's. They evolve from liquid flow and deformation un-coupled model to coupled model with or without consideration of accelerations due to

fluid and soil motion. In this subsection, the theoretical development of wave-induced seabed stress and oscillatory pore pressure modelling is briefly summarized.

Based on the assumptions of a rigid, permeable sandy seabed, un-coupled models have been proposed as the first approximation in the area of wave-seabed interaction. When the pore fluid is considered to be incompressible, the equations governs the storage of fluid is the Laplace's equation, or diffusion equation with including of the compressible pore water.

Based on a linear wave theory, Putnam (1949) presented a simple solution for an isotropic porous seabed of finite thickness. They concluded that seepage of pore fluid can result in a significant loss of wave energy. Liu (1973) employed the uncoupled model of Laplace's equation to simulate the flow in a permeable bed and determined the damping rate for an infinite seabed. The viscous effect of the boundary layer was incorporated. Nakamura *et al.* (1973) and Moshagen and Torum (1975) proposed the diffusion equation for pore water conservation. Moshagen and Torum (1975) found that the inclusion of pore fluid compressibility significantly alter the vertical seepage forces acting on the soil. However, the relative compressibility of the pore fluid appeared somewhat unrealistic (Prevost *et al.*, 1975) which impaired the validity of their conclusion.

The approach of un-coupled modelling ignores the compressibility of seabed and its deformation due to un-coupling of pore-fluid motion and soil motion. Furthermore, these approaches provide no information on the soil effective stresses and soil displacements in the seabed.

In 1970's, the second type of models for the wave-induced seabed response emerged. It is based on the assumption of compressible pore fluid and soil, but ignoring the accelerations due to pore fluid and soil motion. Biot consolidation equation (Biot, 1941) and storage equation (Verruijt, 1969) were adopted to describe the force balance and fluid motion, respectively. The methodologies in solving the governing equations can be summarized into three classes: direct analytical solution, boundary-layer approximation and numerical modelling.

The direct analytical approach was first developed by Yamamoto *et al.* (1978) and Madsen (1978), among which Madsen (1978) considered a hydraulically anisotropic and unsaturated porous bed, whilst Yamamoto *et al.* (1978) studied an isotropic medium. Both considered only an infinite thickness of soil bed. Under elastic conditions, Okusa (1985) used the compatibility equation and reduced the governing equation of Yamamoto *et al.* (1978) to a fourth-order differential linear equation. He stated that the wave-induced soil response depended only on the wave conditions, not on the soil characteristics for a fully saturated and isotropic sandy seabed of infinite thickness. The conclusion may not hold for the seabed of finite thickness (Gatmiri, 1990; Jeng and Hsu, 1996). Jeng and Hsu (1996) provided a closed form solution for the shear stress and pore pressure induced by a progressive wave for a saturated poro-elastic seabed of finite thickness. Based on the solution, Jeng and Hsu (1996) compared the relative difference between the solutions for infinite and finite bed thickness and foundthat when using an infinite bed the relative errors in pore pressure, wave-induced effective stresses and soil displacements are significant. For a general layered seabed, Rahman *et al.* (1994) proposed a semi-analytical analysis because the analytical solution is not able to provide

a closed-form solution. The other shortcoming of the direct analytical solution is the complicated mathematical presentations especially for a finite thickness seabed.

An alternative approximation, the boundary-layer approximation, was proposed by Mei and Foda (1981). The basic principle of the approach is to divide the whole soil domain into inner and outer regions. Full solution is provided in the inner region, namely, near the seabed surface of more interest while a simplified solution is obtained in the outer region. This approximation can obtain a more acceptable solution for saturated seabed with low permeability under low frequency waves than other cases (Hsu *et al.*, 1993).

Numerical methods, including finite difference method, finite element method and boundary element method, are more powerful to address the complex situations for one or multiple-dimensional seabed.

Madga (1990) developed a one-dimensional finite difference model for the wave-induced pore pressure in a nearly saturated sandy bed. He concluded that the time phase in pressure generation depends mainly on the degree of saturation, compressibility of the soil skeleton and soil permeability. Zen and Yamazaki (1990) established a finite difference model for a single layer of porous seabed. Gatmiri (1990) developed a finite element model for the wave-induced effective stresses and pore pressure in an isotropic and saturated permeable seabed. He found that there exists a critical bed thickness about 0.2 times the wavelength, for which the horizontal movement of the soil skeleton reach a maximum. Further, the soil response of a finite thickness is affected by soil characteristics as well as wave even when the seabed is hydraulically isotropic and saturated. At the lateral boundaries, the vertical displacement and pore pressure are

prescribed to be zero ignoring a phase lag in soil response in a fully saturated seabed of finite thickness (Jeng and Hsu, 1996). Probably, this is the reason why the general trend of pore pressure distribution versus the seabed thickness in Gatmiri (1990) was found to be inconsistent (Jeng and Hsu, 1996). Thomas (1995) developed a one-dimensional finite element method for a two layered unsaturated seabed. The results suggested that the stiffer sediment in the top layer dominated the response of the bottom layer in a two-layer seabed. Jeng and Lin (1996) extended the model for a non-homogeneous seabed with the permeability and shear modulus varying with depth. Jeng and Lin (1997) went on to examine the influence of non-linear wave components on the soil response. The combined effect of cross-anisotropic soil behaviour and non-homogeneous soil characteristics on the wave-induced soil response was examined by Jeng and Lin (1999). For the application to the seabed with a structure, a two-dimensional finite element model was developed (Jeng, 2003) by employing the principle of repeatability for the specification of lateral boundary conditions.

To account for the dynamic of soil motion, Zienkiewicz *et al.* (1980) proposed a one-dimensional so-called u−p approximation for waves propagation over porous media based on the Biot's poro-elastic theory (Biot, 1956). In addition to inertial terms due to the soil motion, Jeng and Rahman (2001), Jeng and Cha (2003) included the inertial terms related to the pore fluid motion and investigated the effects of dynamic soil behaviour on the wave-induced soil response through a two-dimensional analysis. Usually, the dynamic solutions are lengthy and complex which limits its application in engineering practice.

All aforementioned poro-elastic models and small strain modelling framework are only applicable to small deformations, which are an idealized condition. To address the large deformation occurred under the action of a storm for soft seabed, poro elasto plastic models are required to provide a better estimation of the soil response. However, due to the complexity in constitutive relationship and moving boundary, only a few investigations have been published (Sekiguchi et al., 1995; Yang and Poorooshasb, 1997; Li et al., 2002).

Physical modelling

Theoretical investigations usually involve some assumptions to simplify the real physical problem to make the mathematical equations tractable. To test model validity or to help construct a conceptual model for a specific process of seabed and wave interaction, physical models have often been carried out. In general, three different experimental approaches have been used: wave tank experiments, geotechnical compressive tests, and centrifugal wave modelling.

There have been numerous investigations for the wave-induced pore pressure based on water tank experiments. Sleath (1970) and Tsui and Helfrich (1983) used wave tank to measure the phase lag of wave-induced pore pressure. Based on second-order Stokes wave theory, Maeno and Hasegawa (1985) proposed an empirical equation for the wave-induced pore pressure in sandy beds. The empirical pore pressure equation was expressed as a function of the wave steepness and two experimental parameters, which are depended on the permeability of the bed. Demars and Vanover (1985) measured the wave-induced pore pressure and stresses in a sandy bed. Their laboratory data verified the elastic theories in estimating the total vertical and horizontal stresses in a sandy bed,

where dilation of the grain matrix is small. Furthermore, their theoretical solution of the total stress for a seabed of infinite depth was shown to provide a lower bound for stresses in a sandy bed of finite depth.

Apart from the examination of wave-induced pore pressure, wave tank was also employed in studying the phenomenon of seabed liquefaction under wave loading. Tzang (1992) conducted a series of wave tank experiments and demonstrated the relationship between the build-up pore pressure and fluidization in a soft seabed. Sumer (2005) used wave tank to investigate sinking and floating of pipeline in liquefied sand. The results of the experiments showed that the density of liquefied soil varies with depth, which is consistent with Hwang *et al.* (2006). Therefore, it is not appropriate to treat the viscosity of the liquefied soil a constant throughout the depth.

Although wave tank experiments have been commonly used by coastal engineers, they generally lack the necessary accuracy required in determining soil parameters. In order to achieve a better estimation of soil characteristics, compressive test needs to be performed. Both wave tank experiments and compressive tests have the scale problem under one gravity acceleration environment and therefore the results obtained in the wave tanks may not be easily extrapolated to prototype conditions.

Centrifugal wave modelling is a newly developed experimental approach, which allows the experiments are conducted under N times gravitational acceleration. The centrifugal experiment can provide the spatial distribution of both soil response and water pressure. Sekiguchi and Phillips (1991) and Phillips and Sekiguchi (1992) may have been the first to conduct wave experiments in a centrifuge and develop the fundamental framework of the centrifugal wave experiments. Their experimental data

has been widely cited for the verification of theoretical results. Sassa and Sekiguchi (1999) and Sassa and Sekiguchi (2001) further improved the controls of experimental environment, which enables the progressive nature of wave-induced liquefaction to be clearly observed. However, the wave experiment in centrifuges remains be a challenging task with both preparation technique and wave generation system requiring much more investigations.

2.2.2 **Wave-Induced residual pore pressure modelling**

There are two groups of method for describing the build-up of residual pore pressure that are widely employed. The first group was developed by incorporating into the one-dimensional consolidation equation a source term, which relates the development of pore water pressure to the number of load cycles in simple shear tests. The corresponding analytical solution has been proposed and discussed (McDougal et al., 1989; Cheng et al., 2001; Jeng et al., 2007b). The second group was firstly proposed by Sassa and Sekiguchi (1999) involving the considerison of plastic volumetric strain change in the incompressible fluid storage equation. Although both groups of method are based on the fluid continuity equations they differ significantly in dealing with the relationship between pore pressure generation and cyclic plasticity of the soil. A brief description of each method is given below.

Modified consolidation model

The residual pore pressure ($u_e^{(2)}$) in a homogeneous, isotropic soil can be derived from the one dimensional consolidation equation

$$\frac{\partial u_e^{(2)}}{\partial t} = c_v \frac{\partial^2 u_e^{(2)}}{\partial z^2} + f \tag{2.7}$$

in which c_v is the coefficient of consolidation, related to shear modulus, G and hydraulic conductivity, K by

$$c_v = \frac{2GK(1-\mu_r)}{\gamma_w(1-2\mu_r)} \tag{2.8}$$

where $\mu_r$is Poisson's ratio and γ_w the unit weight of pore water.

On the right hand side of Eq. (2.7), the source term, f is the mean accumulation pore pressure associated with the surface water waves. There are both linear and nonlinear mechanisms of pore pressure generation (Jeng *et al.*, 2007b) which are valid for linear wave and nonlinear wave, respectively (Jeng, 2008). For the linear mechanism, the source term is expressed as

$$f = \frac{\partial}{\partial t}\left(\sigma_0' \frac{N}{N_l}\right) \tag{2.9}$$

where N/N_l represent the ratio of cyclic loading to the cyclic number to liquefaction, can be obtained by (De Alba *et al.*, 1976)

$$\frac{u_g}{\sigma_0'} = \frac{1}{2} + \frac{1}{\pi}\sin^{-1}\left[2\left(\frac{N}{N_l}\right)^{1/\theta} - 1\right] \tag{2.10}$$

or

$$\sin\left(\frac{\pi u_g}{2\sigma_0'}\right) = \left(\frac{N}{N_l}\right)^{1/2\theta} \tag{2.11}$$

where, u_g and σ_0' are the pore pressure generation due to cyclic loading and effective overburden, respectively; and θ is the shape factor. The analytical approximations are available for the finite, shallow and deep seabed (Jeng, 2008).

Modified storage equation model

The storage equation relevant to the poro-elastoplastic soil with contractancy may be described as follows (Sassa and Sekiguchi, 1999):

$$\frac{\partial u_e^{(2)}}{\partial(\omega t)} = \frac{k}{m_v \mu \omega}\frac{\partial^2 u_e^{(2)}}{\partial z^2} + \frac{1}{m_v}\frac{\partial \in_{vol}^{(2)}}{\partial(\omega t)} \tag{2.12}$$

where k is the coefficient of permeability and $\in_{vol}^{(2)}$ is the plastic component of soil volumetric strain increment (Appendix A). Let $\xi = \omega t/2\pi$, the second term on RHS is the temporal rate of plastic volume change which can be describe as (Sassa *et al.*, 2001)

$$\frac{dv^p}{d\xi} = \beta \exp(-\beta\xi) v_\infty^p(\chi) \tag{2.13}$$

where ω can be divided from both sides for convenience of comparison and v^p, v_∞^p and χ are plastic volumetric strain, plastic volumetric strain as time approaching infinity and ratio of shear stress and initial vertical effective stress, respectively. The derivation is detailed in Appendix A.

The coefficient of compressibility of the soil skeleton, m_v is related to c_v by

$$m_v = \frac{k}{c_v \mu} \tag{2.14}$$

Therefore, the above storage equation becomes

$$\frac{\partial u_e^{(2)}}{\partial t} = c_v \frac{\partial^2 u_e^{(2)}}{\partial z^2} + \frac{c_v \mu_r}{K} \frac{dv^p}{dt} \tag{2.15}$$

Therefore, it is obvious that 1) these two methods share the same assumptions of incompressibility of pore fluid and fully-saturated soil; 2) the only difference arises from the description of cyclic plasticity of the soil. Neither one is assumed to be superior to the other if the associated model constants are measured at the same accuracy level. In this study, the second model is adopted.

2.3 Behaviour of liquefied soil

Modelling of liquefied soil is crucial in predicting the progressive liquefaction. With the liquefaction front advances downward, the input wave energy is altered. Consequently, the chance of liquefaction for sub-liquefied seabed is influenced. There is no consensus on whether liquefied soil behaves like a solid or a liquid. Consequently, the commonly accepted constitutive model for a completely liquefied soil does not exist.

In the investigation of ground deformation induced by liquefied soil, some researchers assumed the liquefied soil behaves like a solid with significantly reduced stiffness given by a suitable post-liquefaction stress-strain relations (Finn et al., 1991; Aydan, 1995), whilst others took the view that the liquefied soil intrinsically behaves like a fluid because liquefaction reduces the stiffness of the soil to a negligible extent. For instance, Uzuoka *et al.* (1998) treated the liquefied soil as a Bingham fluid and carried out several numerical simulations and validated against experimental data. The shear stress-shear strain rate relationship of the Bingham model can be expressed as follows:

$$\tau = \mu\dot{\gamma} + \tau_{\mathrm{r}} \tag{2.16}$$

where τ is the shear stress, μ is the viscosity after yield, $\dot{\gamma}$ is the shear strain rate and τ_{r} is the yield strength, i.e., the minimum undrained strength. When applying Bingham fluid model to the liquefied soil, Uzuoka *et al.* (1998) expressed the Bingham viscosity by an equivalent Newtonian viscosity μ'as

$$\mu = \begin{cases} \mu + \dfrac{\tau_r}{2\dot{\gamma}} = \mu + \dfrac{R_r \cdot P}{2\dot{\gamma}} & \dot{\gamma} \neq 0 \\ \infty & \dot{\gamma} = 0 \end{cases} \tag{2.17}$$

In which,

$$\dot{\gamma} = \sqrt{(1/2)\dot{e}_{ij}\dot{e}_{ij}} \tag{2.18}$$

where R_{r} is the residual strength ratio and: *P* is the second invariant of the deviatoric strain rate tensor. The Bingham model appears to provide a realistic description of the post-liquefaction behaviour, both in terms of residual shear strength and viscosity exhibited by such kind of material (Montassar and Buhan, 2006). Sawicki and Mierczyński (2009) carried out experiments to measure the dynamic viscosity of liquefied soil based on the assumption of Newton viscosity fluid model without residual shear strength.

Other significant contribution was made by Hamada and Wakamatsu (1998), who carried out experiments to determine the characteristics of liquefied soil and ground displacements using shaking table tests on liquefied subsoil models. They concluded that during ground flow before earthquake motion cease, liquefied soil behaves as a pseudoplastic fluid. It is a group of non-Newtonian fluids in which the viscosity

coefficient decreases as the shear strain rate increases (Hamada and Wakamatsu, 1998). The relationship between the shear stress, τ, and shear strain rate, , for such fluids, can be expressed with:

$$\tau = \mu_0 \dot{\gamma} / (1 + \dot{\gamma} / \dot{\gamma}_{\mathrm{r}}) \tag{2.19}$$

where the apparent viscosity coefficient η given by:

$$\mu = \mu_0 / (1 + \dot{\gamma} / \dot{\gamma}_{\mathrm{r}}) \tag{2.20}$$

where μ_0 is the initial viscosity coefficient; $\dot{\gamma}$ is the shear strain rate when the secant viscosity becomes equal to $\mu_0/2$, which is usually referred to as the reference shear strain rate.

Hwang *et al.* (2006) performed sinking ball and pulling bar tests to measure the viscosity of liquefied sand and confirmed that the liquefied sand behaved as non-Newtonian fluid, whose viscosity decreased with increasing shear strain rate. Further, a extensive review on the dynamic viscosity of liquefied soil was conducted with the main results as shown in Fig. 2.4 and Table 2.1. Hamada and Wakamatsu (1998) made extensive earthquake-induced ground displacement investigation, and concluded that liquefied soil behaves as a pseudo plastic fluid during ground flow; however, it returns to behaves as a solid body as stiffness recovers due to dissipation of pore water. In other words, there exists a property transition for liquefied soil from relatively rigid viscous to purely viscous fluid. No comprehensive model is available in the existing literature that accounts for this important phase change.

At this point, it is worthwhile to review briefly the rheological models for a closely related material, i.e., fluid mud. There have been three types of rheological models for

fluid mud: Viscous fluid, Viscoelastic model, Viscoplastic model and Viscoelastic-plastic model (Soltanpour and Samsami, 2011).

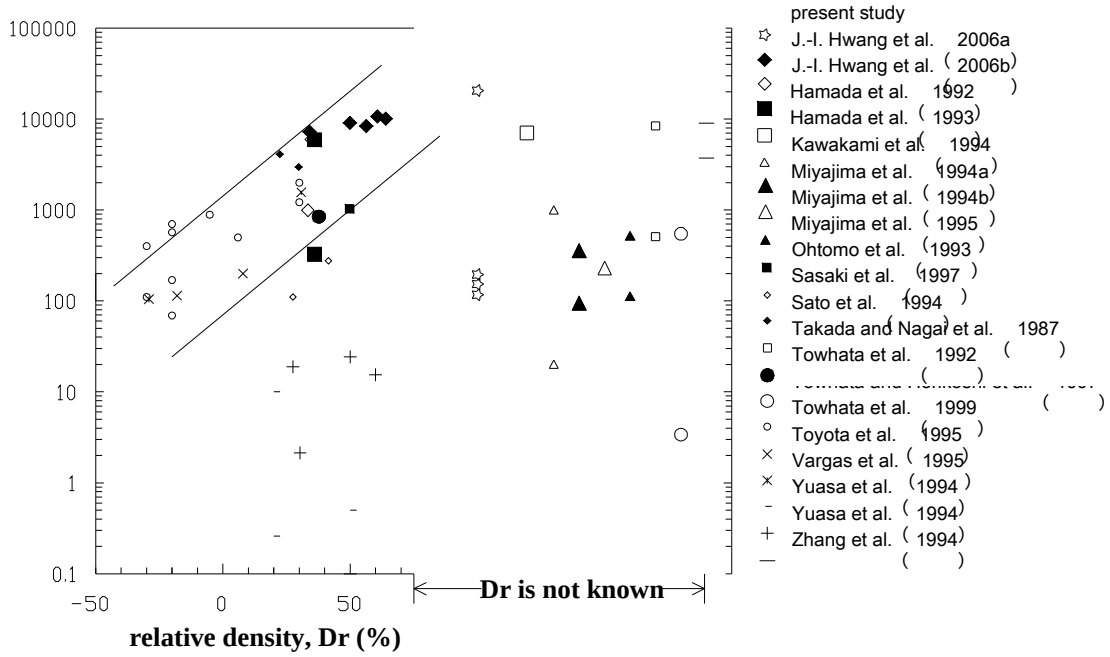

Fig. 2.4 Test results of viscosity values of liquefied soil in literature (Hwang *et al.*, 2006)

Table 2.1 Tests and method of liquefaction in assessing liquefied soil viscosity (Hwang *et al.*, 2006)

Researcher	**Type of test**	**Method of liquefaction**
Hwang *et al*.(2006a)	1 g, subsidence of sphere	Impact
Hwang *et al*.(2006b)	1 g, pulling cylindrical bar	Boiling
Hamada and *et al*.(1992)	1 g, pulling sphere	–

Hamada and *et al*.(1993)	1 g, pulling pipe, pile, sphere	–
Kawakami *et al*. (1994)	1 g, shaking table test	Shaking
Miyajima *et al*. (1994a)	1 g, subsidence of sphere	Shaking
Miyajima *et al*. (1994b)	1 g, pulling sphere	Boiling
Miyajima *et al*. (1995)	1 g, subsidence of sphere	Shaking
Ohtomo *et al*. (1993)	1 g, pulling sphere	Boiling
Sasaki *et al*. (1997)	1 g, subsidence of foundation	Shaking
Sato *et al*. (1994)	50 g, flow of slope	Shaking in centrifuge
Takada and Nagai (1987)	1 g, subsidence of sphere	Shaking
Towhata *et al*. (1992)	Analysis of the progress of lateral deformation of liquefied slopes	–
Towhata and Horikoshi(1997)	Prototype subsidence of building Foundation	1964 Niigata earthquake
Towhata *et al*. (1999)	1 g, pulling pipe	Shaking

Toyota (1995)	1 g, flow of slope	Impact
Vargas *et al*. (1995)	1 g, pulling pipe	Shaking
Yuasa *et al*. (1994)	1 g, pulling sphere	Shaking
Yuasa *et al*. (1994)	1 g, viscometer	Boiling
Zhang *et al*. (1994)	undrained triaxial test	–

Gade (1958) was probably the first researcher who used the viscous fluid mud constitutive model to analyze the dissipation of wave energy by a deformable mud bed. The stress for viscous fluids is represented as follows:

$$\sigma_{ij} = -p\delta_{ij} + 2\mu\dot{e}_{ij} \tag{2.21}$$

where p is the mean or the hydrostatic stress, μ is the dynamic viscosity, δ_{ij} is the Kronecker delta, and $\dot{e}_{ij}$ is the strain rate tensor. The apparent viscosity of a Newtonian viscous fluid can be defined as

$$\mu_a = \mu_m + \frac{\tau_y}{\frac{du}{dz}} \tag{2.22}$$

where μ_a is apparent viscosity, μ_m is the Bingham plastic viscosity and τ_y is yield stress. The apparent viscosity can be obtained through trial-and-error. Alternatively, fluid mud was modelled as viscoelastic materials which simultaneously display characteristics of both solids and fluids. The shear stress of these materials depends not only on the local strain rate, but also on its history. This memory effect results in an

elastic property of fluid, in addition to its viscosity property. Kelvin-Voigt model (Soltanpour and Samsami, 2011) is a representative viscoelastic model. The constitutive equation for the Kelvin-Voigt model is defined as

$$\sigma_{ij} = 2\mu\dot{e}_{ij} + 2Ge_{ij} \tag{2.23}$$

Bingham fluid model is acturally a simplest viscoplastic model. Bingham fluid mud model assumes the shear stress as (Kessel and Kranenburg, 1996):

$$\tau = \tau_y sign\left(\frac{\partial u}{\partial z}\right) + \mu_m \frac{\partial u}{\partial z} \quad \text{if} \quad |\tau| > \tau_y \tag{2.24}$$

where τ_y is the yield stress, μ_m is the Bingham plastic viscosity, and u is the velocity in X direction. By introducing a so-called "equivalent viscosity", Tsuruya *et al.* (1987) converted the Bingham fluid model into the viscous fluid model

$$\mu_e = \mu_m + \frac{\tau_y}{\sqrt{4|\Pi_e|}} \tag{2.25}$$

where $4|\Pi_e|$ is expressed as

$$4|\Pi_e| = 2\left(\frac{\partial u}{\partial x}\right)^2 + 2\left(\frac{\partial w}{\partial z}\right)^2 + \left(\frac{\partial u}{\partial z} + \frac{\partial w}{\partial x}\right)^2 \tag{2.26}$$

Huynh *et al.* (1990) and Jiang and Watanabe (1995) investigate the rheological behaviour of fluid mud and found that the mud exhibits a nearly visoelastic behaviour at low shear rate and a Bingham fluid behavior at high shear rate. Shibayama *et al.* (1989) introduced the viscoelastplastic (VEP) terminology to overcome the shortcoming of visoelastic and Bingham model. The constitutive equations are expressed as

$$\sigma_{ij} = 2\mu_e \dot{e}_{ij} \tag{2.27}$$

$$\mu_e = \begin{cases} \mu + \dfrac{iG}{\omega} & \left(\dfrac{1}{2}\sigma_{ij}\sigma_{ij} \le \tau_y^2\right) \\ \mu_m + \dfrac{\tau_y}{\sqrt{4|\Pi_e|}} & \left(\dfrac{1}{2}\sigma_{ij}\sigma_{ij} > \tau_y^2\right) \end{cases} \tag{2.28}$$

Regarding liquefaction prediction, Sassa *et al.* (2001) adopted an inviscid liquid model with a distinct density for liquefied soil in a theoretical model for predicting the behaviour of liquefied soil under fluid-wave loading, with the emphasis on the progressive nature of wave-induced liquefaction. Liu *et al.* (2009) took into account of the constant viscosity of liquefied soil in the analysis of wave-induced progressive liquefaction and found that the viscosity affect the prediction of final liquefaction depth under the same wave and seabed conditions. However, Sassa *et al.* (2001) has suggested that vertical displacement amplitude of liquefied soil layer increases dramatically in association with the downward propagation of the liquefaction front. It is expected that the shear strain rate will experience the same change. Since the viscosity depends on shear stress rate, it will be inevitably changed during the liquefaction front advancement. Therefore, it is necessary to adopt a more advanced liquefied soil rheological model.

It is increasingly being acknowledged today by researchers in geotechnical engineering that liquefied soil behaves as an incompressible fluid, displaying both viscous and residual strength properties (Towhata *et al.*, 1999; Montassar and Buhan, 2006). By virtue of the rheological similarities between fluid mud and liquefied soil, improvements in the rheological modeling of these two materials can be shared. In this study, the rheological model for fluidly mud proposed by Shibayama *et al.* (1989) is

used for comparison of progressive liquefaction process with Sassa *et al.* (2001) and Liu *et al.* (2009).

2.4 Wave-seabed interaction in post-liquefaction phase

Wave-seabed interaction modelling of pre-liquefied soil has been covered in the previous section. Herein, the focus is moved onto the post-liquefaction phase. Considering the similarities that exist in the behaviour of liquefied soil and fluid mud, the methods developed for wave-fluid mud interaction may provide valuable suggestions for the wave-liquefied soil interaction modelling.

The widely used models to investigate the dissipation of passing waves on soft mud are based on either a two-layer or a multiple layered fluid system in which both seawater and fluid mud are treated as fluid. The governing equations which are used to describe the motion of fluid are the linearized Navier-Stokes equations, neglecting the convective accelerations, and the continuity equation (MacPherson, 1980).

Dalrymple and Liu (1978) and Sakakiyama and Bijker (1988) developed a two-layer wave-mud interaction model to calculate the wave attenuation rate and mud mass transport. A viscous fluid rheological model was adopted for the fluid mud.

However, the two-layer modeling cannot capture the variation of characteristic mud properties along depth of fluid mud. Especially when shear stress and viscosity depends on vertical location, the vertical change of fluid properties may affect the eventual simulation results. To address this problem Tsuruya *et al.* (1987) proposed the so called multi-layer or N-layer fluid system. Maa and Mehta (1990) employed a viscoelastic mud rheological model in a multi-layer wave-mud interaction model. In addition to some laboratory experiments to investigate wave-mud interaction, An and Shibayama

(1993) developed a multi-layer numerical model assuming viscoelastoplastic behavior for fluid mud. Afterwards, Zhang and Zhao (1999) used a multi-layer model similar to the model of Maa and Mehta (1990) to study the wave-mud interaction. However, the restriction of constant viscosity of fluid mud layer was relaxed in their numerical simulations.

For both two-layer and multi-layer fluid systems, the boundary conditions consist of the kinematic boundary conditions at interfaces and free surface, zero horizontal and vertical velocities at the rigid bottom, the imposition of zero normal and tangential stresses at the water surface and the continuity of normal and tangential stresses across the interfaces. By the linearized NS equations subjected to the above boundary conditions, the wave attenuation rate, k_i, is calculated by this model (Soltanpour and Samsami, 2011) as well as the velocity components and fluid pressure.

In comparison with fluid mud modelling the literatures on wave-liquefied soil interaction modelling is very limited. To simulate the wave-liquefied soil interaction, Sassa *et al.* (2001) proposed a theoretical model for progressive liquefaction. The model was an extension of Lamb's (1932) two-layer fluid theory, by considering a layer of inviscid liquefied soil underneath seawater layer. Following the two-layer fluid model developed by Dalrymple and Liu (1978) for ocean waves over mud, Liu *et al.* (2009) treated both seawater and liquefied soil as viscous fluids and the laminar Navier–Stokes equations are used to describe the motion of the two-layer wave system.

2.5 Objectives of thesis

In view of the current research state in the investigation of seabed liquefaction induced by progressive wave, the specific objectives of this thesis are set as: 1) Examine

the seabed liquefaction under action of random progressive wave; 2) Investigate the effects of different liquefied soil rheological modelling on the progressive liquefaction process in the frame of two-layer viscous fluid system for wave-liquefied soil; 3) Establish a frame of multi-layer fluid system for wave-liquefied soil in modelling wave propagating over seabed.

Chapter 3 Two-layer Inviscid Fluid System Model

3.1 Introduction

Sassa and Sekiguchi (1999) demonstrated the progressive nature of fine grained sand liquefaction by centrifuge wave tank tests. By using a high-speed CCD camera, Miyamoto *et al*. (2000) found that the soil surface starts vibrating after liquefaction begins, and the amplitude of the vibration increased markedly as the advancement of the liquefaction front. Inspired by these phenomena, Sassa *et al*. (2001) proposed a two-layer inviscid fluid system to model the wave-induced soil liquefaction. They extended the two-layer fluid theory originally developed by Lamb (1932) by considering a layer of liquefied soil resting on a layer of poro-elastoplastic sediments. The simulation results were found to compare well with the experimental results from the centrifuge tests. In this chapter, we will describe the formulation of the model, basic assumptions on which the model is based and the implementation of the computational code generated. It will then go on to present a series of comparisons with centrifuge tests and results in Sassa *et al*. (2001) that were carried out to verify the model.

3.2 Outline of Sassa's two-layer liquefaction model

The model considers a given regular wave train with wave length L and wave period T propagating over a bed of cohesionless soil. Under certain conditions of wave and soil, the liquefaction may starts and its front will advance downwards. Let us suppose at a time instant t, the liquefaction front reaches down to a soil depth $z_L(t)$ as shown in Fig. 3.1. It consists of three layers: a seawater layer of a mass density ρ_1 above the soil surface $(0 \leq z \leq h)$, a liquefied soil layer of a mass density ρ_2 $(z_L \leq z \leq 0)$ (z_L is

negative), and a sub-liquefied soil layer ($-D \leq z \leq z_L$). Within the liquefied and the underlying sub-liquefied soil, the wave-induced pressure fluctuation u_e is the sum of the oscillatory and residual pore pressure as:

$$u_e = u_e^{(1)} + u_e^{(2)} \tag{3.1}$$

where $u_e^{(1)}$ and $u_e^{(2)}$ represent the oscillatory component and residual pore pressure , respectively. For the first component, $u_e^{(1)}$, its average value $\bar{u}_e^{(1)}$ over any wave cycle is zero by definition. The second component, $u_e^{(2)}$, is generated due to the soil cyclic plasticity, i.e., volumetric contraction under cyclic wave loading.

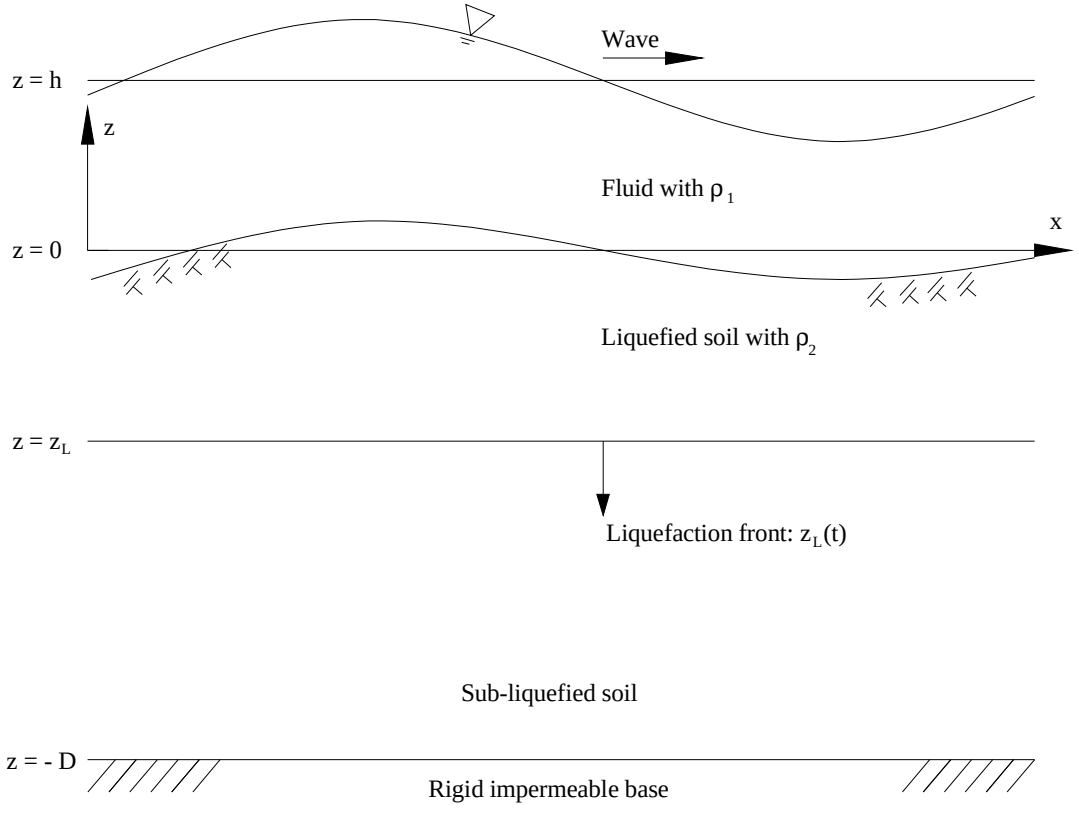

Fig. 3.1 Schematic representation of the liquefaction process in the experiments performed by Sassa *et al*. (2001)

In the solving procedure, the pore pressures are solved individually in the liquefied and sub-liquefied layer. The former is determined using the two-layer fluid system whilst the latter by the pore fluid storage equation. Sequent solving of the two layers provides the gradually advance of progressive liquefaction. In the following section, the formulations used for both layers are presented.

3.2.1 **Formulation for the upper sub-system**

Definition of the upper sub-system above the liquefaction front is shown in Fig. 3.2 illustrates the super part the model, here, named by 'upper sub-system', which is taken as an inviscid fluid system. Density of liquefied soil, ρ_2 is greater than that of seawater, ρ_1. As shown in Fig. 3.2 (b), the fluid pressure oscillation at the level of the soil surface ($z = 0$) is represent by $\tilde{u}_0(x,t)$ and fluid pressure at the interface between liquefied soil and sub-liquefied layer ($z = z_L$) by $\tilde{u}_L(x,t)$. Additionally, κ is the wave number, defined by $2\pi/L$, and the angular frequency of waves, ω defined by $2\pi/T$.

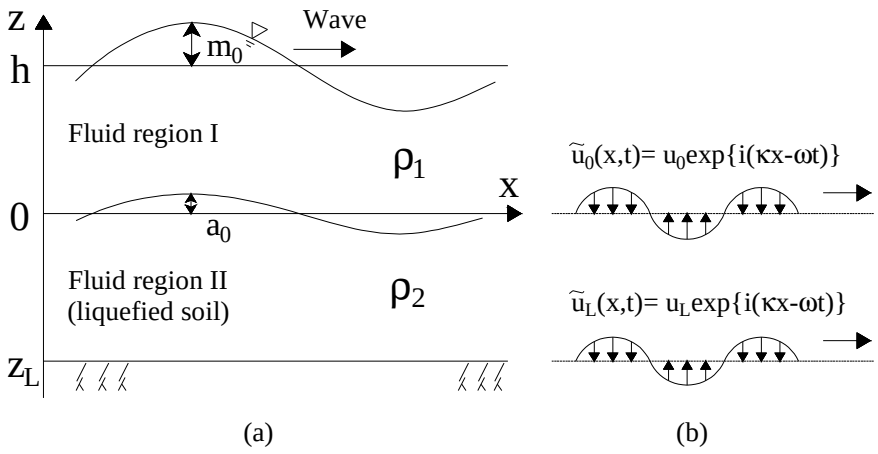

Fig. 3.2 Problem definition for the upper sub-system

The seabed is identified to become liquefied on the condition that the residual pore pressure build-up, $u_e^{(2)}$ reaches the effective overburden stress, σ'_{v0} at the location. A theoretical reason for this statement is explained below (Sassa and Sekiguchi, 1999).

For a one-dimensional problem considered here, assume σ'_v is the vertical effective stress at a given depth, and let $\Delta\sigma_v$ represent the total vertical stress variation induced by wave action at the same location. Therefore, we have

$$\sigma'_v = \sigma'_{v0} + (\Delta\sigma_v - u_e) \tag{3.2}$$

$$\sigma'_v = \sigma'_{v0} + \left(\Delta\sigma_v - u_e^{(1)} - u_e^{(2)}\right) \tag{3.3}$$

where σ'_{v0} denotes the initial vertical effective stress, which is expressed by $\sigma'_{v0} = -\gamma' z$ for $z \leq 0$. Here $\gamma'$is the submerged unit weight of the soil as defined by $(\rho_2 - \rho_1)N_s g$, where g is the gravitational acceleration and N_s represents the acceleration scale factor.

By definition of liquefaction, the seabed liquefies when the average local effective stress over a wave cycle equals zero ($\overline{\sigma'_v} = 0$) for a one-dimensional problem where the horizontal effective stress σ'_h is assumed to be zero. Since the time averages $\overline{\Delta\sigma_v}$ and $\bar{u}_e^{(1)}$over a wave cycle are zero, the liquefaction condition may be simply expressed as

$$\bar{u}_e^{(2)} = \sigma'_{v0} \tag{3.4}$$

Applying classic solution for the two-layer fluid system requires that the bottom ($z = z_L$) is rigid. This condition may be assumed to be satisfied in the sense that the vertical movement of the sub-liquefied soil layer below z_L should be of a negligible

magnitude compared with the vertical movement of the liquefied soil layer (Sassa *et al.*, 2001).

Once the location of liquefaction front, z_L is given, the classical theory of wave propagation in a two-layer fluid of finite thickness proposed by Lamb (1932) can be readily used to determine the amplitude of internal wave as well as the fluid pressure through the upper system. The detailed derivation refers to Appendix B of this thesis.

In Lamb's theory, the dispersion relationship for the two-layer fluid is written as

$$\left[1-\left(\frac{N_s g\kappa}{\omega^2}\right)^2\right] tanh(\kappa h) tanh(\kappa z_L) = \frac{\rho_2}{\rho_1}\left[1-\frac{N_s g\kappa}{\omega^2} tanh(\kappa h)\right]\left[1+\frac{N_s g\kappa}{\omega^2} tanh(\kappa z_L)\right] \tag{3.5}$$

It is instructive to note that under specific conditions of $z_L = 0$, Eq. (3.5) yields the dispersion relationship for the one-layer fluid:

$$\omega^2 = N_s g\kappa_0 tanh(\kappa_0 h) \tag{3.6}$$

where κ_0 denotes the wave number for the one-layer fluid.

The nonlinear equation Eq. (3.5) can be solved numerically. During the root-finding procedure, two real roots for κ exist for a given angular frequency ω, among them one root corresponds to the surface-wave mode $\kappa \cong \kappa_0$, and the other one corresponds to the internal-wave mode $\kappa \gg \kappa_0$ (Ting, 1992). For the surface wave mode considered in this study, the former root is of our interest (Sassa *et al.*, 2001).

The amplitude of oscillatory pore pressure $u_e^{(1)}$ at a generic point in the liquefied soil is related to the amplitude of fluid pressure oscillation at the water-soil interface, u_0 by

$$u_e^{(1)} = \frac{\rho_2 \omega^2 [cosh(\kappa z) - sinh(\kappa z) tanh(\kappa z_L)]}{\rho_2 \omega^2 + (\rho_2 - \rho_1) N_s g \kappa tanh(\kappa z_L)} u_0 \qquad \text{for} \quad z_L \le z \le 0 \qquad (3.7)$$

When z is approaching zero, Eq. (3.7) indicates $u_e^{(1)} > u_0$. This discrepancy stems from the discontinuity of density in two layers. However, the continuity of pressure is satisfied at the interface $z = 0$.

Substituting z by z_L in Eq. (3.7) leads to the amplitude of fluid pressure fluctuation, u_L, as

$$u_L = \frac{\rho_2 \omega^2}{\rho_2 \omega^2 cosh(\kappa z_L) + (\rho_2 - \rho_1) N_s g \kappa sinh(\kappa z_L)} u_0 \qquad (3.8)$$

And the amplitude of the vertical displacement of the surface of a liquefied soil, a_1, is expressed as follows:

$$a_1 = \frac{\kappa tanh(\kappa z_L)}{\rho_2 \omega^2 + (\rho_2 - \rho_1) N_s g \kappa tanh(\kappa z_L)} u_0 \qquad (3.9)$$

The wave number κ involved in Eqs. (3.7)–(3.9) is determined by the dispersion relationship for the two-layer fluid as defined by Eq. (3.5).

3.2.2 **Formulation for the lower sub-system**

Suppose the liquefaction front is located at $= z_L$, the sub-liquefied soil is below z_L, as shown in Fig. 3.3. After the approach adopted by Sassa *et al.* (2001), the wave-induced

stress changes in the sub-liquefied soil layer are described herein based on the poroelastic solutions for infinite seabed (Madsen, 1978; Yamamoto et al., 1978).

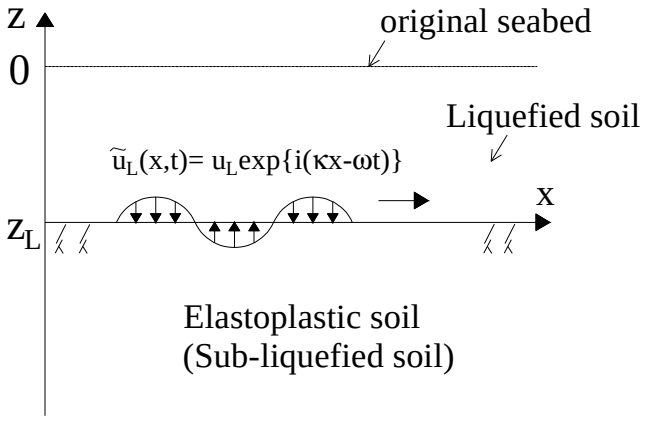

Fig. 3.3 Problem definition for the lower sub-system

For clarity, the related formulas for the general liquefaction front location and the particular location $z_L = 0$ are presented here. When $z_L = 0$, the fluid pressure $\tilde{u}_L(x,t) = \tilde{u}_0(x,t)$ on $z_L = 0$. The corresponding amplitudes of the oscillatory pore pressure $u_e^{(1)}$ and the maximum cyclic shear stress τ at depth z are expressed by (for details of the derivation, refer to Appendix C of this thesis)

$$u_e^{(1)} = u_0 exp(\kappa_0 z) \qquad \text{for} \quad z \le 0 \tag{3.10}$$

$$\tau = -\kappa_0 u_0 z exp(\kappa_0 z) \qquad \text{for} \quad z \le 0 \tag{3.11}$$

Thus, the cyclic stress ratio τ/σ'_{v0} may be expressed as

$$\frac{\tau}{\sigma'_{v0}} = \frac{\kappa_0 u_0}{\gamma'} exp(\kappa_0 z) \tag{3.12}$$

Following Eq. (3.12), we have

$$\left(\frac{\tau}{\sigma'_{v0}}\right)_{z=0} = \frac{\kappa_0 u_0}{\gamma'} \tag{3.13}$$

When the liquefaction front arrives at $z = z_L$, the wave pressure fluctuation that acts on the fluid-soil interface, $\tilde{u}_L$ and shear stress, τ can be obtained by transforming Eq. (3.10) and Eq. (3.11) into

$$u_e^{(1)} = u_L exp[\kappa(z - z_L)] \quad \text{for} \quad z \le z_L \tag{3.14}$$

$$\tau = -\kappa u_L \cdot (z - z_L) exp[\kappa(z - z_L)] \quad \text{for} \quad z \le z_L \tag{3.15}$$

In the above equations, wave number κ is determined by Eq. (3.5) and u_L is defined by Eq. (3.8). The vertical effective stress,σ'_v, on a soil horizon z (where $z \le z_L$) may be expressed as

$$\sigma'_v = -\gamma' \cdot (z - z_L) \tag{3.16}$$

from Eq. (3.14) – Eq. (3.16), the shear stress and the cyclic stress ratio within sub-liquefied seabed are given by

$$u_e^{(1)} = u_0 \exp(\kappa z) F \tag{3.17}$$

$$\chi \equiv \frac{\tau}{\sigma'_v} = \frac{\kappa u_0}{\gamma'} \exp(\kappa z) F \tag{3.18}$$

where function F is defined by

$$F = \frac{\rho_2 \omega^2}{\exp(\kappa z_L)[\rho_2 \omega^2 \cosh(\kappa z_L) + (\rho_2 - \rho_1) N g \kappa \sinh(\kappa z_L)]} \tag{3.19}$$

Particularly when $z_L = 0$, $F = 1$, $\kappa = \kappa_0$ and $\sigma'_v = \sigma'_{v0} = -\gamma' z$. At the elevation of the soil surface ($z = 0$), the cyclic stress ratio χ defined by Eq. (3.18) reduces to χ_0 defined by $\kappa_0 u_0/\gamma'$.

Under the action of cyclic wave loading, soil volume decreases due to the plasticity. Sassa and Sekiguchi (1999) developed the storage equation for the poro-elasto-plastic seabed with contractancy (Derivation procedure and related assumption refer to Appendix B). The distinct character is the specification of development of the plastic volumetric strain, υ^p which is employed to relate the contractive nature of seabed in response to the cyclic wave loading.

The storage equation is written as (Sassa *et al.*, 2001)

$$\frac{\partial u_e^{(2)}}{\partial \xi} = \Phi \frac{\partial^2 u_e^{(2)}}{\partial (\kappa_0 z)^2} + M \frac{\partial \upsilon^p}{\partial \xi} \qquad \text{for} \qquad -D \le z \le z_L \qquad (3.20)$$

where the loading cycle, $\xi = \omega t/2\pi$; M is the constrained modulus of the soil skeleton, which was assumed by Sassa *et al.* (2001) to increase linearly with the increasing effective confining pressure as follows:

$$M = -\frac{\gamma'(z - z_L)}{\gamma' D} M_D = -\frac{z - z_L}{D} M_D \qquad \text{for} \qquad -D \le z \le z_L \qquad (3.21)$$

where M_D is a reference value of M at the bottom $z = -D$ when $z_L = 0$.

The partial drainage factor defined, Φ in Eq. (3.20) is

$$\Phi = 2\pi \frac{kM}{\gamma_f \omega} \kappa_0^2 \qquad (3.22)$$

in which k is the Darcy coefficient of permeability and γ_f is the unit weight of the pore fluid.

The term $\partial \upsilon^{\mathrm{p}} / \partial \xi$ reflects soil cyclic plasticity of the seabed. For a simple case with constant cyclic stress ratio in a cohensionless soil subjected to drained cyclic shearing, Sassa *et al.* (2001) assumed the development of the plastic volumetric strain υ^p with the loading cycle ξ as:

$$\upsilon^{\mathrm{p}}(\xi, \chi) = [1 - \exp(-\beta\xi)]\upsilon_{\infty}^{\mathrm{p}}(\chi) \tag{3.23}$$

$$\upsilon_{\infty}^{\mathrm{p}}(\chi) = \mathrm{R} \cdot [\exp(\alpha\chi) - 1] \tag{3.24}$$

where β, R and α are material parameters and υ_{∞}^{p} denotes the amount of plastic volumetric strain as ξ approaching infinity. Hence, the rate of plastic volumetric change, $\partial \upsilon^p / \partial \xi$ can be expressed as

$$\frac{\mathrm{d}\upsilon^{\mathrm{p}}}{\mathrm{d}\xi} = \beta \exp(-\beta\xi)\upsilon_{\infty}^{\mathrm{p}}(\chi) \tag{3.25}$$

In view of the form of $\partial \upsilon^p / \partial \xi$, Sassa *et al.* (2001) made an assumption of the its expression corresponding to the cases with continuously increasing stress rate, χ as

$$\frac{\mathrm{d}\upsilon^{\mathrm{p}}}{\mathrm{d}\xi} = \beta\left[\upsilon_{\infty}^{\mathrm{p}}(\chi) - \upsilon^{\mathrm{p}}\right] \tag{3.26}$$

which can be solved numerically.

To achieve the solution of built-up pore pressure, a set of appropriate boundary conditions are need. According to the liquefaction criteria, the boundary condition on $z = z_L$ requires that

$$u_e^{(2)} = -\gamma' z_L \qquad \text{for} \qquad z = z_L \leq 0 \tag{3.27}$$

On the rigid impermeable base $z = -D$, no fluid flow is allowed to take place, which means

$$\frac{\partial u_e^{(2)}}{\partial z} = 0 \qquad \text{on} \qquad z = -D \tag{3.28}$$

The storage equation employed here was extended by Miyamoto *et al.* (2004) to non-homogenous porous media with respect to varying permeability. Liu *et al.* (2009) also utilized it but stated that the model did not account fully for the behaviour of the soil e.g. plasticity in general and the plastic behaviour of the soil is limited to volumetric compression.

3.3 Numerical scheme and procedure

Finite-difference scheme can be used to solve the governing equation of Eq. (3.20). Since the liquefaction front is continually moving downward (the solidification process is not included here), the computation domain is becomes thinner with liquefaction keeps continuing. In practice, a constant element thickness, Δz can be assumed considering the computation accuracy level. Then the sub-liquefied seabed is spatially discretized into n elements (n varies with liquefaction front advances and $n \cdot \Delta z = -D - z_L$). As shown in Fig. 3.4, the vertical coordinate z_i of nodal line i is described as $z_i = z_L + (i-1)\Delta z$, for $i = 1, n+1$. The nodal line $z = z_1$ corresponds to the location of the liquefaction front $z = z_L$, while the nodal line $z = z_{n+1}$ represents the bottom of the soil layer, $z = -D$.

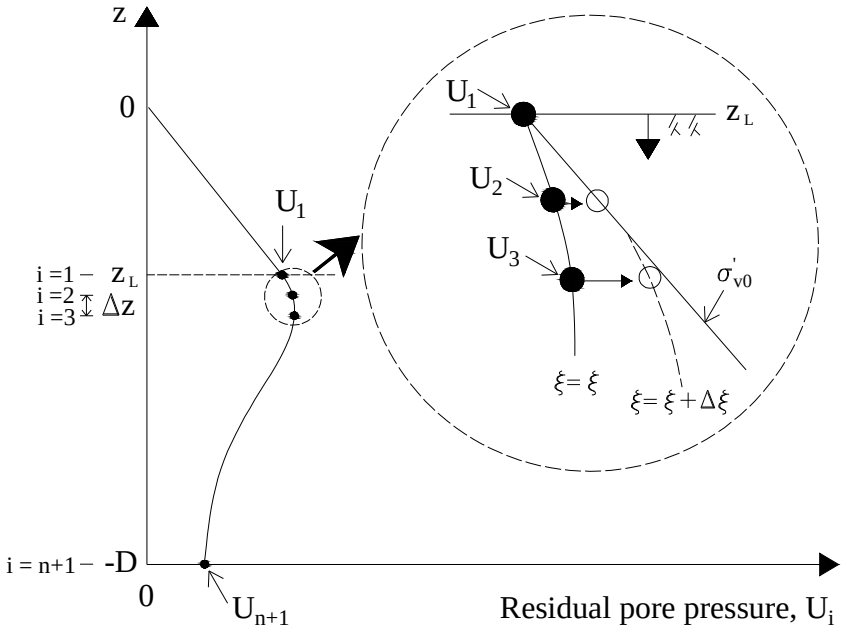

Fig. 3.4 Sketch showing the identification of the liquefaction front

There are totally $n+1$ primary unknowns U_i (here, U_i is used to denote $u_e^{(2)}$ for simplicity in expression) for $i = 1, n+1$. Let Z denotes $\kappa_0 z$ and $\Delta\xi$ denote the increment of wave loading cycles, Eq. (3.20) may be expressed in matrix form as

$$\begin{bmatrix} 1 & 0 & \cdots & \cdots & \cdots & \cdots & 0 \\ A & B & A & 0 & \cdots & \cdots & \vdots \\ 0 & A & B & A & 0 & \cdots & \vdots \\ \vdots & \ddots & \ddots & \ddots & \ddots & & \vdots \\ \vdots & & \ddots & \ddots & \ddots & \ddots & \vdots \\ \vdots & & & 0 & A & B & A \\ 0 & & & & 0 & A & B^* \end{bmatrix} \begin{Bmatrix} U_1 \\ U_2 \\ U_3 \\ \vdots \\ \vdots \\ U_n \\ U_{n+1} \end{Bmatrix}_{\xi+\Delta\xi} = \begin{Bmatrix} -\gamma' z_L \\ U_2 \\ U_3 \\ \vdots \\ \vdots \\ U_n \\ U_{n+1} \end{Bmatrix}_{\xi} + \begin{Bmatrix} 0 \\ Mq \\ Mq \\ \vdots \\ \vdots \\ \vdots \\ Mq \end{Bmatrix}_{\xi} \cdot \Delta\xi \qquad (3.29)$$

where

$$A = -\phi \frac{\Delta\xi}{(\Delta Z)^2} \tag{3.30}$$

$$B = 1 + 2\phi \frac{\Delta\xi}{(\Delta Z)^2} \tag{3.31}$$

$$B^* = 1 + \phi \frac{\Delta\xi}{(\Delta Z)^2} \tag{3.32}$$

$$q = \frac{\partial v^p}{\partial \xi}\Big|_{\xi} \tag{3.33}$$

The first and bottom row of Eq. (3.29) are designed to represent the boundary condition at $z = z_L$ as defined by Eq. (3.27) and the undrained boundary condition as defined by Eq. (3.28). The remaining $n - 1$ rows arise from the partial differential Eq. (3.20). The simultaneous linear Eq. (3.29) can be solved using the method of Gaussian elimination (Sassa *et al.*, 2001).

Solution procedure of the entire system

Once the location of liquefaction front is known (namely the computation domains are determined), the entire system can be solved sequentially as shown in Fig. 3.5. At the very beginning, $z_L = 0, a_0 = 0, U_i = 0$ and the initial values for wave number $\kappa = \kappa_0$.

Otherwise, they are determined or updated from the preceding solution. Next, the source term $M \cdot q\Delta\xi$ in Eq. (3.29) under a given wave loading is obtained. Following it, we can get the residual pore pressures $U_i (i = 1, n + 1)$ through solving Eq. (3.29) by Gaussian elimination method. Based on the liquefaction criteria, the liquefaction front location is

updated. Repeats the procedure until the targeted number of wave loading cycles, ξ_{max}, is reached.

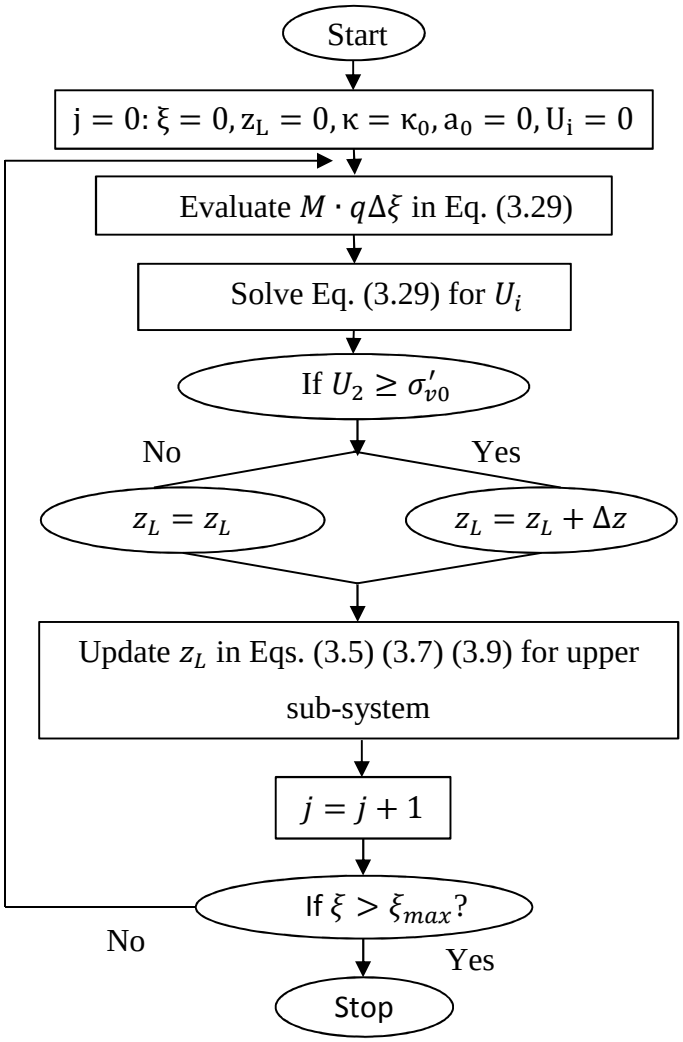

Fig. 3.5 Flowchart for the solution procedure of entire system

At each time step, the solution of the entire system can predict the following quantities: the residual and oscillatory pore pressure components in both the liquefied soil and the underlying sub-liquefied soil, the vertical displacements of the fluid-soil interface (also termed as internal or interface wave motion), the time-varying wave number, κ, and the liquefaction front.

3.4 Model verification

Based on the formulations described in the preceding sections a numerical code is developed using FORTRAN90 language. To validate the code, the case of the Keisa No. 7 sand from the original paper is considered for comparisons with both the centrifuge wave tank tests and simulation results. The wave conditions and the soil parameters used are listed in Table 3.1.

Table 3.1 Wave conditions and soil parameters

Wave conditions	
Wave loading cycles, ξ_{max}	100
Wave frequency, $f(\omega/2\pi)$: Hz	11
Centrifugal acceleration, N_s	30
Fluid depth, h: m	0.09
Initial wave number, $\kappa_0: m^{-1}$	12.2
Wave pressure, $u_0: kPa$	5.0
Soil bed conditions	
Soil depth, $D: m$	0.1
Density of fluid, $\rho_1: kg/m^3$	980
Density of liquefied soil, $\rho_2: kg/m^3$	1840

Constitutive parameters	
R	4.6×10^{-5}
α	55
β	0.1
$M_D: kPa$	5000

Comparisons were also performed in terms the location of the liquefaction front z_L, and three other variables: the wave number κ, vertical movement of seabed surface, a_0 and the excesses pore pressure. The numerical results of the present numerical model are identical to that of Sassa *et al*. (2001), as shown in Fig. 3.6, Fig. 3.7, and Fig. 3.8.

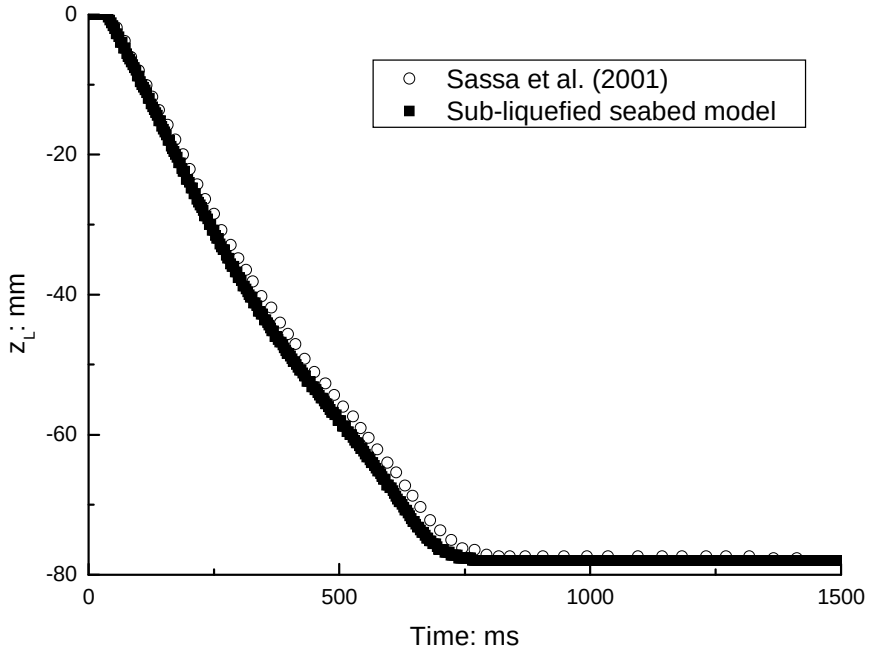

Fig. 3.6 Variation of the location of the liquefaction front

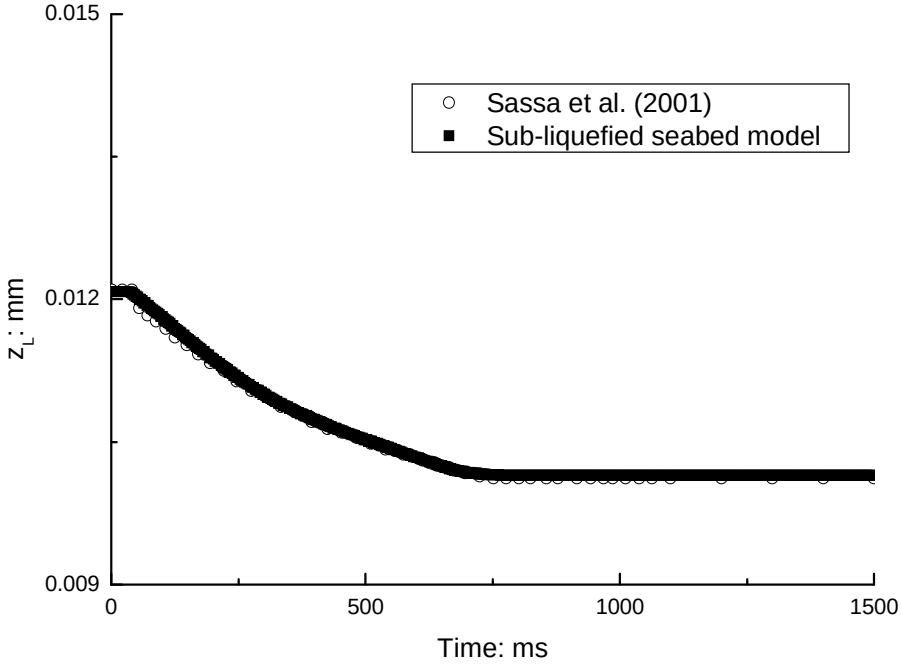

Fig. 3.7 Predicted wave number

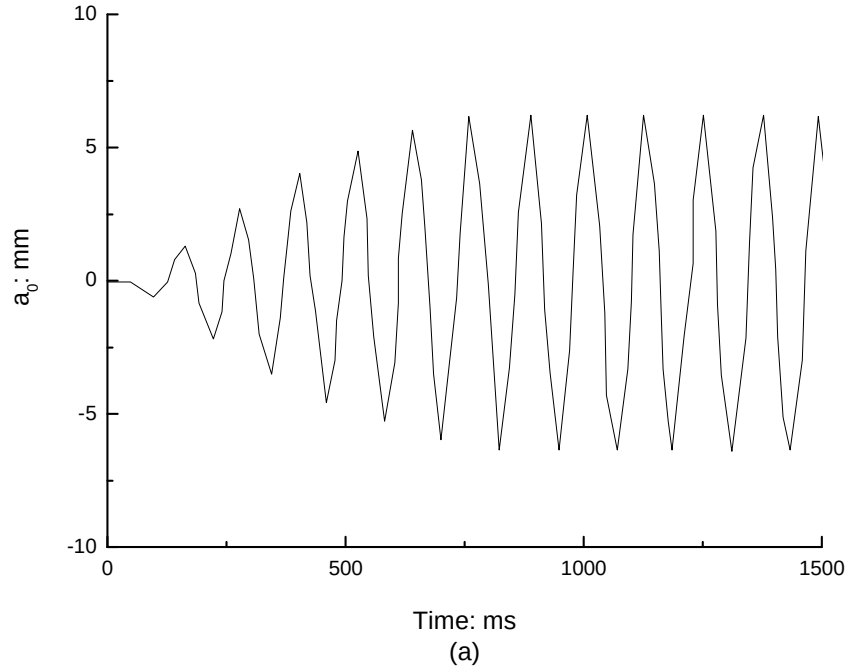

(a)

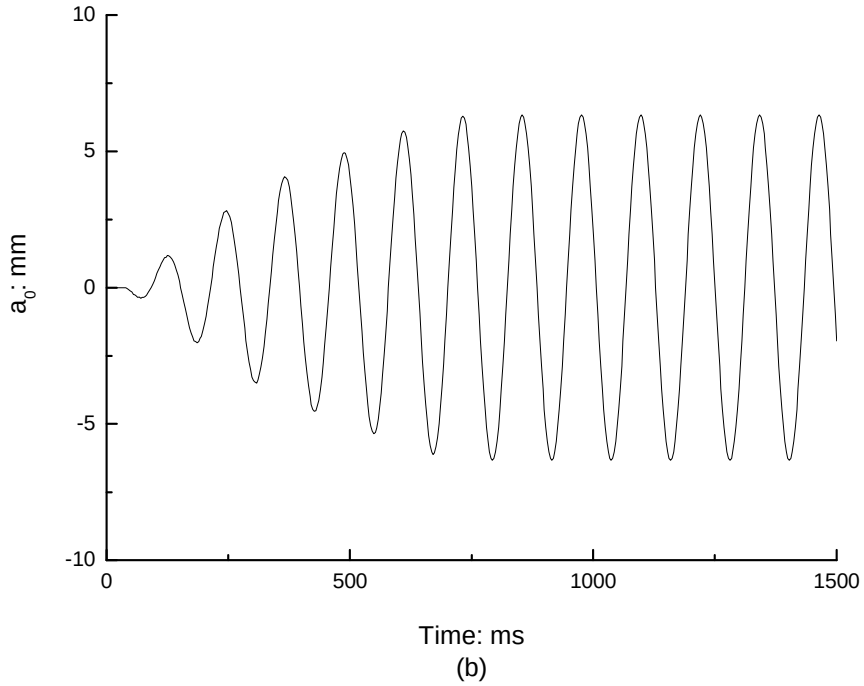

Fig. 3.8 Predicted vertical movement of the soil surface: (a) is the result of Sassa 2001; (b) is the reproduced result

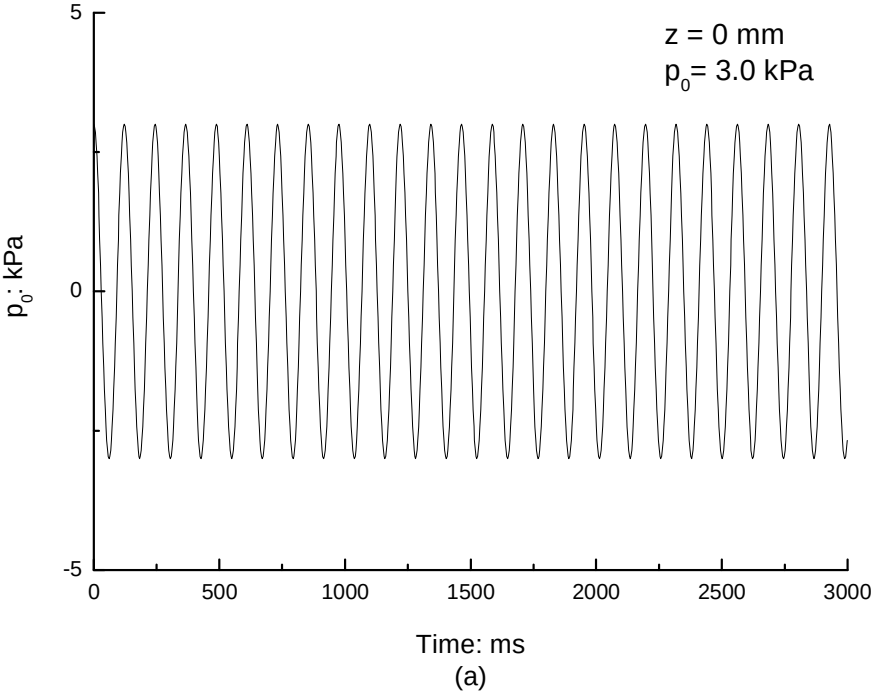

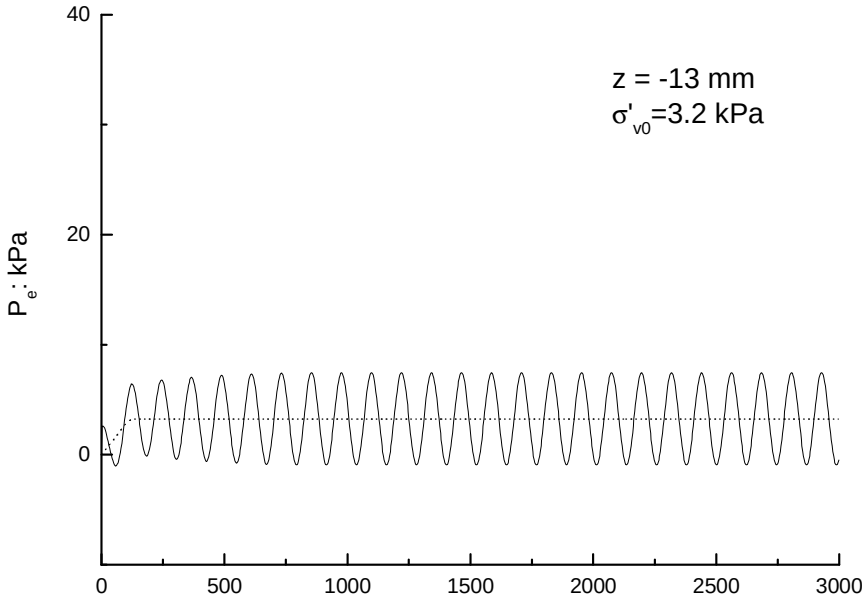
40
20
0
P_e: kPa
z = -13 mm
σ'_{v0}=3.2 kPa
0
500
1000
1500
2000
2500
3000
Time: ms

(b)

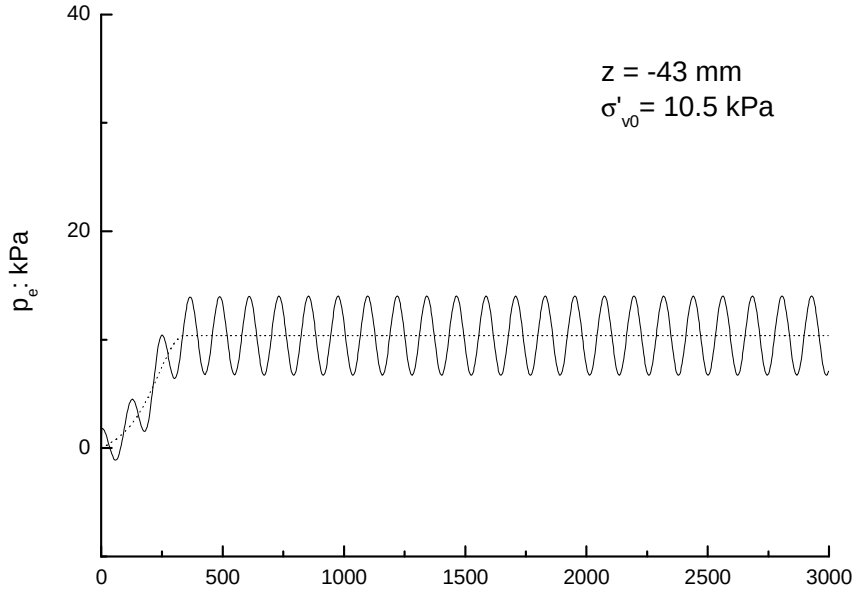
40
20
0
p_e: kPa
z = -43 mm
σ'_{v0}= 10.5 kPa
0
500
1000
1500
2000
2500
3000
Time: ms

(c)

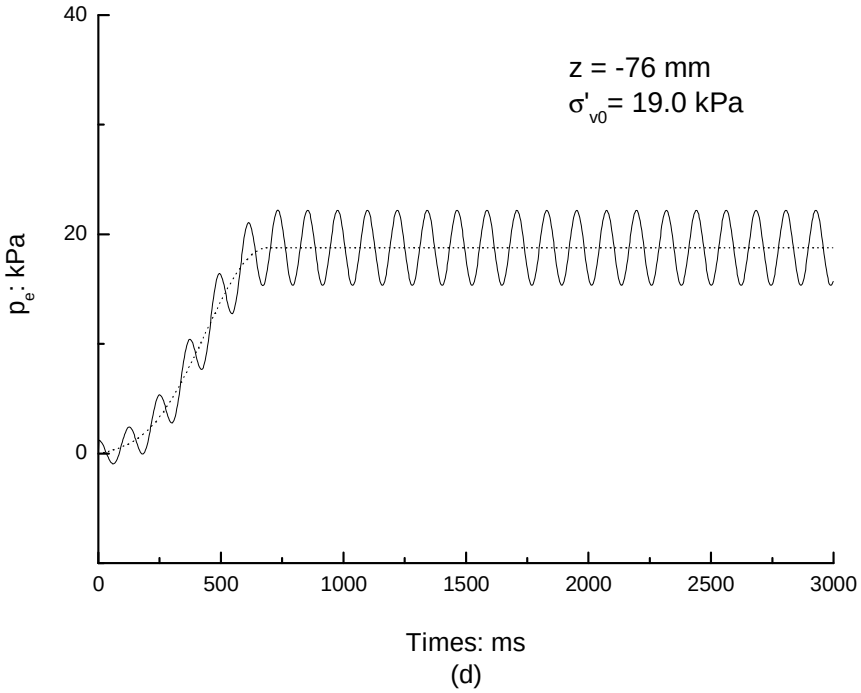

Fig. 3.9 Time history of excess pore pressure: solid line is total amount and dotted line is the residual component. (a) is the wave pressure acting on the soil surface and (b), (c) and (d) are excess pore pressures

For the sake of the comparison between the present simulation results with centrifuge test, the corresponding measured results are shown from Fig. 3.10-Fig. 3.11.

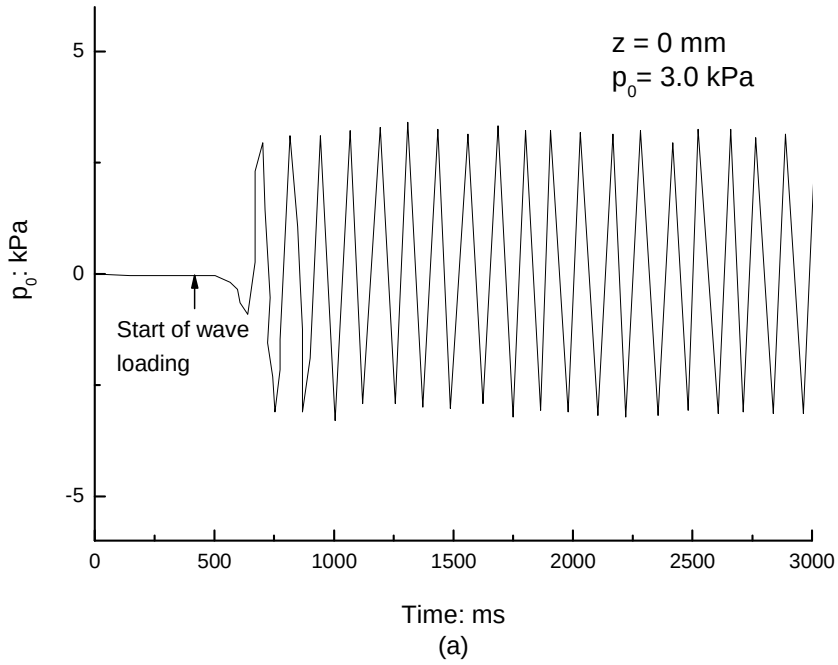

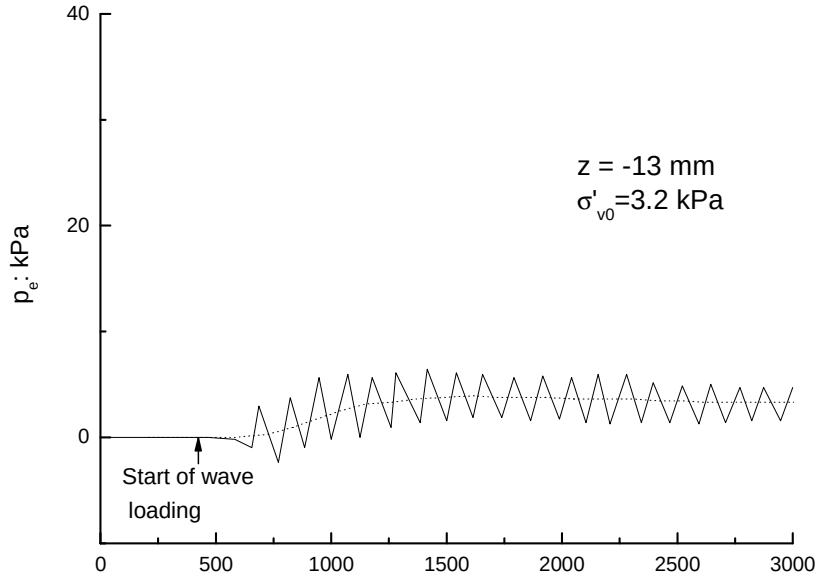
40
20
0
p_e: kPa
z = -13 mm
σ'_{v0}=3.2 kPa
Start of wave
loading
0
500
1000
1500
2000
2500
3000
Time: ms

(b)

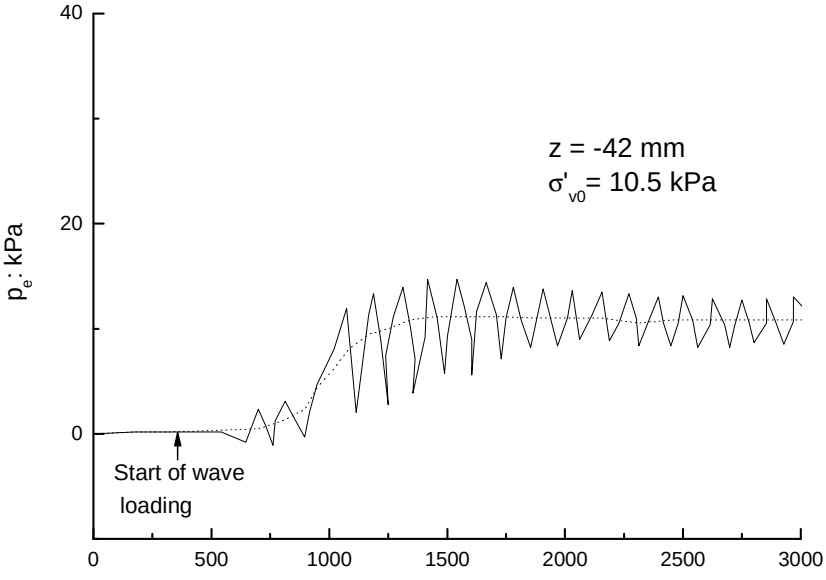
40
20
0
p_e: kPa
z = -42 mm
σ'_{v0}= 10.5 kPa
Start of wave
loading
0
500
1000
1500
2000
2500
3000
Time: ms

(c)

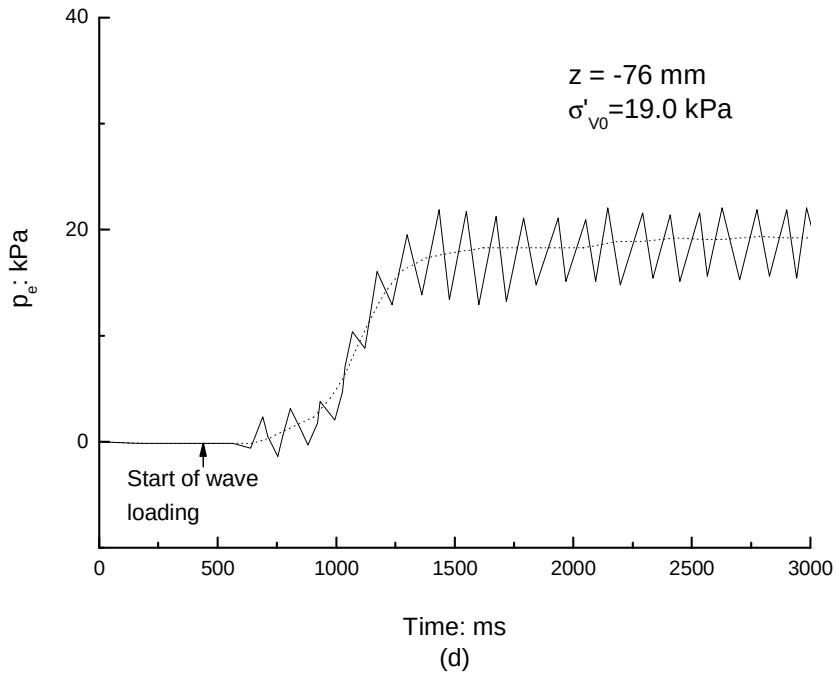

Fig. 3.10 Time history of measured excess pore pressure: solid line is total amount and dotted line is the residual component. Time histories of (a) wave pressure acting on the soil surface and (b), (c) and (d) excess pore pressure

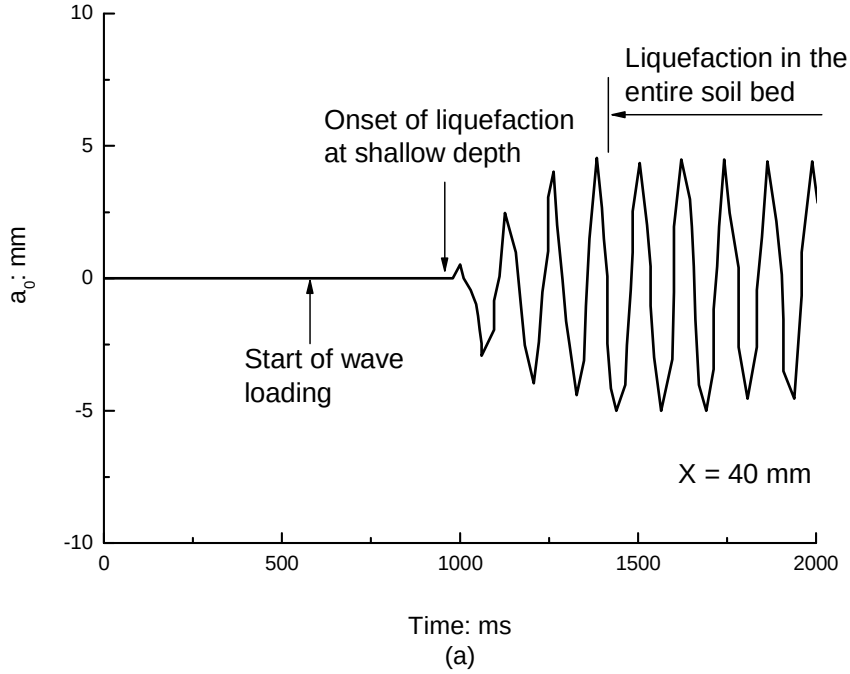

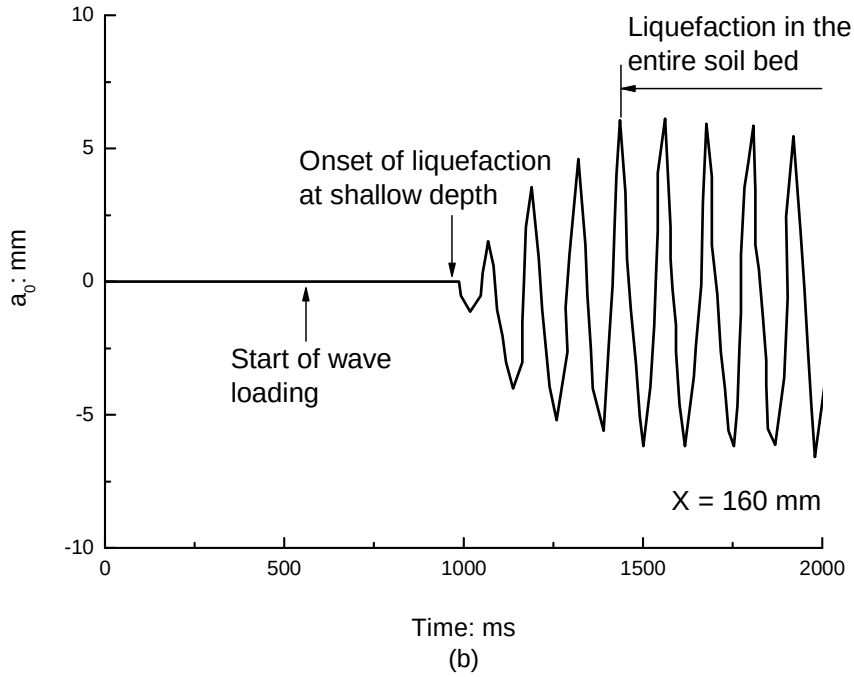

Fig. 3.11 Measured time histories of vertical movement of soil surface in wave test HC at different locations: (a) X=40mm; (b) X=160mm

3.5 Summary

Following the approach proposed by Sassa *et al*. (2001), a progressive liquefaction model was constructed. By comparisons with both centrifuge wave tank tests and simulation results in Sassa *et al*. (2001), the accuracy and robustness of the model are verified. In the next chapter, this model will be employed to investigate the seabed liquefaction under random linear progressive waves using the ensemble modelling method.

Chapter 4 Ensemble Modelling for the assessment of random wave-induced liquefaction risks

4.1 General

In realistic environment, random waves instead of a regular water surface elevation introduce the relevant change on the wave dynamic pressure acting at the seabed, which further induce the variation of pore water pressure and effective stresses inside the marine sediments (Walter, 1968). In this chapter, we consider a series of random waves propagating over a porous seafloor with an infinite thickness ($D \to \infty$) above a rigid impermeable bottom, as shown in Fig. 4.1.

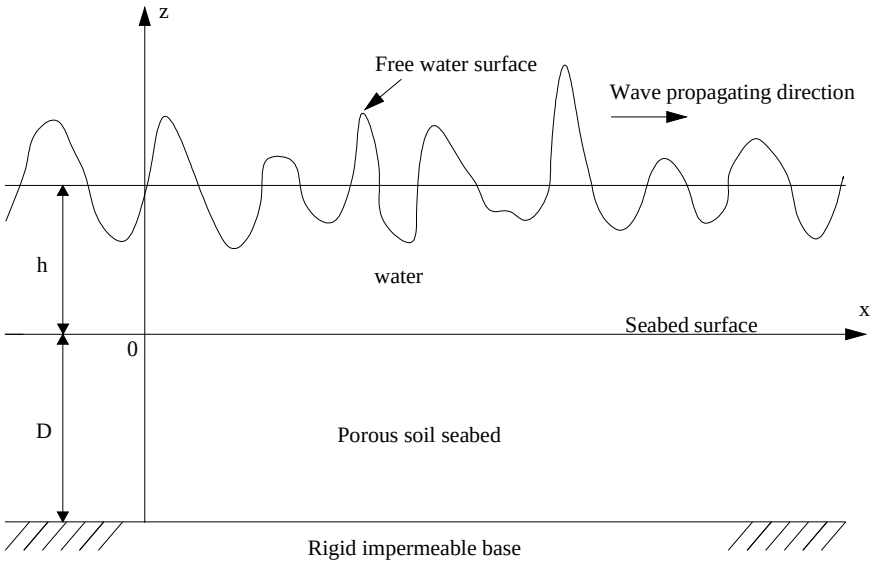

Fig. 4.1 Definition sketch of random wave propagation over a porous seabed

4.2 Wave sampling techniques

To simplify the analysis and recognise that liquefaction usually takes place over a short time scale characterised by a single storm the simulation is limited to large

narrow-band waves. Based on the linear wave theory the wave height was theoretically found to obey the Rayleigh distribution with the probability density function given as follows (Longuet-Higgins, 1952; Tayfun, 1981):

$$P(H) = \frac{2H}{H_{rms}^2} exp\left[-\left(\frac{H}{H_{rms}}\right)^2\right] \tag{4.1}$$

According to the linear wave theory the mean wave height H_z can be related to the wave pressure at the top of the sand bed surface, u_0, as

$$\mathrm{H_z} = \frac{2u_0}{\rho_1 \mathrm{g}} \cosh(\kappa \mathrm{h}) \tag{4.2}$$

And the root mean squared wave height H_{rms} can be approximated as $1.13\, H_z$. Assume X_r is uniformly distributed on (0, 1), then the random wave height, H which satisfies Rayleigh distribution as shown in Eq. (4.3) can be expressed as

$$\mathrm{H} = \mathrm{H_{rms}}\sqrt{-\ln(1 - X_r)} \tag{4.3}$$

For $u_0 = 3\ kPa$ as used in the tests of Sassa *et al.* (2001), the root mean square wave height $H_{rms} = 0.030\ m$. Random variable, X_r is provided by a normal distribution variable generator. And hence, the wave heights H were generated by repeat random sampling from Eq. (4.1) with excluding of $H > 0.1L$ (in which cases, linear wave theory are not valid). As shown in Fig. 4.2, the distribution of the numerically generated wave heights based on Eq. (4.1) compare well with the theoretical distribution calculated from Eq. (4.1) using $H_{rms} = 0.030\ m$.

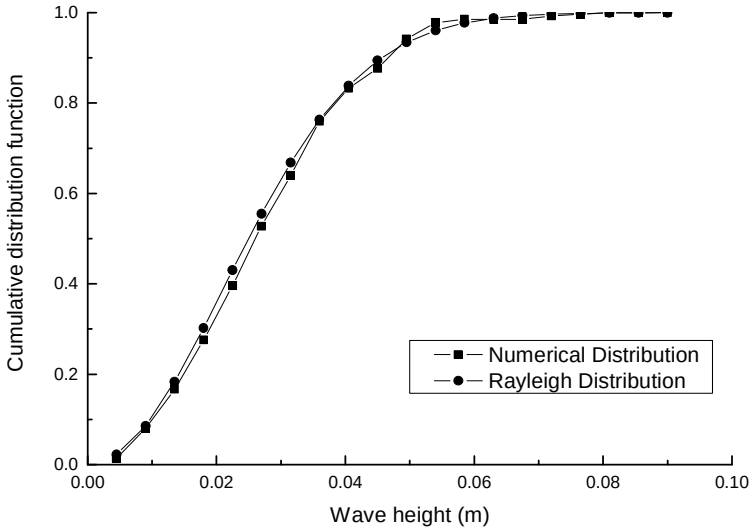

Fig. 4.2 Cumulative distribution function of wave height

4.3 Ensemble modelling results

4.3.1 Regular wave time series

The present work is limited to assessing the randomness of wave parameters only (wave heights) all soil material and other parameters in the model are treated as deterministic constants which are as listed in Table 3.1. Considering that the liquefaction depth is likely to be deeper in ensemble modelling, the depth of soil layer used is increased to 320mm instead of the 80mm used in chapter 3 to reduce the constraint of the soil layer thickness on liquefaction front. Using the same linear variation as assumed in Sassa *et al.* (2001), the value for M_D at the bottom of the soil layer then becomes 50,000 which give a corresponding value 5,000 at a depth of 80 mm in the soil layer.

Instead of using a representative wave height such as the root mean square wave height (H_{rms}) to determine a single liquefaction depth in a random wave field, an ensemble approach calculates the liquefaction depths due to all possible wave heights

described by the Rayleigh distribution and then determines a representative liquefaction depth. This was achieved by performing multiple model runs using regular waves with wave height randomly generated wave height from Rayleigh distribution. Each run ends when the liquefaction front reaches an equilibrium value or the bottom of the seabed. In total 275 runs were performed and the histogram of the maximum liquefaction depth is shown in Fig. 4.3.

As it is expected for a large number of small wave height (> 120) no liquefaction is predicted. For the rest of the wave height the predicted liquefaction depth ranges from 0 to 0.32 m with the depth at the peak of the distribution being about 0.128 m. The mean and root mean square liquefaction depths determined from the histogram are 0.066 and 0.10 m, respectively, compared to the liquefaction depth calculated using a single representative wave height $\mathrm{H_{rms}} = 0.03$ m which is 0.085 m. In detail, the mean (z_L^m) and root mean square (z_L^{rms}) liquefaction depths are calculated as

$$z_L^m = \frac{1}{N_r}\sum_{i=1}^{N_r} z_L \tag{4.4}$$

$$z_L^{rms} = \sqrt{\frac{1}{N_r}\sum_{i=1}^{N_r} z_L^2} \tag{4.5}$$

where N_r is the size of random sample.The histogram for the time to reach the maximum liquefaction depth is shown in Fig. 4.4. The largest value corresponds at the far right corresponds to the end of the run time when no liquefaction was predicted and is not physically relevant. The predicted time ranges from around 0.6 to 3.6 s with a value at the distribution peak being 2.1 s.

The mean and root mean square time to the maximum liquefaction depth determined from the histogram excluding no liquefaction runs are 1.88 and 1.98 s which are, as expected, smaller but comparable to the corresponding value calculated using a single representative wave height H_{rms} which 2.24 s.

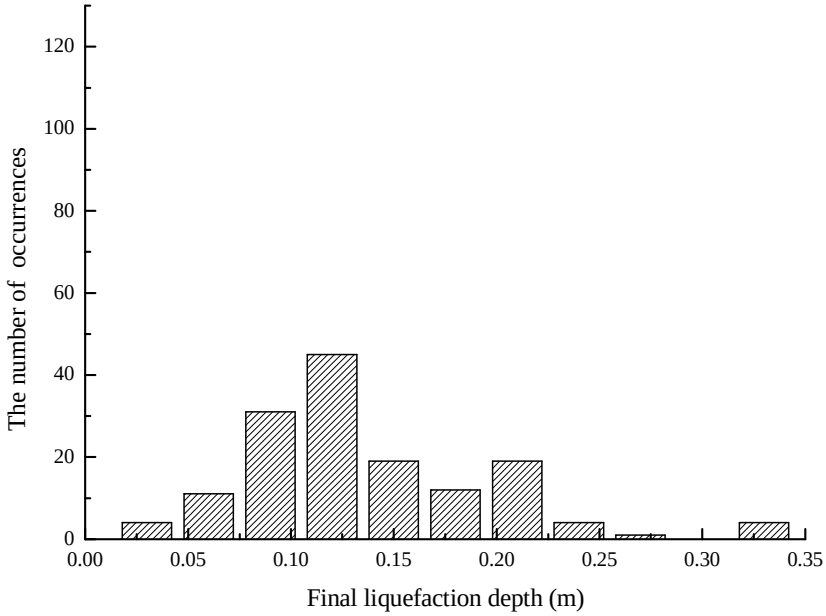

Fig. 4.3 Histogram of the maximum liquefaction depth

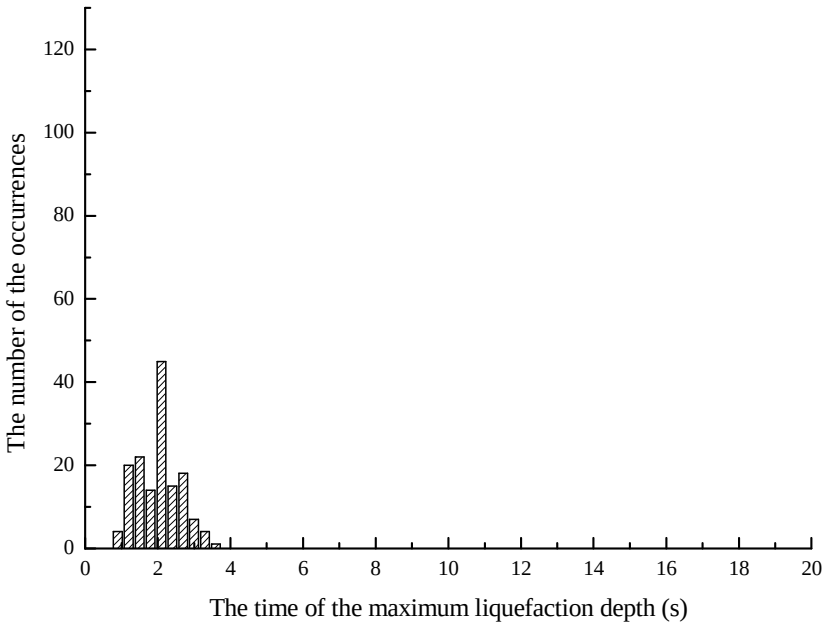

Fig. 4.4 Histogram of liquefaction time

4.3.2 **Random wave time series**

As a real random wave time series consists of individual waves of different heights and frequencies, a more realistic ensemble modelling approach is to perform multiple runs using a randomly varying wave height time series instead of a constant wave height as in the previous runs. The random wave series is generated by assuming that each sampled wave height from the Rayleigh distribution lasts one period and then it is followed by another randomly sampled wave height for another period and so on. Therefore, each random wave series is a succession of sinusoid waves with randomly generated wave height and the total elapsed time is $4000T$. Admittedly, the liquefaction model by Sassa *et al.* (2001) contain the stress terms that are strictly applicable only to linear harmonic waves. The model is nevertheless used here as a first approximation in order to determine the transient liquefaction under a random wave train consisted of a series of individual waves of varying wave height and a constant wave period.

Fig. 4.5 shows the histogram of the liquefaction depth calculated using 100 random wave series together with the results. It can be seen that the random wave-induced liquefaction is much deeper than that corresponding to the equivalent regular wave case. The former value ranges from 0.100 to 0.320 m being 0.200 m at the peak of the distribution, while the latter is around 0.085 m. The reason for the deeper liquefaction in random waves is that the liquefaction depth is mainly affected by the portion of large waves in the random wave series as the values corresponding to $H_{1/3}$ and $H_{1/10}$ are 0.150 and 0.231 m, respectively.

Due to the presence of large number of small waves in the time series the time to the maximum liquefaction is expected to be longer for random waves, which is confirmed by the calculations as shown in Fig. 4.6. The shortest time is approaching that for the

regular wave, which is about 4 s; and the longest liquefaction time can reach as long as 24.4 s, which is nearly 6 times of that for regular wave.

The likely reason for the longer liquefaction time is that individual waves in the wave series whose heights are less than a critical value tend not to contribute to the propagation of liquefaction front. The maximum liquefaction depth is closely associated with the timing of the largest waves in the wave time series.

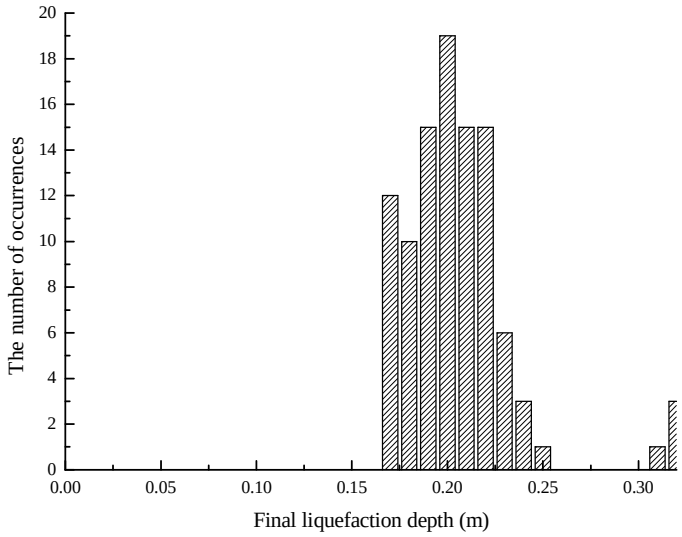

Fig. 4.5 Histogram of the maximum liquefaction depth

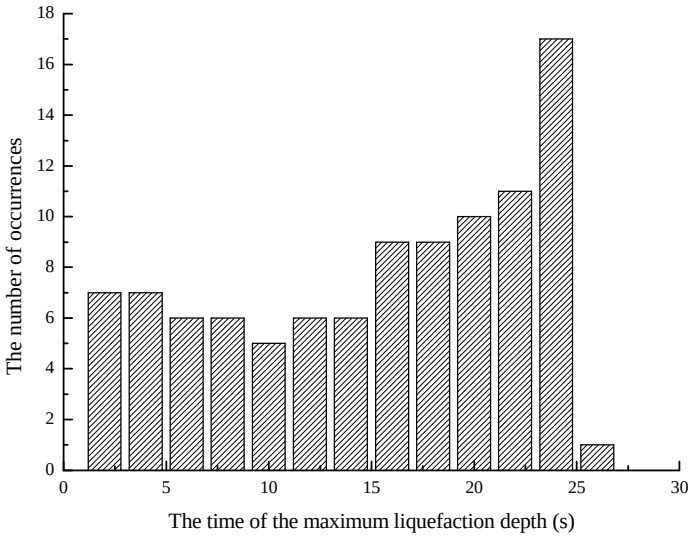

Fig. 4.6 Histogram of liquefaction time

4.3.3 **Wave height and sequencing effects on liquefaction**

As mentioned in the previous section, the wave series is a succession of sinusoid waves with varying wave height generated according to Rayleigh distribution. Thus, there is a maximum value of the wave heights for each wave series. To further understand the liquefaction depth distribution the maximum wave height in each wave time series is plotted against the corresponding final liquefaction depth in Fig. 4.7. Strong linear correlation exists between the two except four data points when the predicted liquefaction depths are the greatest presumably caused by the existence of disproportional number of large waves in these time series. On balance it is reasonable to include that the extent of liquefaction is controlled by the size and number of largest wave heights in the wave time series.

In order to investigate whether the order of appearance of waves of different height in a random wave series will affect the liquefaction time, the relationship between the

time when the liquefaction depth reaches the maximum and the time when the maximum wave height occurs is shown in Fig. 4.8.

Despite some scatter a discernible linear correlation between the two times can be identified, which implies that the time for the maximum liquefaction depth to be reached is strongly associated with the time of occurrence of the maximum wave height except perhaps when the maximum wave height in the sample is very small. The overall relationship seems to indicate that the timing of largest waves in the wave time series controls the time for the maximum liquefaction depth to be reached, at least for large liquefaction depth.

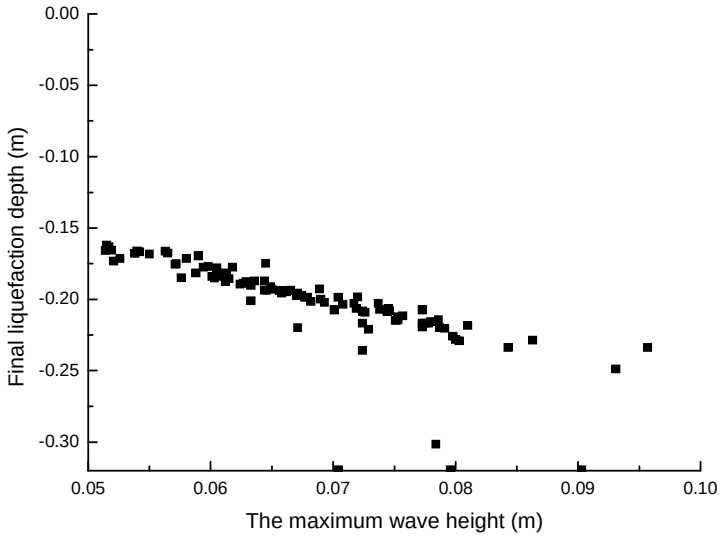

Fig. 4.7 Relationship between the maximum wave height and final liquefaction depth

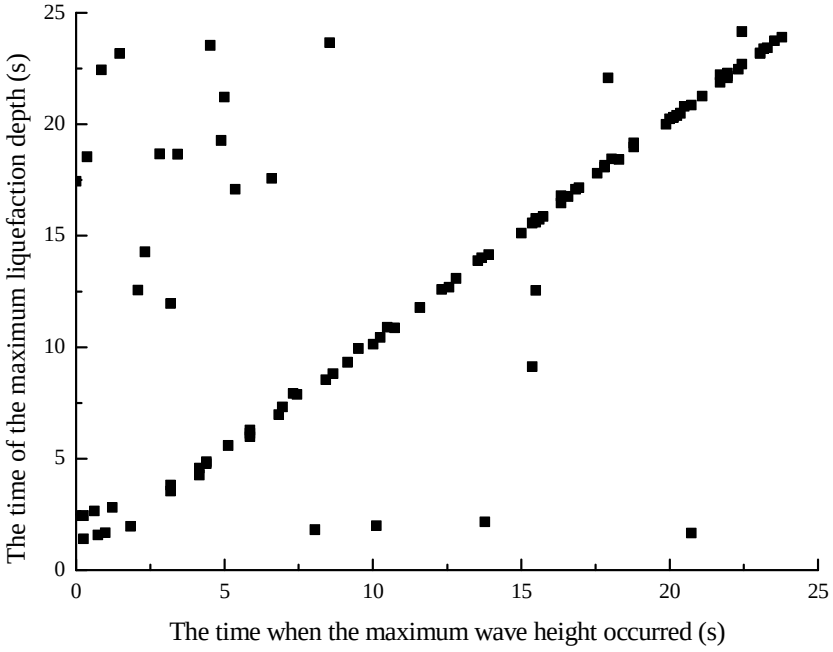

Fig. 4.8 Relationship between the time to the maximum liquefaction and the time of maximum wave height occurrence

4.4 Discussion

4.4.1 **Temporal scale of liquefaction**

According to the experimental studies of Sumer *et al.* (2006) liquefaction is considered as part of a sequence of sediment behaviour from the build-up of pore pressure, to the resulting liquefaction, to the densification of the sediment bed. Under irregular waves, the liquefaction front in a homogenous bed cannot propagate downward indefinitely and has to stop at a certain depth where shear deformations are large enough to cause liquefaction. The compaction begins from the bottom of the liquefied zone with the compaction front moving upwards until it reaches the surface of the sediment. Similar cycle of sediment behaviour was also observed previously by

Miyamoto *et al.* (2004) in a series of experiments conducted in a wave tank mounted in a centrifuge.

Soil densification under regular waves is usually considered to take place at a much slower rate than liquefaction (Zen and Yamazaki, 1990; Miyamoto et al., 2004). It is therefore reasonable to assume clear different temporal scales for the liquefaction and densification processes. This was used by Miyamoto *et al.* (2004) to identify a solidification front and develop a model to predict its upward propagation. However, when sediment is subject to the action of a random wave time series, the liquefaction is mainly affected by large waves in the time series. In between the time of large waves the sediment bed can experience densification as the pore pressure within the bed may have time to dissipate. In general situation, neither the liquefaction front nor the densification front will maintain a one way movement (up or down). As a result the time scales for the liquefaction and densification processes may not be easily separated as in the regular wave situation. Further studies are required to quantify the cycle of sediment bed behaviour in random waves.

4.4.2 **Probability distribution**

In order to further understand the statistical properties of the predicted liquefaction depth, a number of theoretical distributions are fitted to the numerical distributions including the two parameter Weibull distribution, Rayleigh distribution and Normal distribution. All parameters in the theoretical distributions are calculated using the numerical liquefaction depth data.

4.4.2.1 Regular wave series

Fig. 4.9 and Fig. 4.10 show the probability density function (PDF) and cumulative probability distribution (CPD) of the calculated liquefaction depth for regular wave series together with the theoretical ones for Rayleigh, Normal and Weibull distributions. The probability density function of a two-parameter Weibull random variable x_W is

$$P(x_W, \lambda_W, k_W) = \frac{k_W}{\lambda_W}\left(\frac{x_W}{\lambda_W}\right)^{k_W-1} exp\left[-\left(\frac{x_W}{\lambda_W}\right)^{k_W}\right] \quad (4.6)$$

where λ_W and k_W are scale and shape parameters, and both of them can be estimated by the maximum likelihood estimation method.

If the fluid–soil system is linear, the liquefaction would be expected to have a Rayleigh distribution as the wave height is Rayleigh distributed. The fact that none of the three theoretical distributions seems to fit the entire range of the data indicate that the system is nonlinear. The main sources of nonlinearity include the dispersion relationship in the liquefied layer and plastic volumetric strain terms. It is of interest to note that the fit in the larger value range seems to be better for all three distributions, indicating the usefulness of these theoretical distributions for extreme analysis.

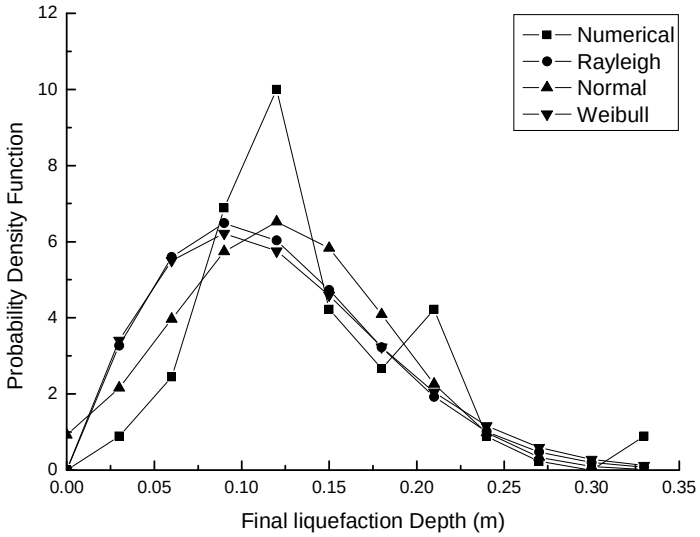

Fig. 4.9 Probability density function of liquefaction depth

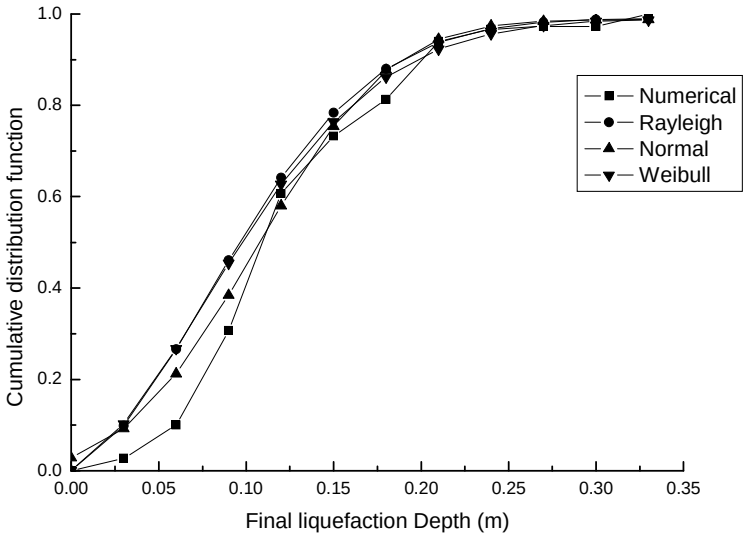

Fig. 4.10 Cumulative distribution function of wave height

4.4.2.2 Random wave series

Fig. 4.11 and Fig. 4.12 illustrate the probability density function (PDF) and cumulative probability distribution (CPD) of the calculated liquefaction depth for the random wave series together with the theoretical PDF and CPD of Normal and Weibull

distributions. The numerical values show a much narrower spread than any of these theoretical distributions. This is to be expected as the differences in predicted liquefaction depth in this case is caused by a small random sequencing effect and the size and number of largest waves in each wave height time series are similar although occurring at different time. The values within a certain range are more or less equally likely to occur and therefore none of the theoretical distributions assessed are applicable to this situation. This conclusion can also be deduced from the histogram of the time to the maximum liquefaction depth. As shown in Fig. 4.6, the time to maximum liquefaction depth is fairly evenly distributed indicating that it is nearly equally likely over a wide range of time.

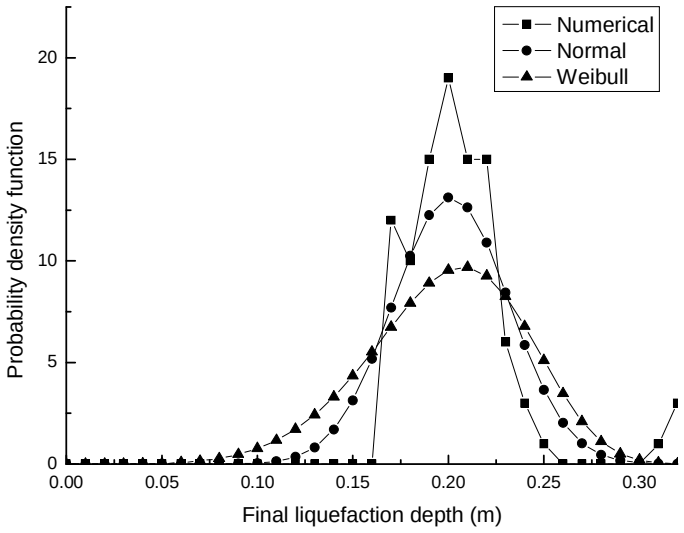

Fig. 4.11 Probability density function of liquefaction depth

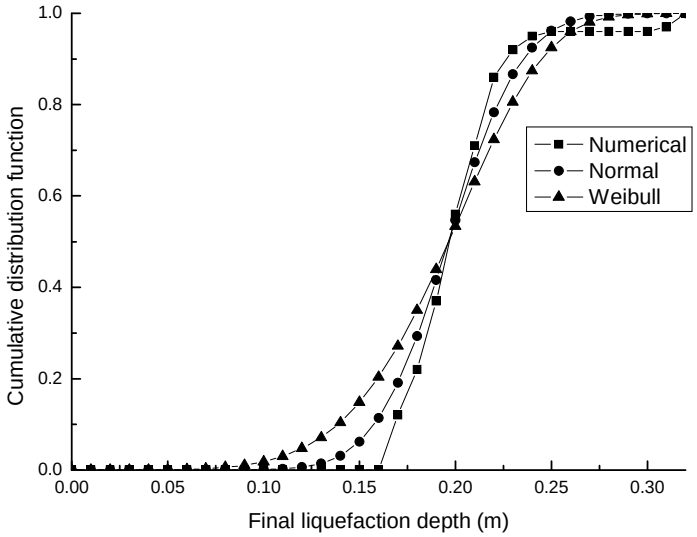

Fig. 4.12 Cumulative distribution function of liquefaction depth

4.5 Engineering implications

As shown by Liu and Jeng (2007) for oscillatory pore pressure, the ensemble modelling results presented above indicate that random wave-induced excess pore pressure and the maximum liquefaction depth also exceed that for the comparable regular waves. This means that the conventional approach of using a representative wave corresponding to the mean value of random waves to determine liquefaction potential could underestimate the maximum liquefaction depth and produce unsafe design in engineering practice. One way of solving this problem is to use extreme waves with higher exceedance probability in the wave height distribution instead of mean values such as significant wave height or root-mean-square wave height. Alternatively, an ensemble modelling similar to what has been done in this chapter should be carried out so as to provide a probability distribution of the liquefaction depth. If the soil parameters or model parameters are deemed to be uncertain and could be given in

probability form they can also be included in the ensemble modelling to cover the full random parameter spaces.

4.6 Summary

A probabilistic study of soil liquefaction processes has been carried out employing ensemble modelling techniques. Two types of ensemble modelling were performed using wave heights randomly sampled from a prescribe Rayleigh distribution, one involving multiple runs of the liquefaction model using regular wave series and the other with random wave series. Based on these multiple runs of the liquefaction model the liquefaction depth and time to the maximum liquefaction are determined in the form of probability distributions so as to reveal the variability and uncertainties involved in predicting wave-induced liquefaction.

The numerical results indicate that for both types of modelling the random wave-induced liquefaction depth is much larger than that corresponding to regular waves with Equivalent Wave Height. The larger liquefaction depth in random waves appears due to the fact that the highest waves rather than average waves in the wave series tend to dominate the liquefaction extent. It is also shown that the time needed for liquefaction to reach bottom of investigated domain can vary considerably in the case of random wave time series. The longer period of low waves between the large waves will delay the time for the maximum liquefaction depth to be reached within the simulation time considered.

One of the main summaries of this work is that the current design practice, which is entirely based on the regular wave models can under-estimate the liquefaction depth and lead to unsafe design. The evaluation of liquefaction potential due to random waves

needs to be based on the appropriate extreme values in the wave height distribution rather than average values such as significant wave height or root-mean-square wave height. It should be pointed out that this finding is based entirely on the numerical model used and needs to be validated by experimental data obtained under fully controlled environment as the prediction is extremely sensitive to the soil and model parameters used.

Finally, in random waves soil densification may occur within the same time frame of liquefaction rather than in the post-liquefaction stage as in regular waves. It is unclear how these two processes interact in random waves. Further work, including both theoretical analysis and field measurements are clearly required to better understand and predict random wave-induced liquefaction and associated risks.

Chapter 5 Two-layer Viscous Fluid Model

5.1 Introduction

In the model used in the previous two chapters, liquefied soil is viewed as inviscid fluid. However, as reviewed in Chapter 1, the liquefied soil is more accepted to be a heavy viscous fluid. Hwang *et al.* (2006) measured viscosity of liquefied sand by the sinking ball and the pulling bar tests, confirmed that the liquefied sand behaves as non-Newtonian fluid whose viscosity decreases with increasing shear strain rate. Hamada and Wakamatsu (1998) made extensive earthquake-induced ground displacement investigation, and concluded that liquefied soil behaves as a pseudo plastic fluid during ground flow; however, it returns to behave as a solid body as stiffness recovers due to dissipation of pore water pressure. In other words, there exists a phase transition for liquefied soil from relatively rigid viscous to purely viscous fluid. Due to the complexity of liquefied soil behaviour, no mature model is available in the literature that takes into account this phase change. Lamb's two-layer fluid system is clearly not applicable for the viscous liquefied soil.

To allow the inclusion of viscosity of liquefied soil, Liu *et al.* (2009) adopted the laminar linearized Navier-Stokes equations to describe the fluid motion which is firstly employed by Dalrymple and Liu (1978) in modelling wave-fluid mud interaction. Furthermore, the wave-induced shear stress was estimated by an analytical solution for a seabed with finite thickness. It was found that the inclusion of the viscosity of the liquefied layer will reduce the predicted final liquefaction depth while the finite depth solution for the shear stress increases the predicted final liquefaction depth.

In this chapter, a two-layer viscous fluid system is constructed. To account for the shear strain rate-dependent viscosity and phase transition of liquefied soil, a visco-elastic–plastic model employed by Oveisy *et al.* (2009) for fluid mud is used as a first approximation. The computed viscosity compared well with the laboratory experimental data in literature. Simulation results demonstrated that the progressive liquefaction was significantly affected by the varying liquefied soil viscosity. Furthermore, the effects of other factors within the present prediction framework, such as wave parameters and soil properties were also examined.

5.2 System definition and formulation

Consider a progressive water wave with a wave length L and wave period T that propagates over a cohesion-less sediment bed. Suppose the liquefaction occurs at time t, and its front progresses down to a location $z = z_L$ as depicted in Fig. 5.1. The entire system consists of two viscous fluid layers, seawater with density ρ_1 ($0 \leq z \leq h$) and liquefied soil with density ρ_2 ($z_L \leq z \leq 0$), respectively; and a poro-elasto-plastic sub-liquefied layer ($-D \leq z \leq z_L$). In this model, the density of each layer is assumed to be constant. Before the liquefaction, the analytical solution for linear wave pressure on water-seabed-interface is used to assess the excess residual pressure in the seabed; after the onset of liquefaction, the upper fluid layers are formulated first and then the lower soil subsystem.

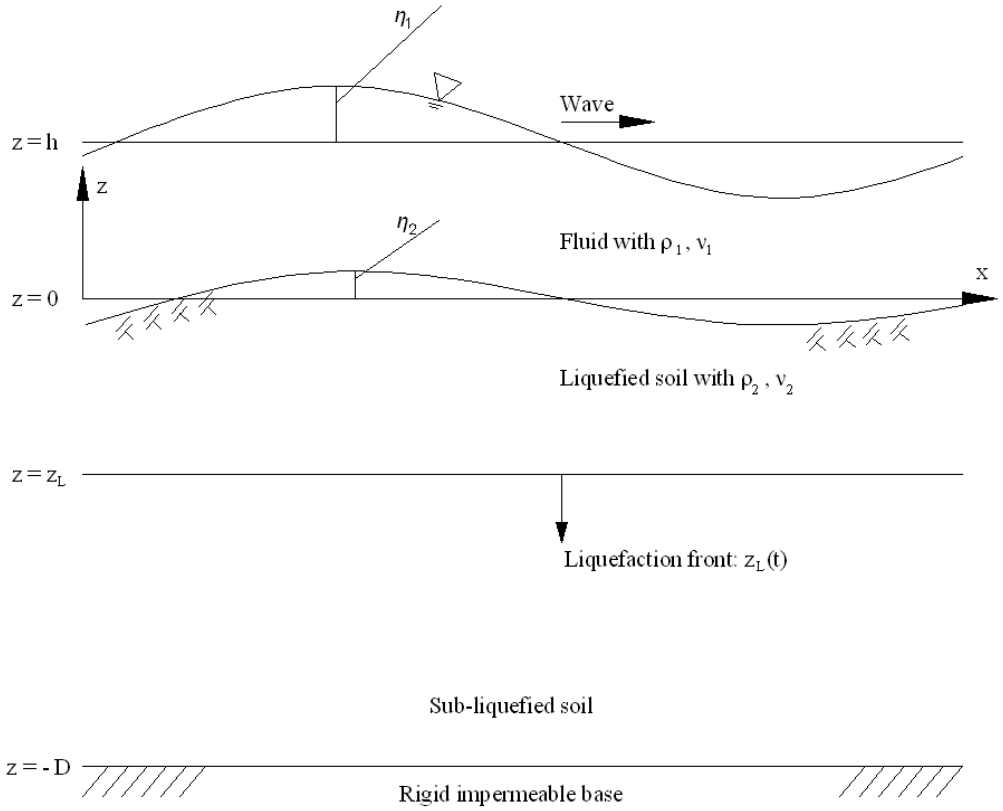

Fig. 5.1 Schematic definition of wave induced progressive seabed liquefied seabed (incorporating viscosity)

5.2.1 **Formulation for the fluid zone**

5.2.1.1 Wave-liquefied soil interaction model

Dalrymple and Liu (1978) developed a two-layer fluid model for wave propagation over a viscous mud layer thus overcoming the limitation of Lamb's model. The laminar Navier–Stokes equations for incompressible fluid, which has been linearized by neglecting convective acceleration, are (MacPherson, 1980)

$$\frac{\partial \hat{u}_j}{\partial t} = -\frac{1}{\rho_j}\frac{\partial \hat{p}_j}{\partial x} + \nu_j\left(\frac{\partial^2 \hat{u}_j}{\partial x^2} + \frac{\partial^2 \hat{u}_j}{\partial z^2}\right) \tag{5.1}$$

$$\frac{\partial \hat{w}_j}{\partial t} = -\frac{1}{\rho_j}\frac{\partial \hat{p}_j}{\partial z} + \nu_j\left(\frac{\partial^2 \hat{w}_j}{\partial x^2} + \frac{\partial^2 \hat{w}_j}{\partial z^2}\right) \tag{5.2}$$

where $\hat{u}$, $\hat{w}$ are the horizontal and vertical velocities, respectively; the subscript j indicates the layer index; x and z are the horizontal and vertical coordinates, respectively; $\hat{p}$ is the dynamic pressure; ρ is the density of fluid; and $\nu = \mu/\rho$ is kinematic viscosity with the subscripts $j = 1, 2$ indicating the upper and lower layers, respectively; t represent the time.

The equations for mass conservation is

$$\frac{\partial \hat{u}_j}{\partial x} + \frac{\partial \hat{w}_j}{\partial z} = 0 \tag{5.3}$$

The periodic solutions for $\hat{u}_j$, $\hat{w}_j$ and $\hat{p}_j$ are assumed respectively as

$$\hat{u}_j(x, z; t) = u_j(z)\exp[i(\kappa x - \omega t)] \tag{5.4}$$

$$\hat{w}_j(x, z; t) = w_j(z)\exp[i(\kappa x - \omega t)] \tag{5.5}$$

$$\hat{p}_j(x, z; t) = p_j(z)\exp[i(\kappa x - \omega t)] \tag{5.6}$$

where ω is angular frequency of the wave system and κ is the unknown complex wave number after liquefaction

$$\kappa = \kappa_r + i\kappa_i \tag{5.7}$$

κ_r is the real part of the wave number which provides the wavelength ($L = 2\pi/\kappa_r$); κ_i is the imaginary part which represents the wave attenuation rate. Displacements of water surface and interfaces, η_j are represented by

$$\eta_j = a_j \exp[i(\kappa x - \omega t)] \tag{5.8}$$

where a_j is a complex unknown value defining the amplitude of the displacement of the jth layer. The water surface is expressed as η_1 while η_2 is unknown complex value representing liquefied layer displacement including their amplitudes and phases. Substituting Eqs. (5.4), (5.5) and (5.6) into the continuity Eq. (5.3) results in

$$u_j = \frac{i}{\kappa}\frac{\partial w_j}{\partial z} \tag{5.9}$$

where the prime represents the differential with respect to z. Introduction of Eq. (5.9) into Eq. (5.1) yields an expression for p_j

$$p_j = \frac{\rho_j \nu_{e,j}}{\kappa^2}\left(\frac{\partial^3 w_j}{\partial z^3} - \lambda_j^2 \frac{\partial w_j}{\partial z}\right) \tag{5.10}$$

in which

$$\lambda_j^2 = \kappa^2 - i\sigma\nu_{e,j}^{-1} \tag{5.11}$$

Substituting p_j into the vertical momentum equation, Eq. (5.2), yields the fourth-order differential equation for w_j

$$\frac{\partial^4 w_j}{\partial z^4} - \left(\kappa^2 + \lambda_j^2\right)\frac{\partial^2 w_j}{\partial z^2} + \kappa^2 \lambda_j^2 w_j = 0 \tag{5.12}$$

The general solutions of Eq. (5.12) can be obtained as

$$w_1(z) = Ae^{\kappa z} + Be^{-\kappa z} + Ce^{\lambda_1 z} + De^{-\lambda_1 z} \tag{5.13}$$

$$w_2(z) = Ee^{\kappa(z+z_L)} + Fe^{-\kappa(z+z_L)} + Ge^{\lambda_2(z+z_L)} + He^{-\lambda_2(z+z_L)} \tag{5.14}$$

The complex constants A, B, C, D, E, F, G, H and the unknown variables κ and a_2 are determined from the boundary conditions at the water surface, the interfaces and the rigid bottom as follows:

(a) At the water surface ($z = \eta_1$)

The kinematic boundary condition, requiring the surface particles to follow the surface, and the imposition of zero normal and tangential stresses can be written as

$$\frac{\partial \eta_1}{\partial t} = \widehat{w}_1 \tag{5.15}$$

$$\hat{p}_1 - 2\rho_1 \nu_1 \frac{\partial \widehat{w}_1}{\partial z} = 0 \tag{5.16}$$

$$\rho_1 \nu_1 \left(\frac{\partial \hat{u}_1}{\partial z} + \frac{\partial \widehat{w}_1}{\partial x} \right) = 0 \tag{5.17}$$

or after Taylor's expansion

$$Ae^{\kappa h} + Be^{-\kappa h} + Ce^{\lambda_1 h} + De^{-\lambda_1 h} = -i\omega a_1 \tag{5.18}$$

$$M_1(Ae^{\kappa h} - Be^{-\kappa h}) - 2\rho_1 \nu_1 \lambda_1 \left[Ce^{\lambda_1 h} - De^{-\lambda_1 h} \right] = \rho_1 g a_1 \tag{5.19}$$

$$2\kappa^2(Ae^{\kappa h} + Be^{-\kappa h}) + (\lambda_1^2 + \kappa^2)\left(Ce^{\lambda_1 h} + De^{-\lambda_1 h} \right) = 0 \tag{5.20}$$

where

$$M_1 = \frac{i\rho_1 \omega}{\kappa} - 2\rho_1 \nu_1 \kappa \tag{5.21}$$

$$\lambda_1^2 = \kappa^2 - i\omega\nu_1^{-1} \tag{5.22}$$

and g is the gravitational acceleration.

(b) At the interfaces ($z = 0$)

$$\frac{\partial \eta_2}{\partial t} = \hat{w}_1 \tag{5.23}$$

or

$$A + B + C + D = -i\omega a_2 \tag{5.24}$$

The continuity of horizontal and vertical velocities is

$$\hat{u}_1 = \hat{u}_2 \tag{5.25}$$

$$\hat{w}_1 = \hat{w}_2 \tag{5.26}$$

or

$$A + B + C + D = Ee^{\kappa z_L} + Fe^{-\kappa z_L} + Ge^{\lambda_2 z_L} + He^{\lambda_2 z_L} \tag{5.27}$$

$$\kappa A - \kappa B + \lambda_1 C - \lambda_1 D = \kappa Ee^{\kappa z_L} - \kappa Fe^{-\kappa z_L} + \lambda_2 Ge^{\lambda_2 z_L} - \lambda_2 He^{\lambda_2 z_L} \tag{5.28}$$

The normal and tangential stresses are also continuous across the interfaces.

$$\hat{p}_1 - 2\rho_1\nu_1\frac{\partial \hat{w}_1}{\partial z} - \rho_1 g\eta_2 = \hat{p}_2 - 2\rho_2\nu_2\frac{\partial \hat{w}_2}{\partial z} - \rho_2 g\eta_2 \tag{5.29}$$

$$\rho_1\nu_1\left(\frac{\partial \hat{u}_1}{\partial z} + \frac{\partial \hat{w}_1}{\partial x}\right) = \rho_2\nu_2\left(\frac{\partial \hat{u}_2}{\partial z} + \frac{\partial \hat{w}_2}{\partial x}\right) \tag{5.30}$$

or

$$M_1(A-B) - 2\rho_1\nu_1\lambda_1(C-D) = M_2(Ee^{\kappa z_L} - Fe^{-\kappa z_L}) - 2\rho_2\nu_2\lambda_2\left(Ge^{\lambda_2 z_L} - He^{\lambda_2 z_L}\right) - (\rho_2 - \rho_1)ga_2 \tag{5.31}$$

$$\rho_1\nu_1[2\kappa^2(A+B) + (\lambda_1^2 + \kappa^2)(C+D)] = \rho_2\nu_2\left[2\kappa^2(Ee^{\kappa z_L} + Fe^{-\kappa z_L}) + (\lambda_1^2 + \kappa^2)\left(Ge^{\lambda_2 z_L} + He^{\lambda_2 z_L}\right)\right] \tag{5.32}$$

where

$$M_2 = \frac{i\rho_2\omega}{\kappa} - 2\rho_2\nu_2\kappa \tag{5.33}$$

(c) At the bottom ($z = -z_L$)

The velocities in both the horizontal and vertical directions should be zero at the fixed bottom,

$$\hat{u}_2 = 0 \tag{5.34}$$

$$\hat{w}_2 = 0 \tag{5.35}$$

or

$$\kappa(E-F) + \lambda_2(G-H) = 0 \tag{5.36}$$

$$E + F + G + H = 0 \tag{5.37}$$

The coefficients $A-H$, the amplitude of interface wave a_2 and wave number κ can be solved from Eqs. (5.18), (5.19), (5.20), (5.24), (5.27), (5.28), (5.31), (5.32), (5.36) and (5.37) by substitution and iteration methods. The detail derivation of these coefficients can be found in Appendix E of this thesis. Then the amplitude of fluid pressure at the bottom of fluid region can be derived from Eq. (5.10) as

$$p_2|_{z=-z_L} = \frac{i\omega\rho_2}{\kappa}(E-F) \tag{5.38}$$

5.2.1.2 Rheological model of liquefied soil

In centrifuge wave testing, Miyamoto *et al.* (2000) observed that water-seabed-interface starts vibrating as liquefaction occurs, and the oscillation amplitude increased considerably with the advancement of the liquefaction front. As discussed in the preceding sections, due to the complexity of liquefied soil behaviour, different constitutive equations have been proposed. In this thesis, the visco-elastic–plastic model (Oveisy *et al.*, 2009) which was proposed originally for mud is adopted here to describe the evolution of viscosity with the gradually increasing deforming rate of the liquefied soil layer. The state of liquefied soil is determined by comparing shear stress and yield stress. When the shear stress is less than the yield stress, the liquefied soil is in a viscoelastic state; otherwise, it is in a viscoplastic state. The visco-elastic–plastic model is preferred as it can account for the behaviour of liquefied soil at both low and high shear stresses. The constitutive equations are expressed as (Oveisy et al., 2009)

$$\sigma_{ij} = 2\mu_e \dot{e}_{ij} \tag{5.39}$$

$$\mu_e = \begin{cases} \mu_1 + \dfrac{iG}{\omega} & \left(\dfrac{1}{2}\sigma_{ij}\sigma_{ij} \le \tau_y^2\right) \\ \mu_2 + \dfrac{\tau_y}{\sqrt{4|\Pi_e|}} & \left(\dfrac{1}{2}\sigma_{ij}\sigma_{ij} > \tau_y^2\right) \end{cases} \tag{5.40}$$

where i and j take the values 1 and 2 which correspond to the x and z axes, respectively, σ_{ij} is the deviator part of stress tensor, μ_e is the apparent viscosity, $\dot{e}_{ij}$ is the deviator part of strain rate tensor, ω is the angular frequency of the wave, G is the elastic modulus, μ_1 is the viscosity of liquefied soil in the viscoelastic state, μ_2 is the viscosity of liquefied soil in the viscoplastic state and τ_y is the yield stress. $|\Pi_e|$ is the objective of the deformation-rate tensor and is expressed as

$$|\Pi_e| = \frac{1}{2}\left(\frac{\partial \hat{u}}{\partial x}\right)^2 + \frac{1}{2}\left(\frac{\partial \hat{w}}{\partial z}\right)^2 + \frac{1}{4}\left(\frac{\partial \hat{u}}{\partial z} + \frac{\partial \hat{w}}{\partial x}\right)^2 \tag{5.41}$$

where $\hat{u}$ and $\hat{w}$ are the horizontal and vertical component of velocity, respectively. The rheological viscoelastic parameters, i.e. shear modulus and viscosity, are taken from the results of the laboratory experiments of (Shibayama, 1993) on commercial kaolinite

$$\mu_1 = 10^{\left(3.353 - 9.56\times10^{-3}W\right)} \times T \tag{5.42}$$

$$\begin{aligned} logG = {} & 3.761 - 1.05 \times 10^{-2}W \\ & + (0.147 - 3.38 \times 10^{-3}W)log(T - 0.522 - 1.23 \\ & \times 10^{-3}W) \end{aligned} \tag{5.43}$$

in which μ_1 is the viscosity ($Pa\ s$), T is wave period (s) and W is the mass water content ratio (referred to water content in the thesis for simplicity) of the liquefied soil (%).

Note that μ_e is related to water content of liquefied soil and wave period. It seems this complex viscosity includes the effect of wave attenuation, in a similar way as application of complex shear modulus by Yamamoto and Takahashi (1985) to consider wave dissipation.

The visco-plastic parameters of kaolinite (i.e. τ_y andμ_2) are evaluated from the laboratory experiments of Tsuruya *et al.* (1987).

$$\tau_y = 1.494 \times 10^6 W^{-2.452} \tag{5.44}$$

$$\mu_2 = 8.465 \times 10^3 W^{-1.344} \tag{5.45}$$

where τ_y, μ_2 are in *Pa* and *Pa s*, respectively.

Due to dearth of corresponding model constants for sand, the parameters originally proposed for clay of kaolinite are employed. The predicted viscosity compares well with the measured data for sand in literature (shown in **Error! Reference source not found.**), which ensures the validity of this approximation. In this rheological model, the viscosity of liquefied soil depends on mass water content ratio, wave period and motion of liquefied soil layer. In reality the shear strain and deformation rate should both be varying with depth but as a first approximation, the average values for both of them are adopted.

5.2.2 **Formulation for sub-liquefied seabed**

To determine the build-up of the residual pore pressure in the sub-liquefied soil layer, the plastic volumetric strain under cyclic wave loading needs to be specified in addition to the fluid conservative equation or storage equation. The development of plastic volumetric strain should reflect the contractive nature of sand bed, which is

related to wave-induced shear stress. Therefore, we need obtain the shear stress in porous seabed prior to constructing the sub-liquefied seabed model which is presented in Chapter two. The cyclic shear stresses are determined by the solution for a bed of finite thickness.

Finite solution for cyclic shear stress

P_0 is the wave pressure before liquefaction, is given by Hsu (1990),

$$P_0 = \frac{\gamma_w m_0}{cosh(k_0 d)} \tag{5.46}$$

The vertical normal effective stress is

$$\sigma'_{v0} = \gamma' z \tag{5.47}$$

A closed form solution for a seabed with finite thickness was given by Jeng and Hsu (1996). For a progressive wave propagating over a fully saturated poro-elastic seabed of finite thickness, the shear stress and wave-induced pore pressure within the seabed are

$$\begin{aligned}\tau = iP_0\{&(C_1 + C_2\kappa_0 z)exp(\kappa_0 z) - (C_3 + C_4\kappa_0 z)exp(-\kappa_0 z) \\ &+ \kappa_0\delta[C_5 exp(\delta z) - C_6 exp(-\delta z)]\}exp[i(\kappa_0 x - \omega t)]\end{aligned} \tag{5.48}$$

$$\begin{aligned}P = \frac{P_0}{1-2\mu}\{&(1-2\mu)[C_2 exp(\kappa_0 z) - C_4 exp(-\kappa_0 z)] \\ &+ (1-2\mu)(\delta^2 - \kappa_0^2)[C_5 exp(\delta z) \\ &+ C_6 exp(-\delta z)]\}exp[i(\kappa_0 x - \omega t)]\end{aligned} \tag{5.49}$$

where

$$\delta^2 = \kappa_0^2 - \frac{i\omega\gamma_w(1-2\mu)}{2Gk_z(1-\mu)} \tag{5.50}$$

in which k_z is soil permeability, G is shear modulus, μ is Poisson's ratio, ω is wave frequency, κ_0 is the wave number before liquefaction. Coefficients $C_1 - C_6$ are shown in Appendix D.

If liquefaction occurs, the shear stress and pore pressure in the seabed can be calculated using Eq. (5.48) and Eq. (5.49). A minor change is that P_0 and κ_0 should be P_L and κ which have to be updated from the two-layer wave model. The vertical normal effective stress can be calculated using Eq. (5.47) and then the shear stress ratio $\chi = \tau/\sigma'_{v0}$ can be further calculated.

5.3 Numerical scheme and computational procedure

By adopting a finite difference method, the governing Eq. (3.20) can be discredited as

$$\begin{aligned} &\frac{U(\xi+\Delta\xi,Z)-U(\xi,Z)}{\Delta\xi} - Mq \\ &= \frac{U(\xi+\Delta\xi,Z+\Delta Z)-2U(\xi+\Delta\xi,Z)+U(\xi+\Delta\xi,Z-\Delta Z)}{(\Delta Z)^2} \end{aligned} \tag{5.51}$$

in which, $q = \partial v^p/\partial\xi$, $Z = \kappa_0 z$, $\Delta\xi$ is the increment of wave cycle, and ΔZ the increment of general depth. Note that we represent $u_e^{(2)}$ by U in Eq. (5.51).

The value of q is determined by Eq. (3.26), which can be calculated using the backward Euler scheme. The left hand side of Eq. (3.26) can be discredited as

$$\frac{\partial v^p}{\partial \xi} = \frac{v^p(\xi,\chi) - v^p(\xi-\Delta\xi,\chi)}{\Delta\xi} \tag{5.52}$$

Thus $v^p(\xi,\chi)$ can be determined based on $v^p(\xi-\Delta\xi,\chi)$,

$$\frac{v^p(\xi,\chi) - v^p(\xi-\Delta\xi,\chi)}{\Delta\xi} = \beta\left[v_\infty^p(\chi) - v^p(\xi,\chi)\right] \tag{5.53}$$

$$v^p(\xi,\chi) = \frac{\beta v_\infty^p(\chi)\Delta\xi + v^p(\xi-\Delta\xi,\chi)}{1+\beta\Delta\xi} \tag{5.54}$$

With the initial condition that the plastic volumetric strain is zero, the value of $v^p(\xi,\chi)$ can be determined and then q can be calculated for each step.

Considering the boundary conditions at the fluid–soil interface and assuming an impermeable bottom together with dividing the seabed thickness *D* into a mesh of $n \times \Delta z$, Eq. (5.51) can be transformed into

$$\begin{bmatrix} 1 & 0 & \cdots & \cdots & \cdots & \cdots & 0 \\ \mathrm{A} & \mathrm{B} & \mathrm{A} & 0 & \cdots & \cdots & \vdots \\ 0 & \mathrm{A} & \mathrm{B} & \mathrm{A} & 0 & \cdots & \vdots \\ \vdots & \ddots & \ddots & \ddots & \ddots & & \vdots \\ \vdots & & \ddots & \ddots & \ddots & \ddots & \vdots \\ \vdots & & & 0 & \mathrm{A} & \mathrm{B} & \mathrm{A} \\ 0 & & & & 0 & \mathrm{A} & \mathrm{B}^* \end{bmatrix} \begin{Bmatrix} U_1 \\ U_2 \\ U_3 \\ \vdots \\ \vdots \\ U_{\mathrm{n}} \\ U_{\mathrm{n+1}} \end{Bmatrix}_{\xi+\Delta\xi} = \begin{Bmatrix} -\gamma' \mathrm{z_L} \\ U_2 \\ U_3 \\ \vdots \\ \vdots \\ U_{\mathrm{n}} \\ U_{\mathrm{n+1}} \end{Bmatrix}_{\xi} + \begin{Bmatrix} 0 \\ \mathrm{Mq} \\ \mathrm{Mq} \\ \vdots \\ \vdots \\ \vdots \\ \mathrm{Mq} \end{Bmatrix}_{\xi} \cdot \Delta\xi \tag{5.55}$$

where

$$A = -\phi\frac{\Delta\xi}{(\Delta Z)^2} \tag{5.56}$$

$$B = 1 + 2\phi\frac{\Delta\xi}{(\Delta Z)^2} \tag{5.57}$$

$$B^* = 1 + \phi \frac{\Delta\xi}{(\Delta Z)^2} \tag{5.58}$$

$$q = \frac{\partial v^p}{\partial \xi}\Big|_{\xi} \tag{5.59}$$

Based on above model, the detailed procedure of the analysis is as follows:

(1) Start analysis from $\kappa = \kappa_0$ $z_L = 0$, $\xi = 0$; calculate initial wave number by water depth and wave period.

(2) Before liquefaction, the wave pressure is calculated by the common formula for a progressive wave: $P_0 = \gamma_f m_0 / cosh(k_0 d)$.

(3) Solve Eq. (5.55) to get the residual pressure at each point for $\xi = \xi + \Delta\xi$.

(4) Repeat steps (2) and (3) until U_2 increases to the value of $\gamma' \Delta z$.

(5) Update the liquefaction front location and vertical effective stress.

(6) In the following steps, the two-layer wave-liquefied soil model is used to calculate κ and the amplitude of fluid pressure over sub-liquefied soil p_L. A trial-and-error approach is used to get a convergent viscosity for liquefied soil. In the first run after onset of liquefaction, a guessed value of a uniform liquefied soil viscosity is used. In the subsequent runs, the viscosity obtained in the last solution is used as trial value. Then, the N-layer fluid system is solved to get shear strain rate of liquefied soil layer and the rheological model equation gives a new viscosity. Repeat this procedure until reach a convergent viscosity.

(7) Input the final viscosity value into the multi-layer system to get the wave pressure at sub-liquefied seabed surface, $z = 0$;

(8) With the wave pressure exerted on seabed surface, the analytical solution of wave-induced shear stress and shear stress ratio are calculated to determine$\partial v^p/\partial \xi$.

(9) Solve Eq. (5.55) to get the residual pore pressure.

(10) Repeat steps (5)–(9) until the end of the analysis.

The solution procedure of the entire system and for determining fluid motion with the two-layer fluid system are summarised in Fig. 5.2 and Fig. 5.3, respectively.

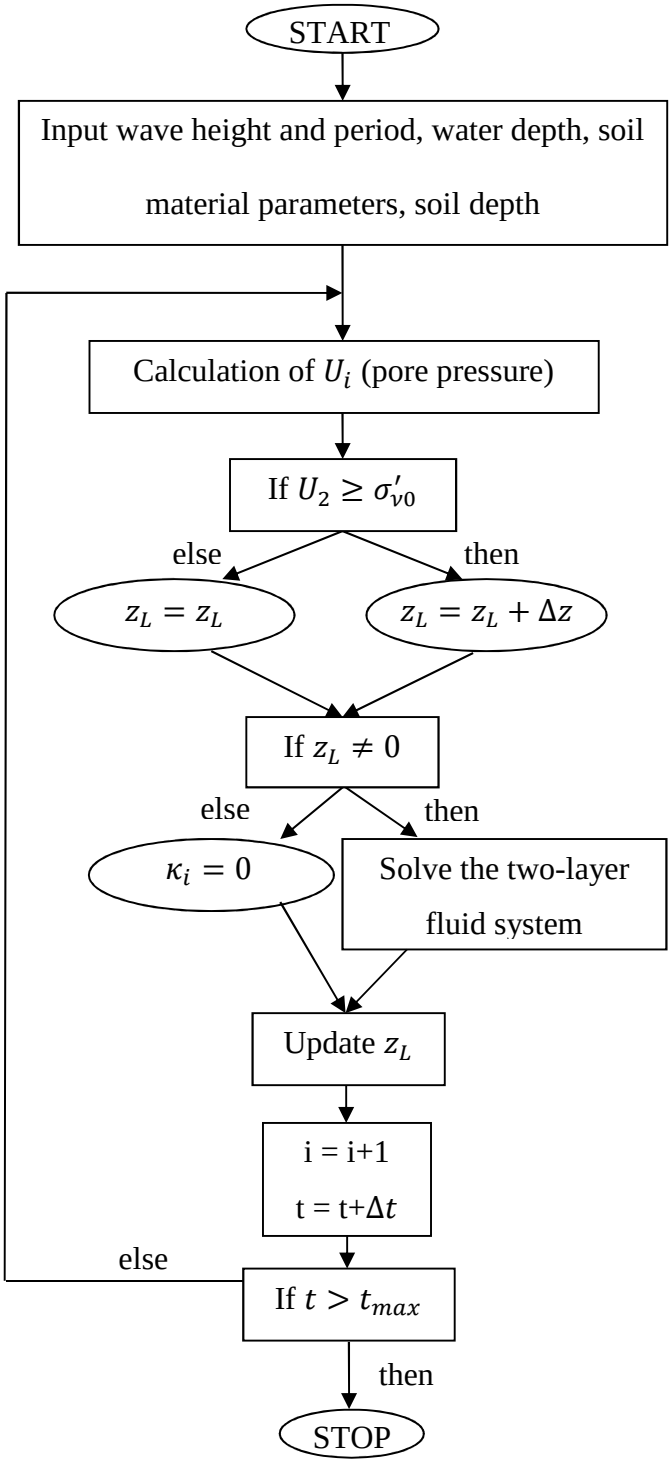

Fig. 5.2 Flowchart for the solving procedure of the entire system

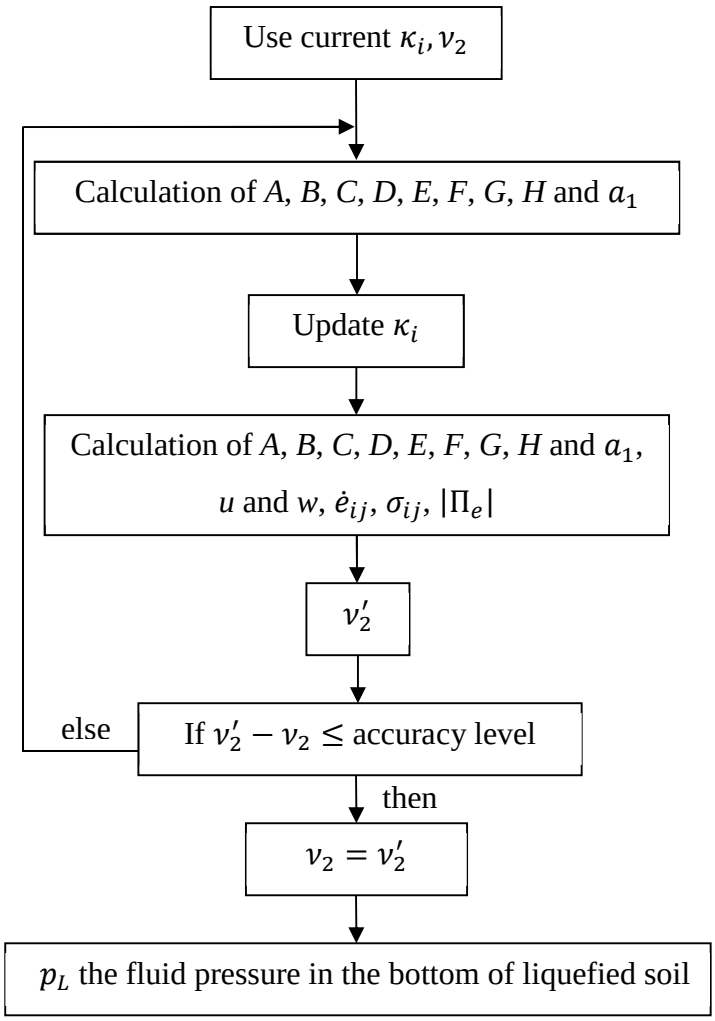

Fig. 5.3 Flowchart for the solving procedure of the two-layer fluid system

5.4 Model performance

5.4.1 Comparison with Liu's model

Prior to examining the effect of visco-elasto-plastic rheological model for liquefied soil, the present model was verified by comparison with simulation results in Liu *et al.* (2009). The results of evolution of liquefaction front are shown in Fig. 5.4 in which 'Model Liu' represents model results given by Liu *et al.* (2009). These results are

obtained by inputting a constant viscosity for liquefied soil into the present model. The parameters used in the case for comparison are listed in Table 5.1. As shown in Fig. 5.4, the present model produced an identical solution to 'Model Liu'.

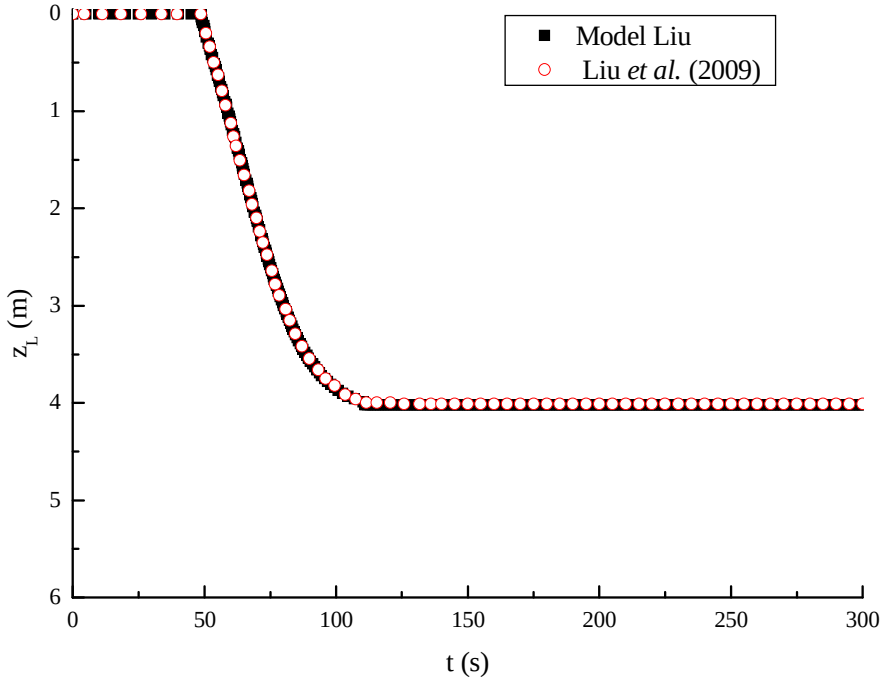

Fig. 5.4 Reproduction of Liu *et al*. (2009)'s results of liquefaction front propagation

Table 5.1 Wave conditions and soil parameters in comparison with Liu *et al.* (2009)

Wave conditions	
Fluid depth, *h*: m	20
Wave period, *T*: s	10
Initial wave length, *L*: m	121.2
Wave height, *H*: m	6.5
$\nu_1 : m^2 s^{-1}$	1×10^{-6}

$\nu_2: m^2 s^{-1}$	10
Soil bed conditions	
Soil depth, *D*: m	6.0
Permeability coefficient, $k_z: ms^{-1}$	1.5×10^{-4}
Density of liquefied soil, $\rho_s: kgm^{-3}$	1800
Water content ratio of liquefied soil, w	42%
$M_D: kPa$	3.12×10^4
R	1.8×10^{-5}
α	55
β	0.04

5.4.2 **Comparison with Oveisy's model**

Since the dynamic viscosity of liquefied soil layer strongly depends on the soil deformation rate, the normalized lateral velocity distribution along depth of liquefied soil layer is tested by comparing with Oveisy's results.

Using the wave characteristic as Case c (Table 5.2) in Oveisy *et al.* (2009), two-layer fluid system was simulated numerically. We chose the seabed depth D so that the final liquefaction depth is roughly equal to mud thickness of case c. Other soil parameters are listed in Table 5.3. The result of normalized lateral velocity of liquefied soil by the value at seabed surface is shown in Fig. 5.5.

In Fig. 5.5, 'Model A' represent the result of present model. Other three curves are reproduced from Oveisy et al. (2009). Regarding these results two points had to be made: ① Although Oveisy presented the viscoelastic-plastic model, a constant viscosity is used when making the comparison with the experiment data and Sakakiyama and Bijker (1988)'s results. ② Oveisy's model is a two dimensional model, but the present model is one-dimensional. In the two dimensional model, the wave height of incident wave is gradually damped as travelling in the lateral direction. However, the initial value wave height is used in the one dimensional model due to the lack of information for wave dissipation. It is probably the reason why the present model results did not completely agree with that of Oveisy's. Better fit between the two predictions is found when $z/d_m \geq 0.5$, z is the vertical location in liquefied layer and d_m is the depth of the layer.

Table 5.2 Wave parameters for Case c in Oveisy *et al.* (2009)

$h: m$	$T: s$	$\rho_s: kgm^{-3}$	$H: m$	$\nu_1: m^2s^{-1}$	$\nu_2: m^2s^{-1}$
0.3	1.02	1230	0.032	1×10^{-6}	1

Table 5.3 Soil parameters used for comparison with Case c in Oveisy *et al.* (2009)

$D: m$	$k_z: ms^{-1}$	$M_D: kPa$	R	α	β
0.3	1.5×10^{-4}	3.12×10^4	1.8×10^{-5}	55	0.04

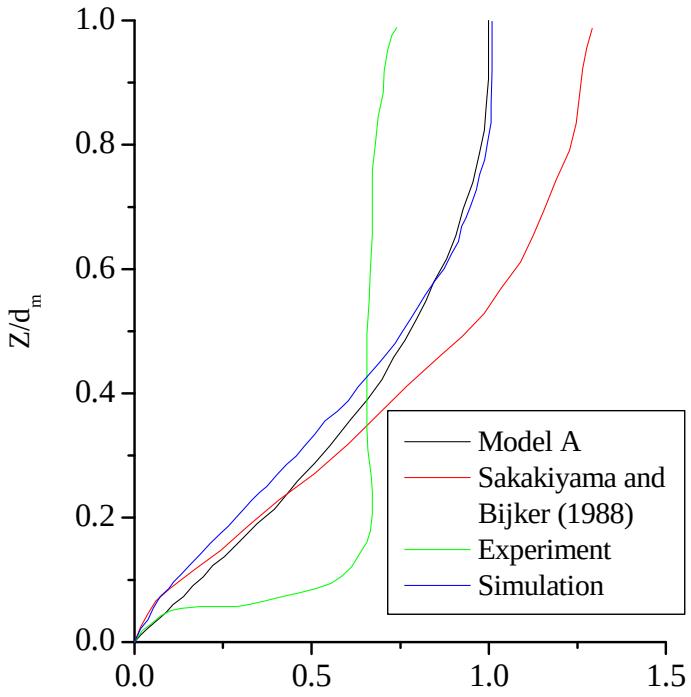

Fig. 5.5 Profile of the velocity in the liquefied layer normalized by u_1, the velocity at the surface of seabed

5.4.3 **Comparison with test results of viscosity**

Hwang *et al.* (2006) have carried out extensive review on the dynamic viscosity of liquefied soil with the main results as shown in **Error! Reference source not found.** and **Error! Reference source not found.**. It can be seen that the major of viscosity data lie within the area between the parallel lines in **Error! Reference source not found.**. In the present model, the dynamic viscosity μ can be estimated using Eq. (5.60)

$$\mu_e = \rho \nu_2 \tag{5.60}$$

where, ρ is the density of liquefied soil, 1800 kgm^{-3}, ν_2 is the kinematic viscosity that obtained from the present model with a value range from 12.52 to 0.09 $m^2 s^{-1}$. The

corresponding values of dynamic viscosity μ_e are from 21,240 to 162 $kPa \cdot s$, which are clearly in reasonable accord with that in **Error! Reference source not found.**.

5.5 Results and discussion

A series of numerical simulations are performed in this section. The wave and soil parameters used are listed in Table 5.1 unless stated otherwise.

5.5.1 Effect of shear stress

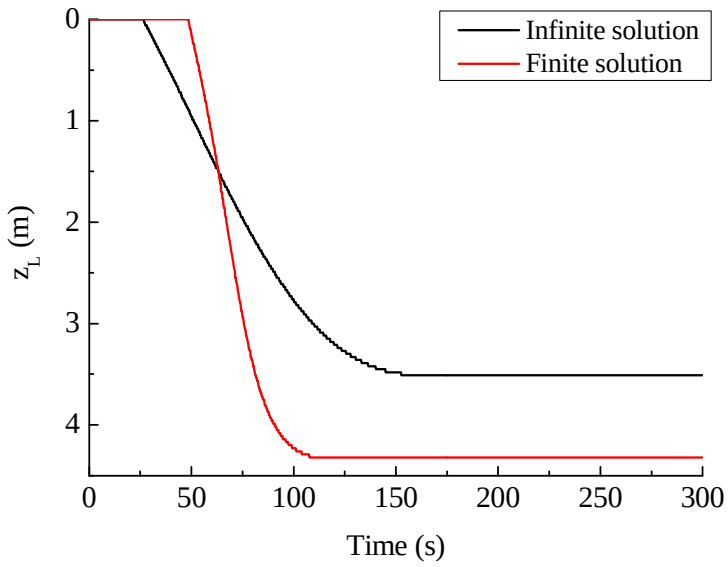

Fig. 5.6 Influence of shear stress solution on liquefaction progresses

Fig. 5.6 reveals that there is a significant difference (exceeding 23%) in the liquefaction front evolution predicted by using different methods to estimate the wave-induced shear stress. 'Finite solution', namely, the shear stress is obtained using the analytical solution for finite thickness seabed, predicts a final liquefaction of 4.32 m while a depth of 3.52 m is computed by infinite solution for shear stress. This can be

explained from two prospects: firstly, shear stress of finite solution is greater than that of infinite solution though the latter is larger in the shallower zone at the beginning of liquefaction phase (as shown in Fig. 5.8). This result is consistent with the earlier occurrence of liquefaction for infinite solution (Fig. 5.6) and the larger amplitude of the displacement on the seabed surface (Fig. 5.7) at earlier liquefaction stage. After this initial period, the finite shear stress exceeds infinite shear stress, and both liquefaction depth and interface wave amplitude, i.e., the amplitude of soil displacement at seabed surface, surpass those of the infinite solutions. Secondly, as the source term in the storage equation involves an exponential function of cyclic stress ratio and coefficient α is positive the influence of a small difference of shear stress and cyclic stress ratio on liquefaction will be amplified.

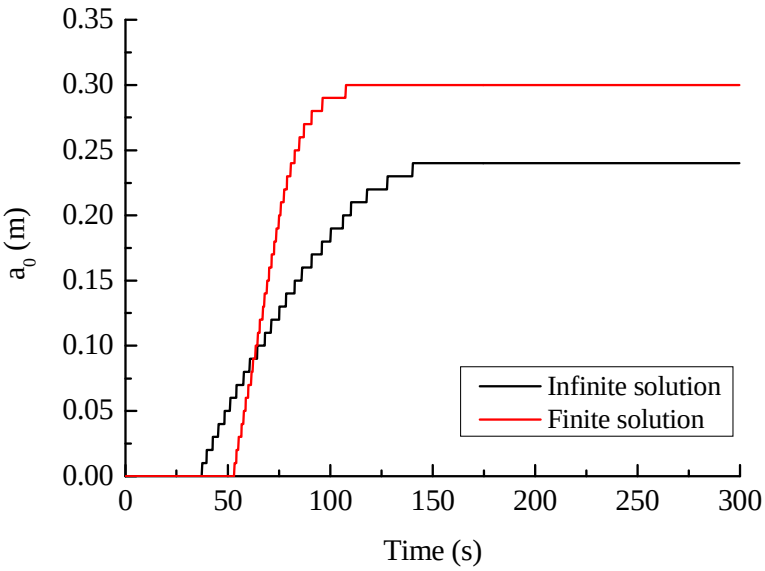

Fig. 5.7 Influence of shear stress solution on amplitude of interface wave

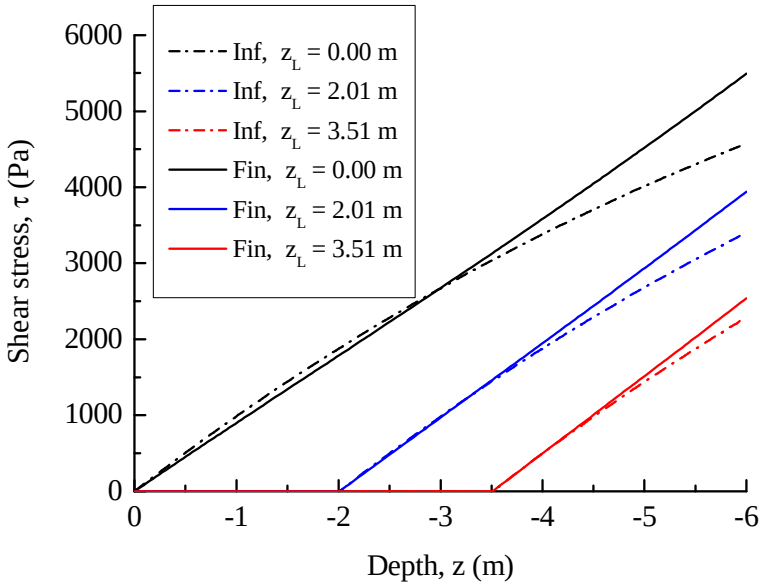

Fig. 5.8 Shear stress from two different solutions: 'Inf' and 'Fin' represent infinite and finite bed solutions, respectively.

5.5.2 **Effect of varying viscosity**

As shown in Fig. 5.9, when visco-elastic-plastic model is employed to model liquefied soil, the maximum liquefaction depth is 4.32m, which is 7.5% deeper than the result obtained by procedure of a constant viscosity (4.02m in Liu *et al.* (2009)). In their model, the viscosity in liquefied soil layer ν_2 was prescribed to 10 $m^2 s^{-1}$. In the present model, ν_2 varies when the liquefaction front moves downward as shown in Fig. 5.10. It decreases from 12.52 to 0.09 $m^2 s^{-1}$ rapidly, and then reaches a steady level. This sharp drop in viscosity models the presumption of transition in the liquefied soil, i.e. the liquefied soil viscosity will transfer from visco-elastic state to visco-plastic state when the deformation rate and associative shear stress rate reach a certain level. This prediction is also consistent with the observed trend of liquefied soil deformation as described in Sassa *et al*. (2001).

As described in the formulation of the visco-elastic-plastic constitutive model, dynamic viscosities of both visco-elastic phase and visco-plastic phase depend on the water content of liquefied soil. Therefore, the effect of water content on the progressive liquefaction is also examined here. The results are shown in Fig. 5.11 and Fig. 5.12.

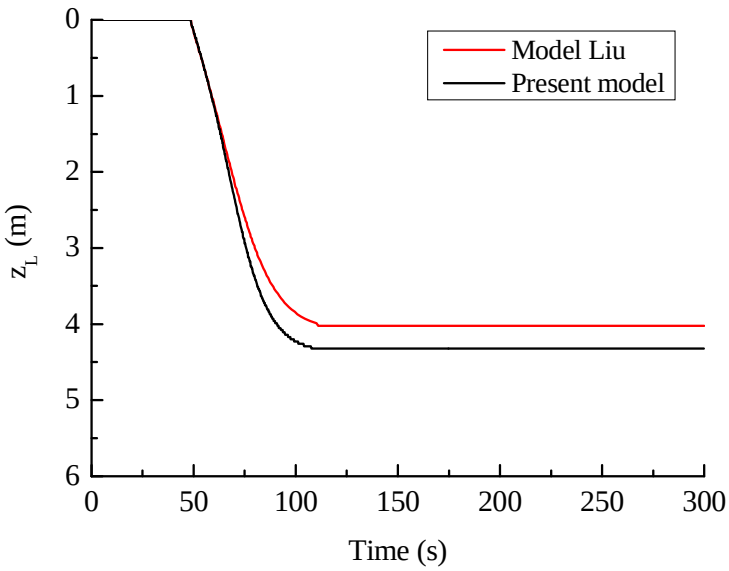

Fig. 5.9 Effect of varying viscosity of liquefied soil on liquefaction front evolution

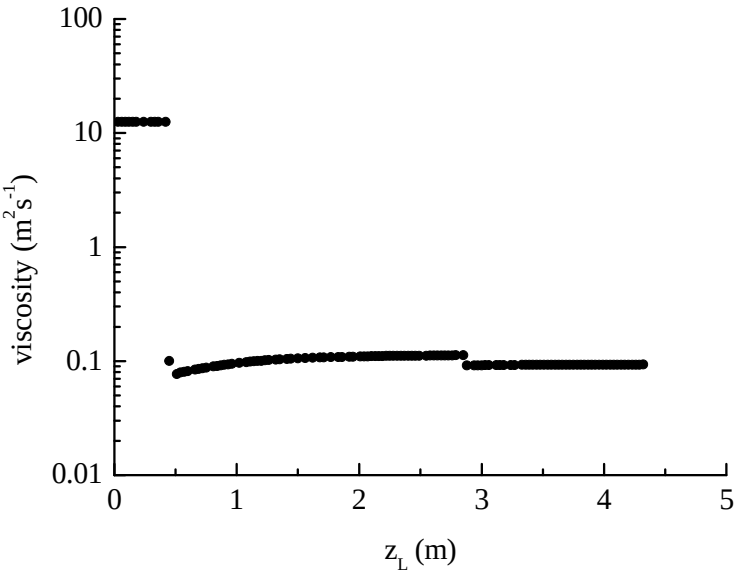

Fig. 5.10 Evolution of kinematic viscosity of liquefied soil with liquefaction depth

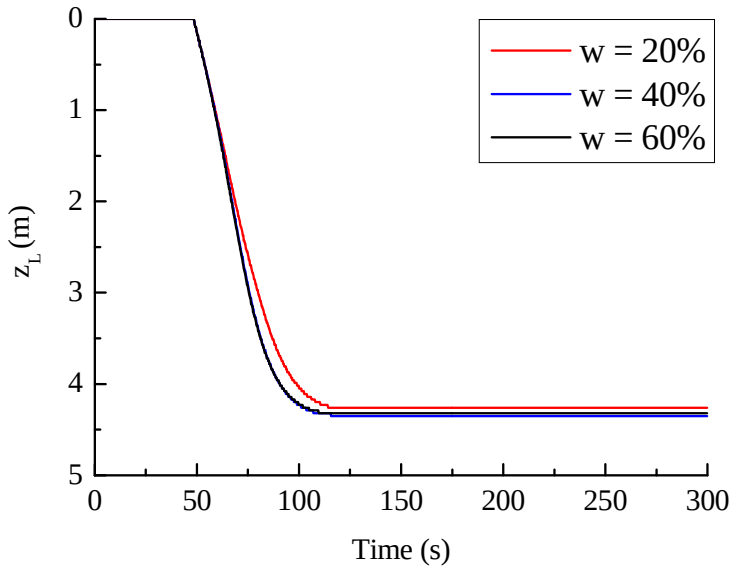

Fig. 5.11 Evolution of liquefaction front with different liquefaction water content

In Fig. 5.11, water content is observed to have no notable influence on the final liquefaction depth. For low water content, from 20% to 40%, increasing water content

causes slightly deeper liquefaction. The viscosity computed for different water content is shown in Fig. 5.12.

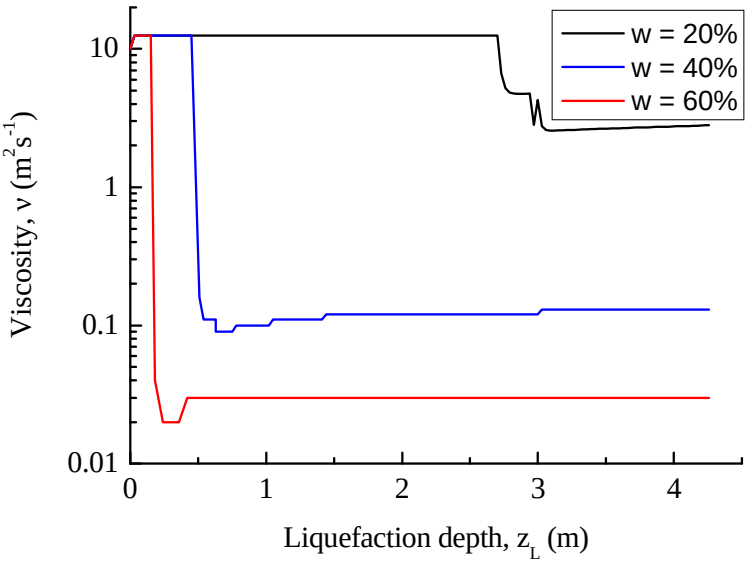

Fig. 5.12 Evolution of kinematic viscosity of liquefied soil with different water content ratio

From Fig. 5.12, we can see higher water content will lead to lower steady viscosity. Moreover, the liquefied soil with higher water content tends to enter visco-plastic state sooner than with lower water content. This can be explained by its lower stiffness. In the framework of constant viscosity and density of liquefied soil layer, Liu *et al.* (2009) discussed the viscosity effect on liquefaction by varying liquefied soil viscosity, ν_2 from 1 to $100 m^2 s^{-1}$. They found that when ν_2 increases from 1 to $10 m^2 s^{-1}$, the liquefaction depth decreases; however, in the range between 10 and $100\, m^2 s^{-1}$, there is no appreciable reduction in predicted liquefaction depth. In the present study, the viscosity varies in a smaller range. Despite the small range, parameter λ in the analytical solution for two-layer fluid system is still expected to show a significant change but this did not happen.

Fig. 5.13 illustrates that the effect of water content on wave pressure is not large although an increase in water content (from 20% to 40%) generally causes an increase in wave pressure. It also shows that after onset of liquefaction, wave pressure at interface between liquefied soil and sub-liquefied soil gradually increases whilst the wave pressure at interface between liquefied soil and overlying water gradually reduces.

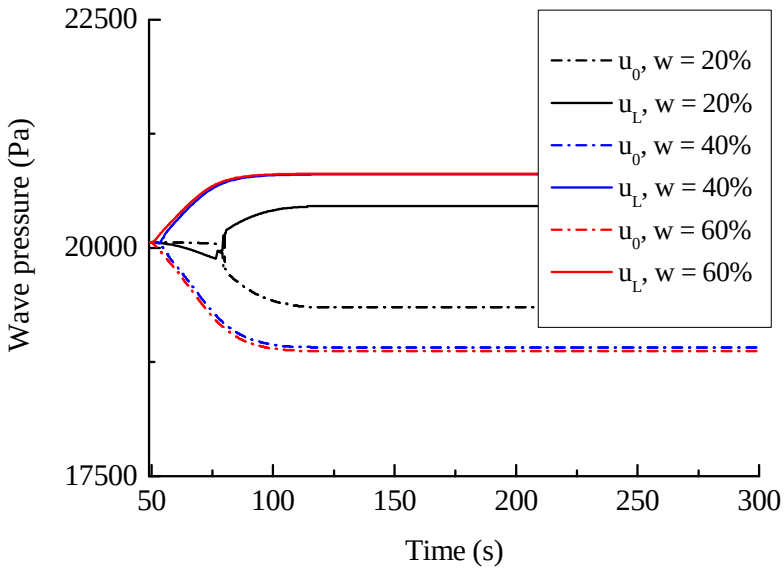

Fig. 5.13 Wave pressure amplitude at location ($z = 0$), u_0 and liquefaction front, ($z = z_{L,}$), u_L.

5.5.3 **Effect of wave and soil characteristics**

Fig. 5.14 demonstrates that the increasing water depth will produce smaller wave pressure and consequently the shear stress ratio and final liquefaction depth will decrease. Also the liquefaction process begins sooner and its front reaches deeper for shallower water depth. Fig. 5.15 depicts the distribution of the source term $M\,\partial v^p/\partial\xi$ in Eq. (3.20) when the liquefaction reaches at 0.24 m, which is the final liquefaction depth for the case with the water depth h equal to 21 m. The source term is found to decrease

for deeper water depth due to the corresponding decreasing shear stress ratio. In turn, the smaller source term prevents the build-up of the residual pore pressure and eventurally results in a shallower liquefaction depth. As shown in Fig. 5.16, when water depth increases, the corresponding viscosity in visco-plastic state increases slightly; however, there is no discernible difference in the viscosity of visco-elastic state.

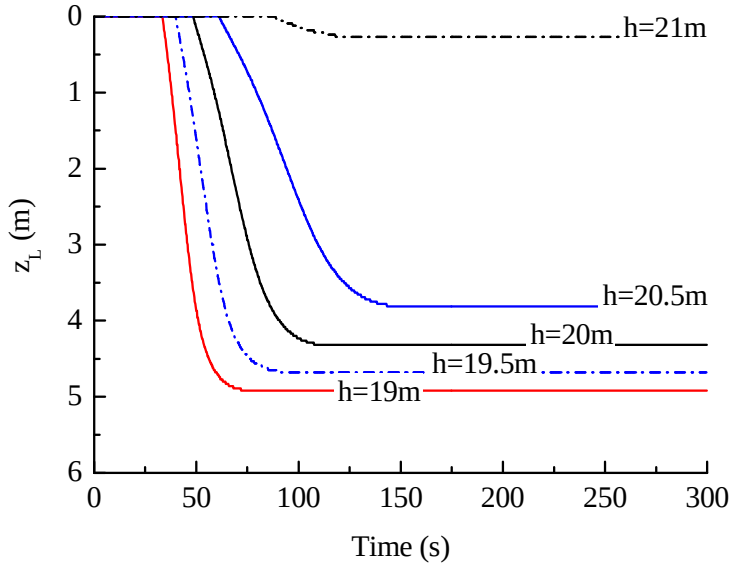

Fig. 5.6 The influence of water depth on liquefaction processes

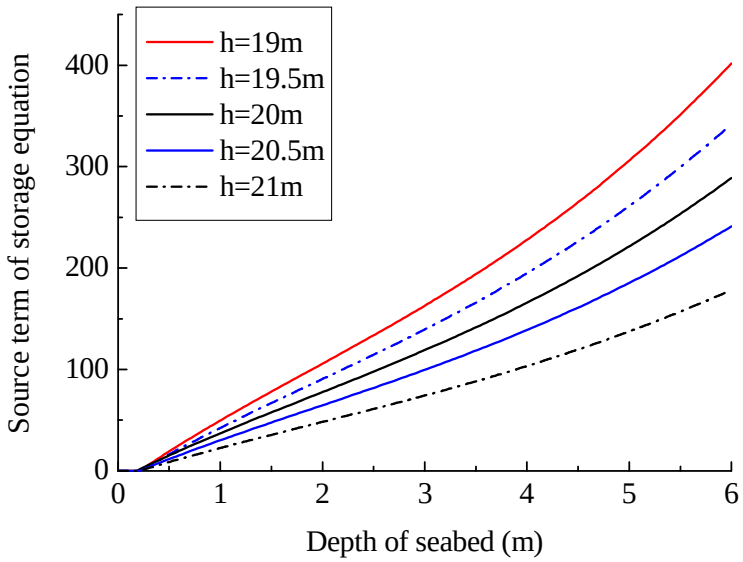

Fig. 5.7 The distribution of source term in the storage equation for various water depth ($z_L = 0.27\ m$)

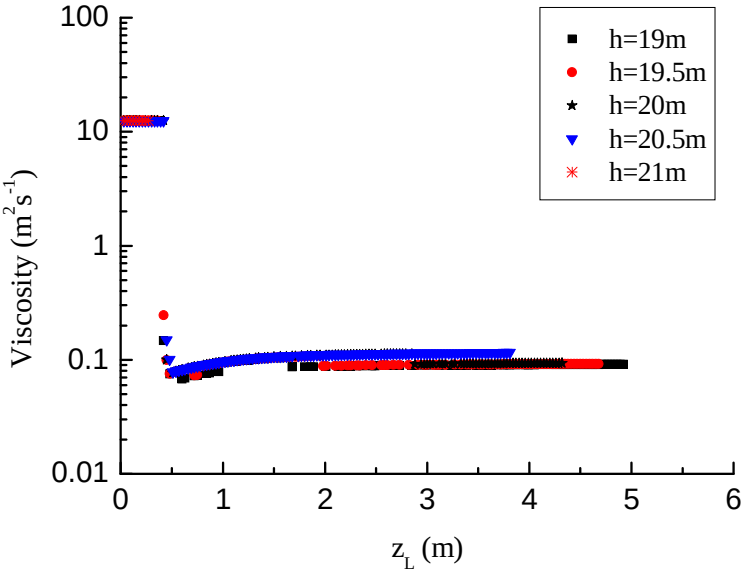

Fig. 5.8 The influence of water depth on viscosity of the liquefied soil

As to the wave period, it affects the wavelength and wave pressure (together with water depth), also the viscosity (but it is not significant as shown in Fig. 5.18). For porous sub-liquefied soil, the partial drainage factor depends on wave angular frequency. The partial drainage controls the rate of residual pressure dissipation as shown by Liu *et al.* (2009). As a result, for a given wave height smaller wave period would lead to deeper liquefaction since the rate of residual pore pressure dissipate is smaller for a shorter wave than for a longer one.

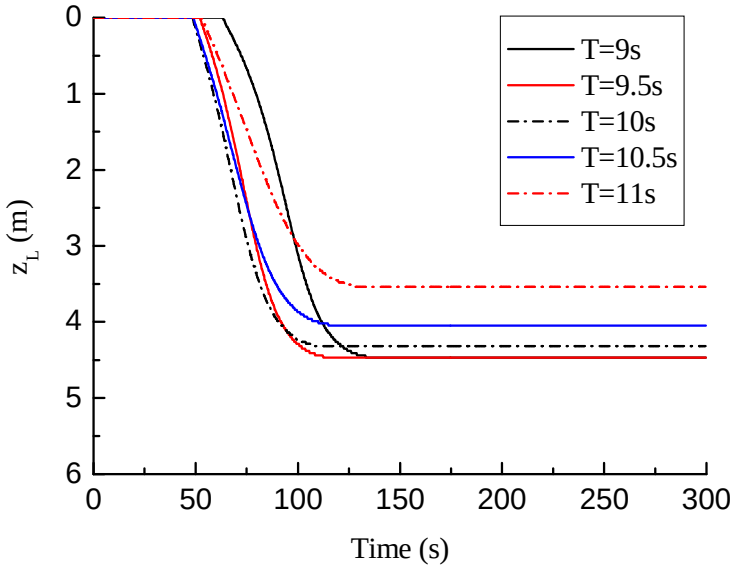

Fig. 5.9 Influence of wave period on liquefaction processes

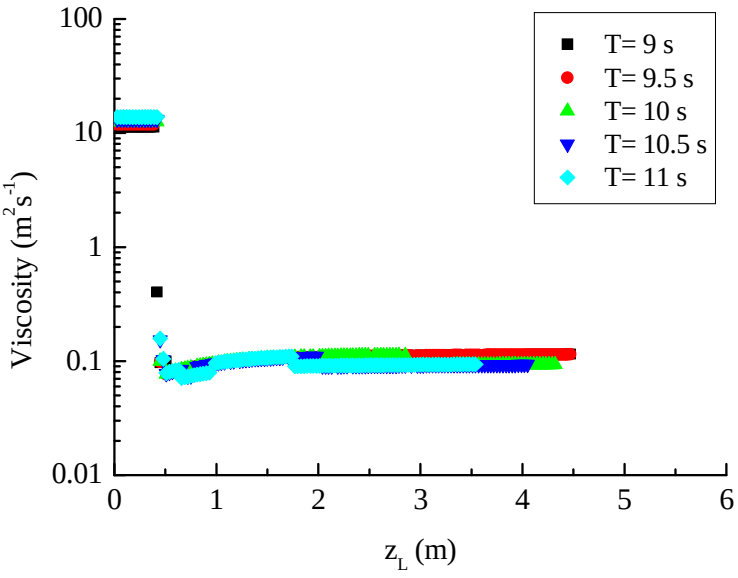

Fig. 5.10 The influence of wave period on viscosity of the liquefied soil

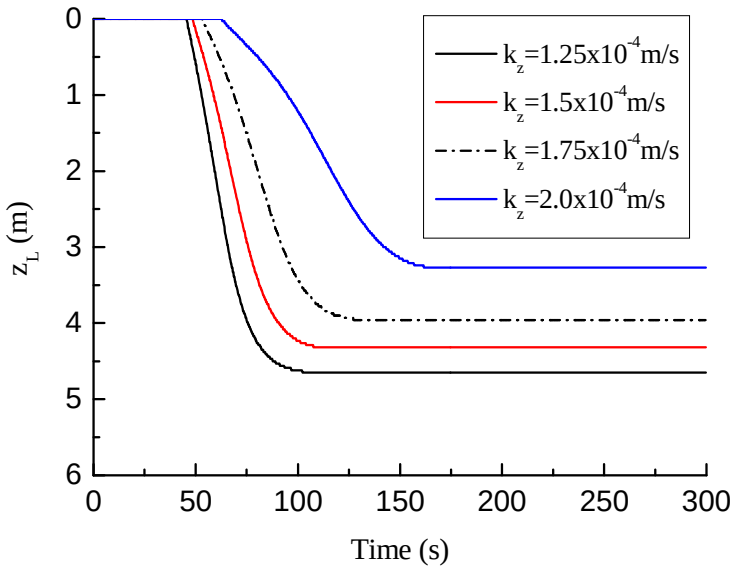

Fig. 5.11 The influence of soil permeability on liquefaction processes

Similarly, the soil permeability which dominants the dissipation rate of residual pore pressure can significantly influences the liquefaction progress. Higher hydraulic conductivity leads to shallower liquefaction depth, as shown in Fig. 5.19.

5.5.4 **Effect of soil poro-plastic parameters α, β and R**

Parameters α, β and R affect the residual pore pressure build-up pattern. Fig. 5.20-Fig. 5.22 demonstrate that both the final liquefaction depth and the liquefaction process are very sensitive to these parameters. Furthermore, the effects of α and β on the final liquefaction depth and the liquefaction process are more significant than that of R. This is because that the former two parameters are exponentially related to the ultimate plastic volumetric strain in Eq. (3.24) and the rate of plastic volumetric change in Eq. (3.25), respectively. However, the ultimate plastic volumetric strain is linearly related to R. Therefore, calibration of these parameters should be done with enough cautions lest use of the uncalibrated model parameters impairs the prediction results completely. However, there is no explicit parametric identification procedure available (Liu *et al.*, 2009). When these parameters were employed originally (Sassa *et al.*, 2001), no definite physical meanings are assigned to them. Actually, they are determined so that the predicted results of liquefaction depth may consistently reproduce the experimental performance.

Alternatively, the built-up of residual pore pressure can be calculated using Eq. (2.7), which models the accumulation pore pressure using the ratio of cyclic loading to the cyclic number to liquefaction by Eq. (2.9). As mentioned in the literature review of Chapter 2, a relationship between $\partial v^p/\partial \xi$ and the source term in the fluid storage equation, f can be achieved by comparing Eq. (2.7) and Eq. (2.15):

$$f = \frac{c_v \mu_r}{K}\frac{dv^p}{dt} = \frac{c_v \mu_r}{K}\frac{\omega}{2\pi}\frac{dv^p}{d\xi} \tag{5.61}$$

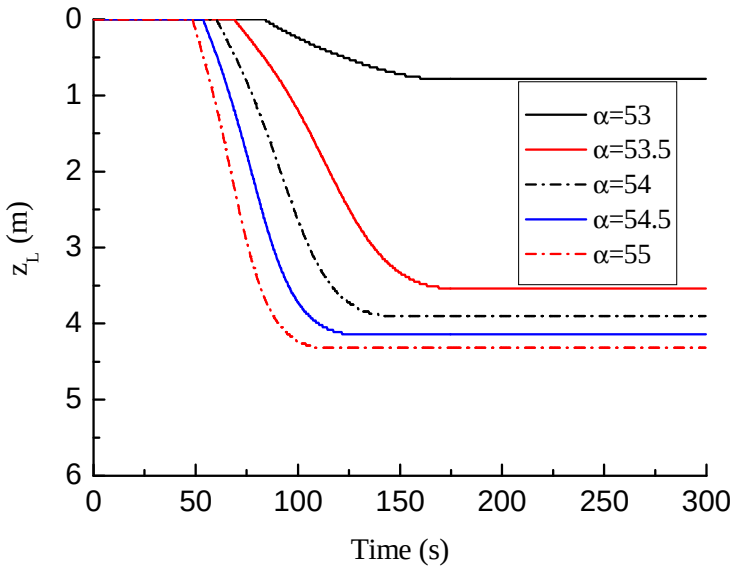

Fig. 5.20 The influence of α on liquefaction processes

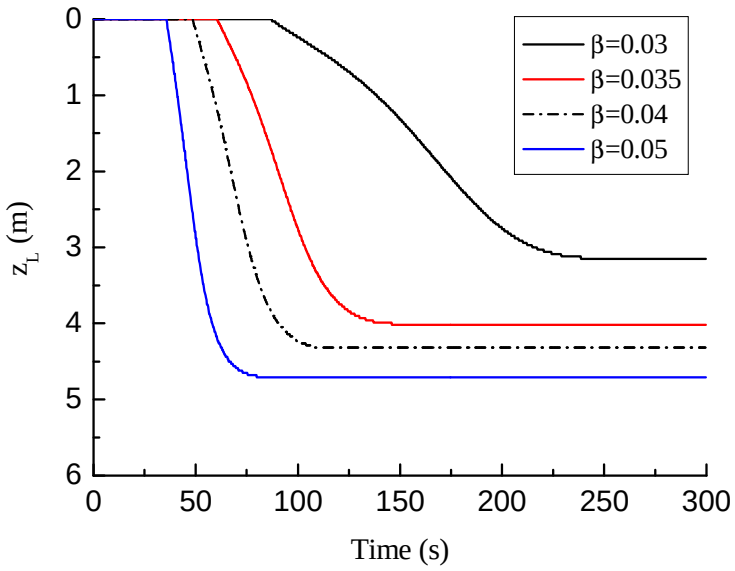

Fig. 5.21 The influence of β on liquefaction processes

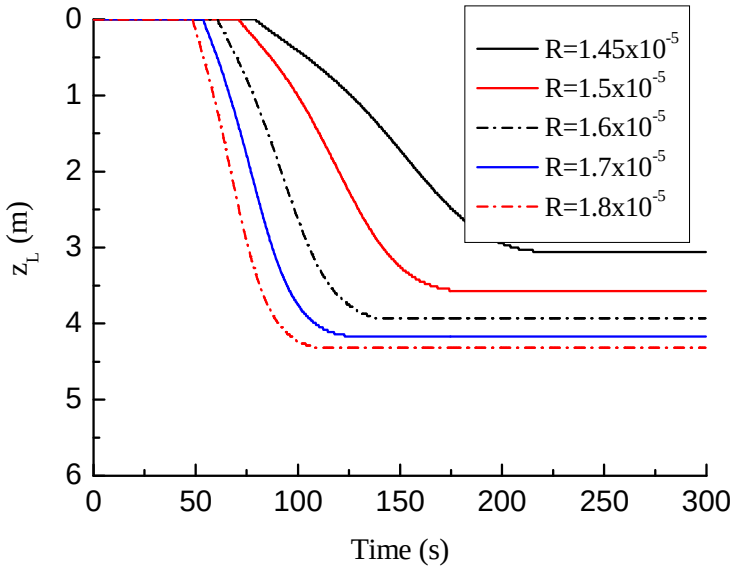

Fig. 5.22 The influence of R on liquefaction processes

5.6 Summary

This chapter presents a model based on visco-elastic-plastic rheological constitutive equation for predicting wave-induced residual liquefaction. The upper seawater and liquefied soil were treated as viscid fluid and described by linearized Navier-Stokes and continuity equation, while the lower sub-liquefied soil was modelled by a poro-elastic-plastic model to calculate residual pore pressure build-up.

Simulation results confirmed that shear stress obtained from infinite seabed solution can lead to significant errors and underestimate the liquefaction depth. The viscosity of liquefied soil computed by the present model shows an abrupt state change, i.e., from viso-elastic stage to visco-plastic stage, due to the accelerating deformation rate of liquefied soil layer. The computed value of viscosity compares well with the test data in the literature. It is found that the shear strain rate dependent viscosity does influence the liquefaction process relative to a constant viscosity, even though this effect is not

particularly marked. Although the rheological parameters depend on both water content of the liquefied soil and wave period, influence of water content on the liquefaction progress seems to be rather limited. However, wave period makes a more notable difference probably because it is more difficult for the residual pore pressure to dissipate under the action of a shorter wave. Effect of the other factors, such as water depth and soil parameters on progressive liquefaction are examined as well. Deeper liquefaction depth is more likely to take place in shallower water under same wave loading. Smaller soil permeability prevents residual pore pressure dissipation and consequently enhances the liquefaction. Finally, the liquefaction is very sensitive to the soil parameters in the source term, which desire a general identification method.

Chapter 6 N-layer Viscid Fluid Model

6.1 Introduction

In Chapter 5, shear strain rate-dependent viscosity of liquefied soil has been confirmed to affect seabed liquefaction progress although not strongly. However, the two-layer fluid system model is based on an approximation of constant viscosity throughout the depth of liquefied soil. This is necessary in the framework of two-layer system in which the entire liquefied soil is assumed to be a uniform layer with respect to the viscosity despite the shear strain rate varies along depth. When the liquefied soil layer is sufficiently thick, this approximation may lead to serious errors.

In investigations of wave dissipation over fluid mud, some researchers have attempted to divide the fluid mud layer to multiple layers to allow the different properties for each sub-layer to be specified (Tsuruya *et al*., 1987; Oveisy *et al*., 2009; Soltanpour and Samsami, 2011). In the situation of fluid mud, the depth of fluid mud is usually known and constant during computation. Therefore, the number of layer can be set and kept unchanged. On the contrary, during progressive liquefaction the liquefaction front advances downward and the thickness (thus number of layers) of sub-layer of liquefied soil therefore changes. In this chapter, the relevant formulas for a multi-layer system are derived and coded based on a recursive procedure to enable an automatically change of the number of liquefied soil layers, thus extending the previous two-layer viscous fluid model to multi-layer or N-layer one. By virtue of N-layer viscid fluid system developed here for the wave-liquefied soil interaction, both density and

viscosity of liquefied soil are allowed to vary with depth, whereby the effect of stratification on the liquefaction progress can be explored.

As the rheological model for liquefied soil, storage equations for sub-liquefied seabed and the wave-induced shear stress finite solution used in this chapter are the same as those in Chapter 5, for the sake of brevity, they are not repeated here. The formulations of N-layer viscous fluid model and numerical scheme are presented first. Then, the predictions by the two-layer and N-layer models are compared for purpose of validation and for assessing the performance of the N-layer model. Finally, a parametric study is conducted to examine the effects of wave and soil characteristics on liquefaction progress.

6.2 System definition and formulation

Consider a progressive wave propagate over a level seabed. The liquefaction occurs at time t, its front advances down to a location $z = z_L$ as depicted in Fig. 6.1. The entire system consists of n viscous fluid layers including seawater layer with density ρ_1 ($0 \leq z \leq h$) and liquefied soil layers with density $\rho_i, i = 2, N$ ($z_L \leq z \leq 0$). Below the fluid layers, there is a poro-elasto-plastic sub-liquefied soil layer ($-D \leq z \leq z_L$). Before liquefaction, analytical solution for linear wave fluid pressure on water-seabed-interface is used to assess the excess residual pressure in seabed. Since the onset of liquefaction, the N-layer system is solved to obtain the water pressure exerted on surface of sub-liquefied soil prior to computing the built-up of residual pore pressure.

Dalrymple and Liu (1978) developed the two-layer fluid model for wave propagation over very viscous mud. The linear theory is applicable for wind wave

environment (Maa and Mehta, 1990) and overcome the limitation of Lamb's model which ignores viscosity of liquefied soil. The laminar Navier–Stokes equations for incompressible fluid, which has been linearized by neglecting the convective acceleration (Dalrymple and Liu, 1978) terms are written as

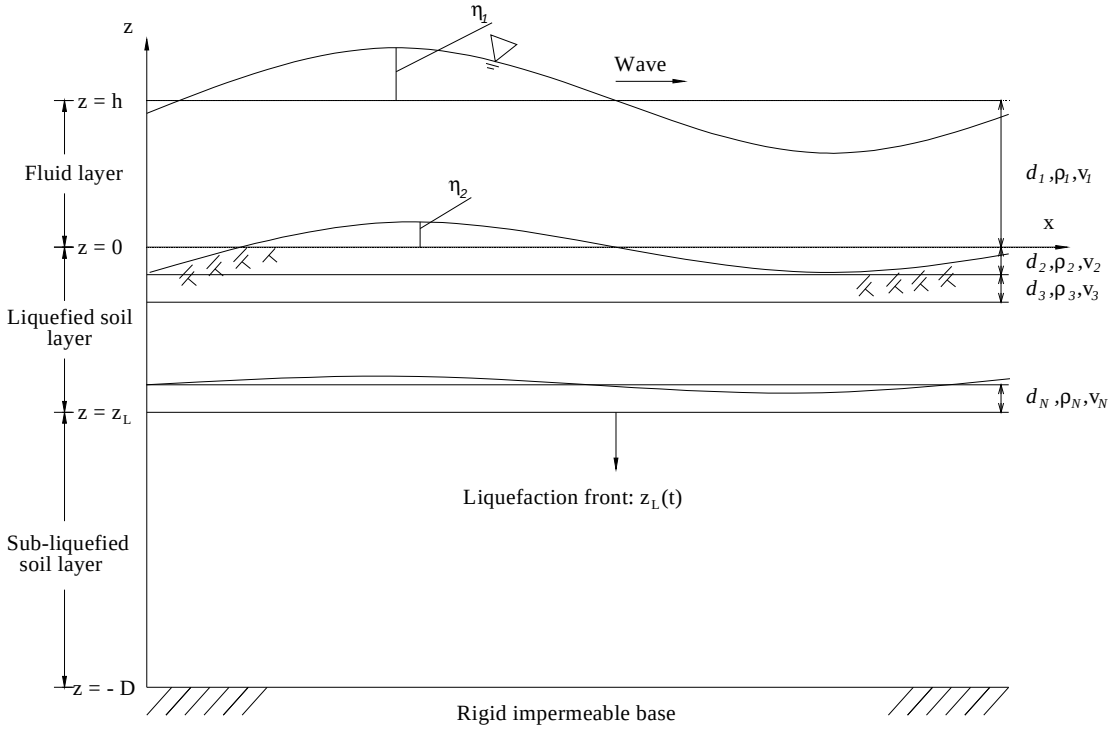

Fig. 6.1 Schematic definition of wave induced progressive seabed liquefied seabed

$$\frac{\partial \hat{u}_j}{\partial t} = -\frac{1}{\rho_j}\frac{\partial \hat{p}_j}{\partial x} + \nu_{e,j}\left(\frac{\partial^2 \hat{u}_j}{\partial x^2} + \frac{\partial^2 \hat{u}_j}{\partial z^2}\right) \tag{6.1}$$

$$\frac{\partial \hat{w}_j}{\partial t} = -\frac{1}{\rho_j}\frac{\partial \hat{p}_j}{\partial z} + \nu_{e,j}\left(\frac{\partial^2 \hat{w}_j}{\partial x^2} + \frac{\partial^2 \hat{w}_j}{\partial z^2}\right) \tag{6.2}$$

where $\hat{u}$, $\hat{w}$ are the horizontal and vertical velocities, respectively; the subscript j indicates the layer index; x and z are the horizontal and vertical coordinates, respectively; $\hat{p}$ is the dynamic pressure; ρ is the density of fluid; and $\nu_e = \mu_e/\rho$ is apparent kinematic viscosity; t represent the time.

The equations for mass conservation is expressed as

$$\frac{\partial \hat{u}_j}{\partial x} + \frac{\partial \hat{w}_j}{\partial z} = 0 \tag{6.3}$$

The separable, periodic solutions for $\hat{u}_j$, $\hat{w}_j$ and $\hat{p}_j$ are assumed as

$$\hat{u}_j(x, z; t) = u_j(z)\exp[i(\kappa x - \omega t)] \tag{6.4}$$

$$\hat{w}_j(x, z; t) = w_j(z)\exp[i(\kappa x - \omega t)] \tag{6.5}$$

$$\hat{p}_j(x, z; t) = p_j(z)\exp[i(\kappa x - \omega t)] \tag{6.6}$$

where ω is angular frequency of the wave system and κ is the unknown complex wave number after liquefaction

$$\kappa = \kappa_r + i\kappa_i \tag{6.7}$$

in which κ_r denotes the real part of the wave number which provides the wavelength ($L = 2\pi/\kappa_r$); κ_i is the imaginary part which represents the wave attenuation rate. Displacements of water surface and interfaces, η_j are represented by

$$\eta_j = a_j\exp[i(\kappa x - \omega t)] \tag{6.8}$$

where a_j is a complex unknown value to define the amplitude of the displacement of the jth layer. The water surface is expressed as η_1 while $\eta_j, j = 2, \cdots, n$ are unknown complex value representing mud sub-layer displacements based on their amplitude and phases. Substituting the real and imaginary parts of the wave number into Eq. (6.8), the expression of water surface and interfacial displacements can be obtained as

$$\eta_j = a_j exp(-\kappa_i x)\exp[i(\kappa_r x - \omega t)] \tag{6.9}$$

Substituting Eqs. (6.4), (6.5) and (6.6) into the continuity Eq. (6.3) results in

$$u_j = \frac{iw_j'}{\kappa} \tag{6.10}$$

in which the prime represents the differential with respect to z. Introduction of Eq. (6.10) into Eq. (6.1) yields an expression for p_j

$$p_j = \frac{\rho_j \nu_{e,j}}{\kappa^2}\left(w_j''' - w'\lambda_j^2\right) \tag{6.11}$$

where

$$\lambda_j^2 = \kappa^2 - i\sigma\nu_{e,j}^{-1} \tag{6.12}$$

Substituting p_j into the vertical momentum equation, Eq.(6.2), yields the fourth-order differential equation for w_j

$$w_j'''' - \left(\kappa^2 + \lambda_j^2\right)w_j'' + \kappa^2\lambda_j^2 w_j = 0 \tag{6.13}$$

The solutions can be obtained as

$$\begin{aligned} w_j(z) = A_j sinhk\left(\sum_{n=1}^{j} d_n + z\right) + B_j coshk\left(\sum_{n=1}^{j} d_n + z\right) \\ + C_j exp\left[\lambda_j\left(\sum_{n=1}^{j-1} d_n + z\right)\right] + D_j exp\left[-\lambda_j\left(\sum_{n=1}^{j} d_n + z\right)\right] \end{aligned} \tag{6.14}$$

where d_n is the thickness of n^{th} layer. The complex constants A_j, B_j, C_j, D_j and the unknown variables κ and a_j, are determined from the boundary conditions. $5N$ boundary conditions are required for a viscous fluid model of N layers. The unknown constants and variables are determined from the boundary conditions at the water surface, $(N-1)$ interfaces and the rigid bottom as follows:

(a) At the water surface ($z = \eta_1$)

The kinematic boundary condition, requiring the surface particles to follow the surface, and the imposition of zero normal and tangential stresses can be written as

$$\frac{\partial \eta_1}{\partial t} = \hat{w}_1 \tag{6.15}$$

$$\hat{p}_1 - 2\rho_1 \nu_{e,1} \frac{\partial \hat{w}_1}{\partial z} = 0 \tag{6.16}$$

$$\rho_1 \nu_{e,1} \left(\frac{\partial \hat{u}_1}{\partial z} + \frac{\partial \hat{w}_1}{\partial x} \right) = 0 \tag{6.17}$$

or after Taylor's expansion

$$A_1 sinh\kappa h + B_1 cosh\kappa h + C_1 + D_1 exp(-\lambda_1 h) = -i\omega a_1 \tag{6.18}$$

$$M_1 (A_1 cosh\kappa h + B_1 sinh\kappa h) - 2\rho_1 \nu_{e,1} \lambda_1 [C_1 - D_1 exp(-\lambda_1 h)] = \rho_1 g a_1 \tag{6.19}$$

$$2A_1 \kappa^2 sinh\kappa h + 2B_1 \kappa^2 cosh\kappa h + (\lambda_1^2 + \kappa^2)[C_1 + D_1 exp(-\lambda_1 h)] = 0 \tag{6.20}$$

where

$$M_1 = \frac{i\rho_1 \omega}{\kappa} - 2\rho_1 \nu_{e,1} \kappa \tag{6.21}$$

$$\lambda_1^2 = \kappa^2 - i\omega\nu_{e,1}^{-1} \tag{6.22}$$

And g is the gravitational acceleration.

(b) At the interfaces ($z_j = -\sum_{n=1}^{j} d_n$ where $j = 1, \cdots, N-1$)

$$\frac{\partial \eta_{j+1}}{\partial t} = \hat{w}_j \tag{6.23}$$

or

$$B_j + D_j + C_j\, exp\left(-\lambda_j d_j\right) = -i\omega a_{j+1} \tag{6.24}$$

The continuity of horizontal and vertical velocity components are

$$\hat{u}_j = \hat{u}_{j+1} \tag{6.25}$$

$$\hat{w}_j = \hat{w}_{j+1} \tag{6.26}$$

or

$$\begin{aligned} A_{j+1} sinh\kappa d_{j+1} + B_{j+1} cosh\kappa d_{j+1} + C_{j+1} + D_{j+1} exp\left(-\lambda_{j+1} d_{j+1}\right) \\ = B_j + D_j + C_j\, exp\left(-\lambda_j d_j\right) \end{aligned} \tag{6.27}$$

$$\begin{aligned} \kappa A_{j+1} cosh\kappa d_{j+1} + \kappa B_{j+1} \kappa^2 sinh\kappa d_{j+1} + C_{j+1}\lambda_{j+1} \\ - D_{j+1}\lambda_{j+1} exp\left(-\lambda_{j+1} d_{j+1}\right) \\ = \kappa A_j + C_j \lambda_j\, exp\left(-\lambda_j d_j\right) - \lambda_j D_j \end{aligned} \tag{6.28}$$

The normal and tangential stresses are also continuous across the interfaces. Considering the Taylor series expansion of $z_j = -\sum_{n=1}^{j} d_n$, they can be written as

$$\begin{aligned}\hat{p}_j - 2\rho_j \nu_{e,j} \frac{\partial \hat{w}_j}{\partial z} - \rho_j g \eta_{j+1} \\ = \hat{p}_{j+1} - 2\rho_{j+1} \nu_{e,j+1} \frac{\partial \hat{w}_{j+1}}{\partial z} - \rho_{j+1} g \eta_{j+1}\end{aligned} \tag{6.29}$$

$$\rho_j \nu_{e,j} \left(\frac{\partial \hat{u}_j}{\partial z} + \frac{\partial \hat{w}_j}{\partial x} \right) = \rho_{j+1} \nu_{e,j+1} \left(\frac{\partial \hat{u}_{j+1}}{\partial z} + \frac{\partial \hat{w}_{j+1}}{\partial x} \right) \tag{6.30}$$

or

$$\begin{aligned}M_j A_j - 2\rho_j \nu_{e,j} \lambda_j \left[C_j exp(-\lambda_j d_j) - D_j \right] \\ = M_{j+1} \left(A_{j+1} cosh\kappa d_{j+1} + B_{j+1} sinh\kappa d_{j+1} \right) \\ - 2\rho_{j+1} \nu_{e,j+1} \lambda_{j+1} \left[C_{j+1} - D_{j+1} exp\left(-\lambda_{j+1} d_{j+1}\right) \right] \\ - \left(\rho_{j+1} - \rho_j \right) g a_{j+1}\end{aligned} \tag{6.31}$$

$$\begin{aligned}\rho_j \nu_{e,j} \left\{ 2\kappa^2 B_j + \left(\lambda_j^2 + \kappa^2 \right) \left[C_j exp(-\lambda_j h) + D_j \right] \right\} \\ = \rho_{j+1} \nu_{e,j+1} \left\{ 2\kappa^2 \left(A_{j+1} sinh\kappa d_{j+1} + B_{j+1} cosh\kappa d_{j+1} \right) \right. \\ \left. + \left(\lambda_{j+1}^2 + \kappa^2 \right) \left[C_{j+1} + D_{j+1} exp\left(-\lambda_{j+1} d_{j+1}\right) \right] \right\}\end{aligned} \tag{6.32}$$

where

$$M_j = \frac{i\rho_j \omega}{\kappa} - 2\rho_j \nu_{e,j} \kappa \tag{6.33}$$

(c) At the bottom ($z_j = -\sum_{n=1}^{N} d_n$)

The velocities in both the horizontal and vertical directions should be zero at the fixed bottom, i.e.

$$\hat{u}_N = 0 \tag{6.34}$$

$$\hat{w}_N = 0 \tag{6.35}$$

or

$$\kappa A_N - \lambda_N D_N + \lambda_N C_N exp(-\lambda_N d_N) = 0 \tag{6.36}$$

$$B_N + D_N + C_N exp(-\lambda_N d_N) = 0 \tag{6.37}$$

The unknowns including coefficients A_j, B_j, C_j, D_j $(j = 1, 2, 3, \dots, N)$, the amplitude of interface wave a_j $(j = 2, 3, 4, \dots, N)$ and wave number κ can be solved from the above equations subjected to the appropriate boundary conditions by substitution and iteration methods.

The procedures to solve the automatically increasing number of fluid system are

1) Express variables at general layer j (j ≠ 1, N) A_{j+1}, B_{j+1}, C_{j+1}, D_{j+1} in terms of A_j, B_j, C_j, D_j, and a_{j+1} using 4 boundary equations at each layer interface; the remaining one equation is used to describe the expression between a_{j+1} and a_j.

2) When $j = 1$, A_j, B_j, C_j, D_j can be determined by three surface boundary equations and one of 1-2 interface boundary conditions; as a result, they can be expressed using a_2. 3) Eventually, there are two unknowns, wave number κ and a_2 remain because

a_j ($j = 3, 4, 5, \ldots, N$) can be expressed in terms of a_2. Two boundary condition equations are employed to solve κ and a_2. Since the final forms are implicitly non-linear, two layers of nested loop nonlinear root finding subroutine (Newton method is adopted in this study) are need.

The details of the derivation and explanation refer to Appendix F in this thesis. After successive solving of the upper fluid system, the amplitude of wave pressure at the bottom of fluid region can be derived from Eq. (6.11) and used to solve the residual pore pressure build-up.

6.3 Numerical scheme and computational procedure

Discretization of storage equation for sub-liquefied soil is identical to the two-layer model. The distinct difference is the solving the N-layer fluid system. The seawater layer has a constant depth and the thickness of sub-layer of liquefied soil is set to be 1/200 of the total seabed depth. The detailed procedure of the analysis is as follows:

(1) Start analysis from $\kappa = \kappa_0$ $z_L = 0$, $\xi = 0$; calculate initial wave number by water depth and wave period.

(2) Before liquefaction, the wave pressure is calculated by the common formula for a progressive wave: $P_0 = \gamma_f m_0 / cosh(k_0 d)$.

(3) Solve Eq. (5.55) to get the residual pressure at each point for $\xi = \xi + \Delta\xi$.

(4) Repeat steps (2) and (3) until P_{r2} increases to the value $\gamma' \Delta z$.

(5) Update the liquefaction front location, number of liquefied soil layers and vertical effective stress.

(6) In the following steps, the multi-layer wave model is used to calculate κ and the amplitude of fluid pressure over sub-liquefied soil p_L. In the first run after onset of

liquefaction, a guess value of a uniform liquefied soil viscosity is provided. In the sequent runs, the viscosity of the last solution is used as trial value. Then, the N-layer fluid system is solved to get shear strain rate of liquefied soil layer. Use the rheological equation to achieve a new viscosity. Check if the guessed viscosity is sufficiently close to this new value. Except from the first run, the viscosity for liquefied sub-layers actually is an array. If relative difference between each element of the successive velocity arrays is lower than a certain level (in this study, 1/100), the convergent velocity array is assumed to be acquired. Then continue the next step; otherwise, repeat this trial-and-error until a convergent value is reached.

(7) Input the convergent viscosity value into the multi-layer system to get the wave pressure at sub-liquefied seabed surface, $z = 0$;

(8) With the wave pressure exerted on seabed surface, the analytical solution of wave-induced shear stress and shear stress ratio are calculated to determine$\partial v^p / \partial \xi$.

(9) Solve Eq. (5.55) to get the residual pore pressure.

(10) Repeat steps (5)–(9) until the end of the analysis.

The solving procedure of the entire system and for determining fluid motion with the multi-layer fluid system are summarised in Fig. 6.2 and Fig. 6.3, respectively.

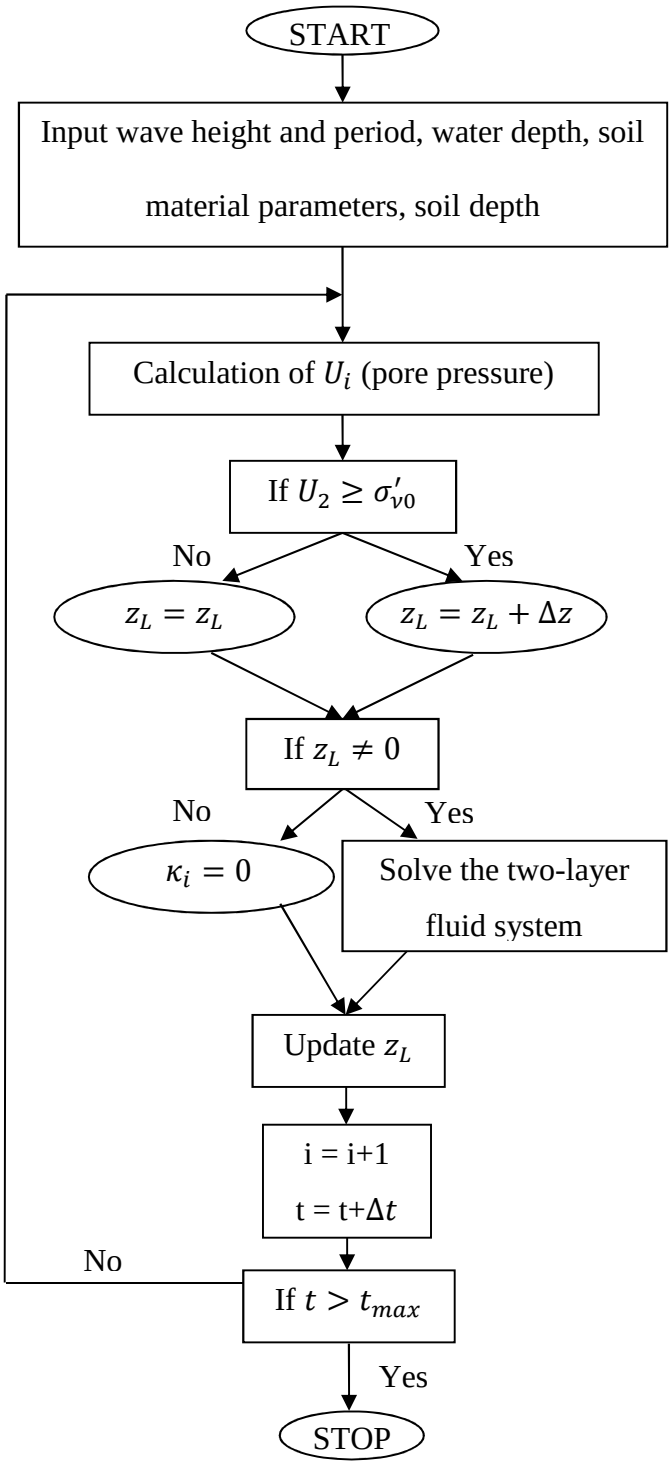

Fig. 6.2 Flowchart for the solution procedure of the entire system

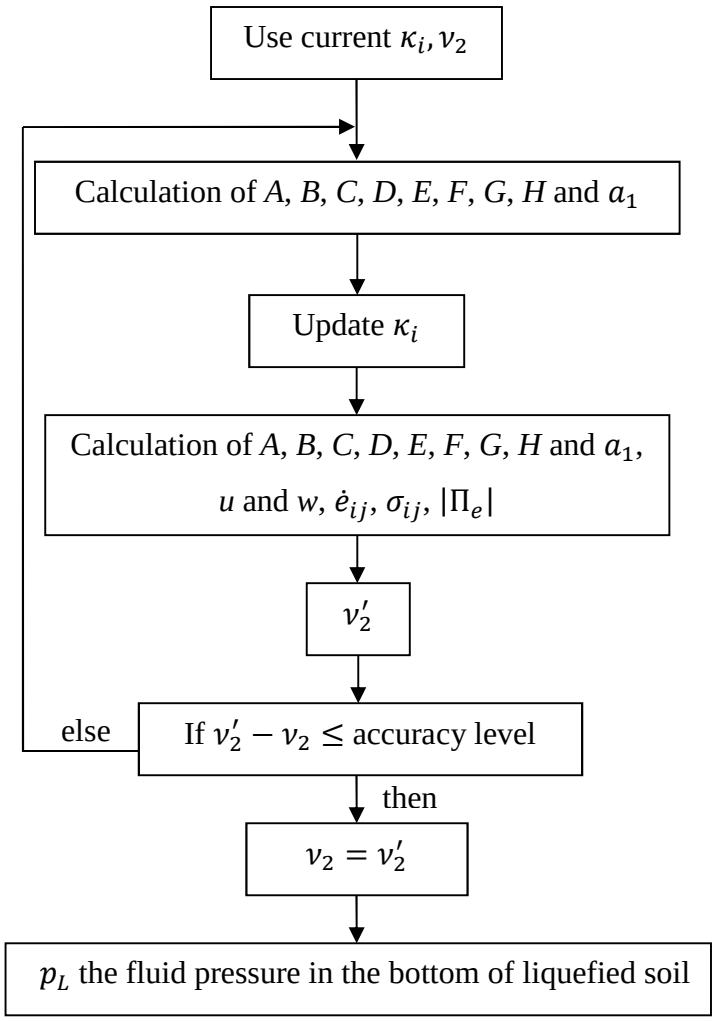

Fig. 6.3 Flowchart for the soluting procedure of the two-layer fluid system

6.4 Model validation

Before examination and parametric analysis, a comparison is performed to verify the performance of multi-layer model. Model A is reproduced by reducing the N-layer viscid model (Model B) to a constant viscosity for liquefied soil. As shown in Fig. 6.4, liquefaction front evolution from two models is completely identical as expected, thus validating the multi-layer modelling. The parameters used in the case for comparison are listed in Table 6.1.

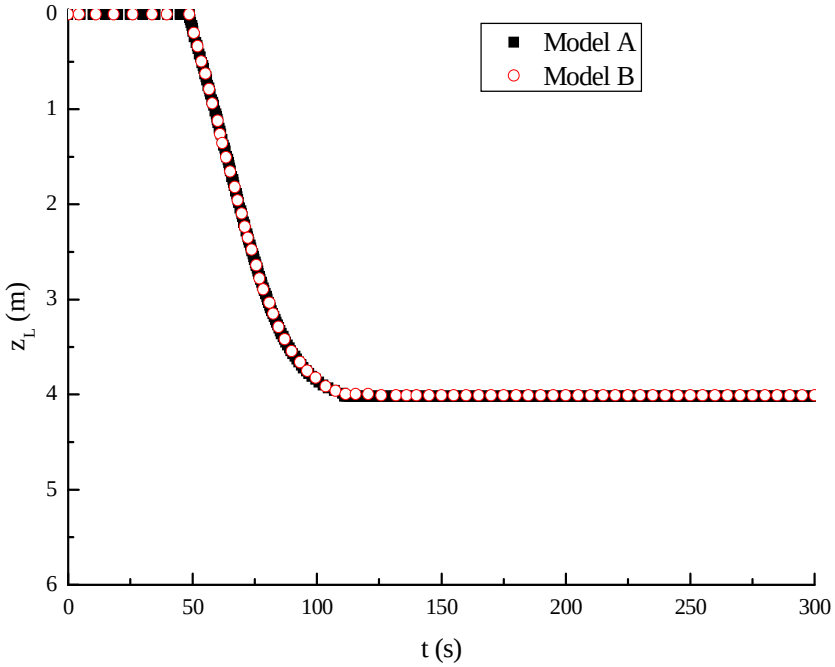

Fig. 6.4 Reproduction of Liu et al. (2009)'s results for evolution of liquefaction front

Table 6.1 Wave conditions and soil parameters

Wave conditions	
Fluid depth, *h*: m	20
Wave period, *T*: s	10
Initial wave length, *L*: m	121.2
Wave height, *H*: m	6.5
$\nu_1 : m^2 s^{-1}$	1×10^{-6}
$\nu_2 : m^2 s^{-1}$	10 (for Model A)
Initial guess viscosity of liquefied soil, $\nu_2 : m^2 s^{-1}$	10 (for Model B)
Soil bed conditions	
Soil depth, *D*: m	6.0
Permeability coefficient, $k_z : m s^{-1}$	1.5×10^{-4}
Density of liquefied soil, $\rho_s : kg m^{-3}$	1800
$M_D : kPa$	3.12×10^4
Soil shear modulus, *G, MPa*	31.2
Poisson's ratio	0.33

R	1.8×10^{-5}
α	55
β	0.04

6.5 Results and discussion

A series of numerical simulations are performed to investigate the factors influencing the liquefaction progress. The difference between the multi-layer and two-layer modelling is examined to highlight the advantage of the former. The wave and soil parameters which are used in the simulations are summarized in Table 6.1 unless stated otherwise.

6.5.1 **Effect of varying liquefied soil density**

The varying density of liquefied soil with depth has long been recognised (Sumer et. al, 1999) even though an appropriate mathematical model to describe the inherent mechanism was not available. In this section, a linearly increasing liquefied soil density is assumed to investigate its influence on liquefaction. This is realised by specifing a linearly decreasing water content (from 60% at upper layer to 20% at seabed bottom if the seabed can be completely liquefied). The corresponding values of liquefied soil density are 1648.8 and 2103 kg/m^3, respectively. Sumer (2006) measured the liquefied soil density in a small scale laboratory test, which is 1850 at surface and 2000 at the impermeable bottom. The range used here is a little larger than that for the purpose of parametric study.

Fig. 6.5 shows that the difference in the final liquefaction depths predicted by varying water content model and constant water content model is no more than 12%. For the constant water content model, higher water content leads to swallower liquefaction. However, the difference of interface wave amplitude made by varying liquefied soil sub-layer density is significant.

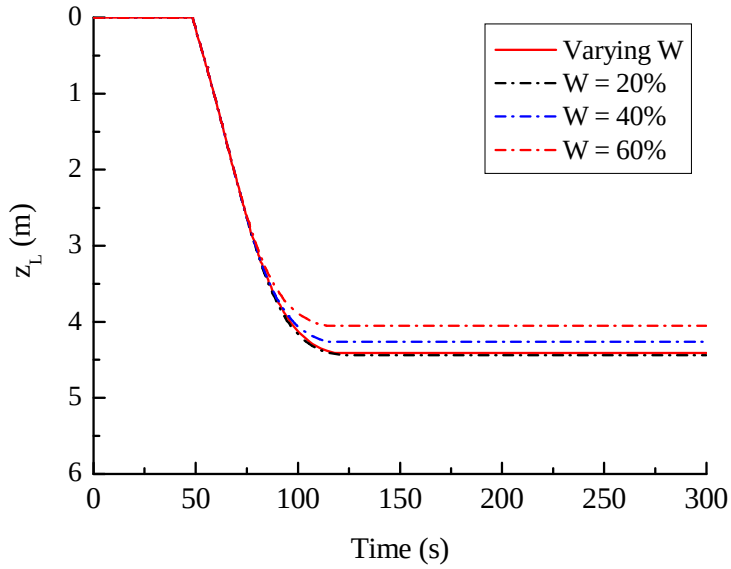

Fig. 6.5 Effect of varying water content on liquefaction

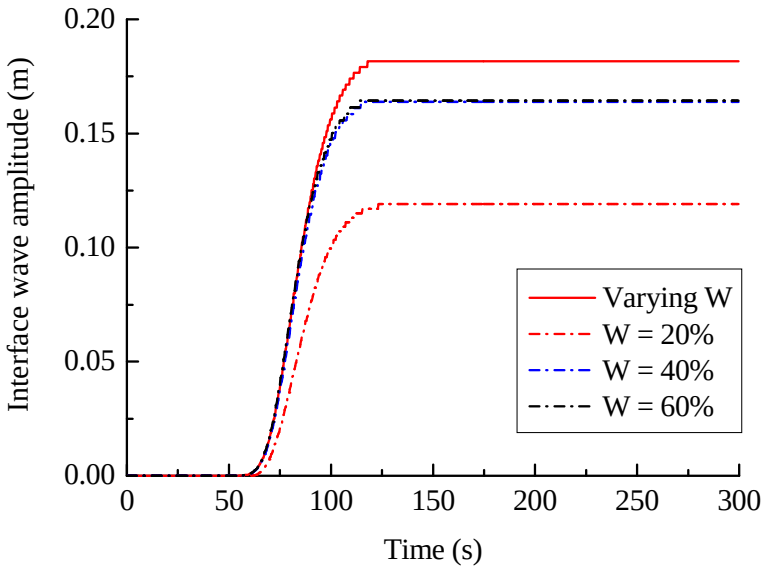

Fig. 6.6 Effect of varying water content on the interface (between water and liquefied soil) wave amplitude

Fig. 6.6 shows that the amplitude predicted by varying density model is much larger. Despise the closeness of final liquefaction depth between varying density model and constant $w = 20\%$, there is a difference in amplitudes of interface wave between two models.

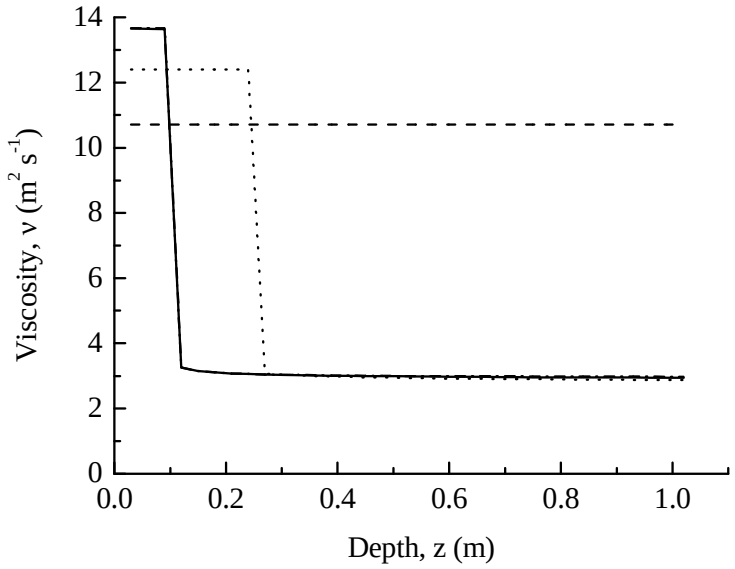

(a) Number of layers, N = 35

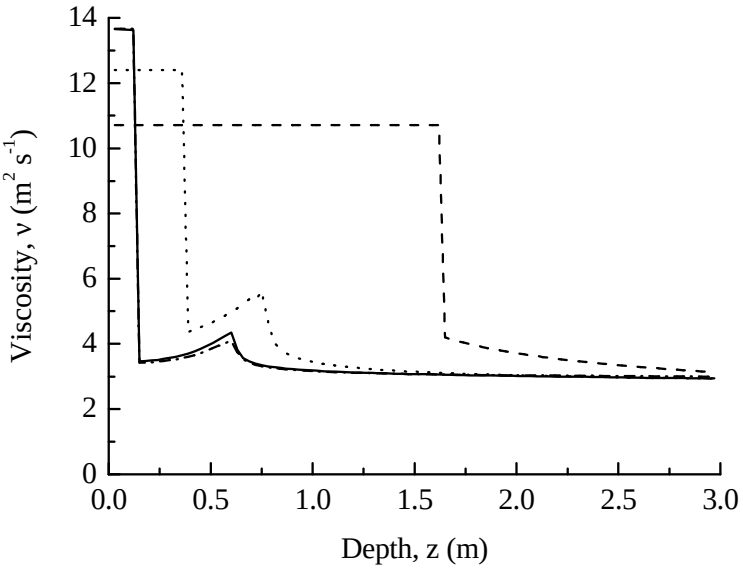

(b) Number of layers, N = 100

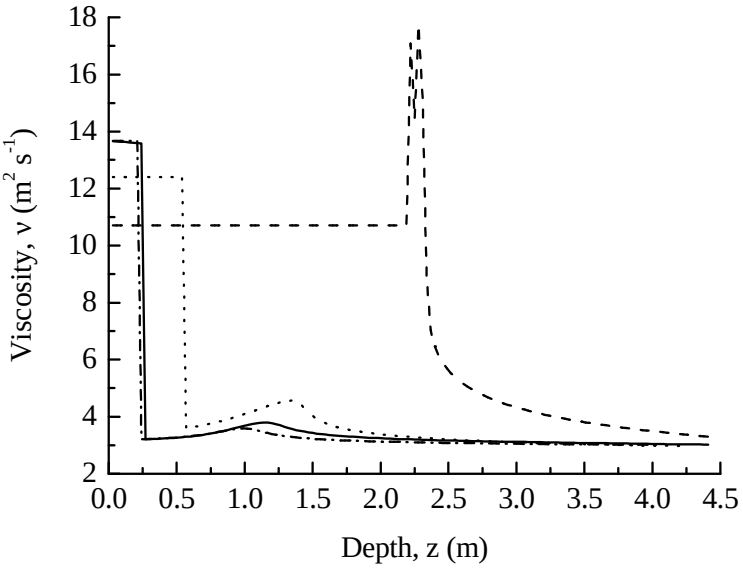

(c) Final liquefaction

Fig. 6.7 Effect of varying water content on distribution of liquefied soil viscosity: solid line for varying water content, dash line for $W = 20\%$, dot line for $W = 40\%$, and dash dot line for $W = 60\%$.

Fig. 6.7 illustrates the distribution of viscosity of liquefied soil during liquefaction. Viscosity in varying density model is much closer to constant water content $W = 60\%$ than the others. When water content is lower, the liquefied soil tends to stay in visco-elastic phase especially in the upper layer. As for the critical viscosity value between visco-elastic and visco-plastic phase, higher water content results in a higher critical transit viscosity. In Fig. 6.7(c), the fluctuation of viscosity is caused by the difficulty in numerical solution. The multi-layer model with linearly changing water content is found to achieve a convergent viscosity of liquefied soil easier than two-layer model.

There is another phenomenon concerning liquefied soil density. For a higher density, the two-layer viscid model with a constant liquefied soil density but temporal changing

strain rate-dependent viscosity cannot produce liquefaction or the resulting liquefaction depth is shallower than the N-layer viscid model. Three cases are considered here: Case 1: water content ratio $W = 30\%$, constant liquefied soil is 1939.2 kg/m^3; Case 2: water content ratio $W = 40\%$, constant liquefied soil is 1817.3 kg/m^3 and Case 3: water content ratio $W = 50\%$, constant liquefied soil is 1723.4 kg/m^3. Results are shown in Fig. 6.8. Compared with results in Chapter 4, there is much more difference made by the water content ratio for the two-layer model because the density is related to water content using Eq. (6.38). When water content reduces, the liquefaction drastically decreases. Actually, there is no liquefaction predicted by two-layer model for case 1. For the N-layer model with constant water content through the depth, the trend of water content influence is opposite.

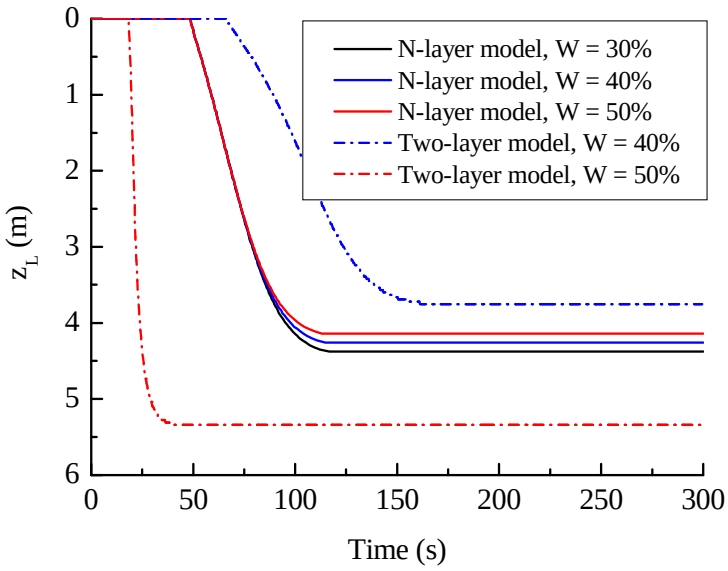

Fig. 6.8 Effect of liquefied soil density (caused by water content difference) on liquefaction

The increasing water content tends to resist a bit the liquefaction despite that the associated density of liquefied soil is relatively smaller. Also, the difference between two-layer model and N-layer model depends on the water content ratio. For Case 1 and Case 3, the difference is more significant than for Case 2. Therefore, stratification of viscosity along the liquefied soil layer does influence the liquefaction and fluid motion (e.g., the interface wave amplitude).

6.5.2 **Effect of varying viscosity**

A comparison between the two-layer and N-layer model is carried out in this section. The density of liquefied soil ρ_{lid} is related to the water content ratio by:

$$\rho_{lid} = \rho_g(100 + W)\frac{\rho_f}{100\rho_f + W\rho_g} \tag{6.38}$$

where the density of soil grain, $\rho_g = 2700\ kgm^{-3}$; ρ_f is the density of fluid, $\rho_f = 1000\ kgm^{-3}$. The initial density of liquefied soil is set to $1800\ kgm^{-3}$, so the water content ratio in the rheological model is 42%.

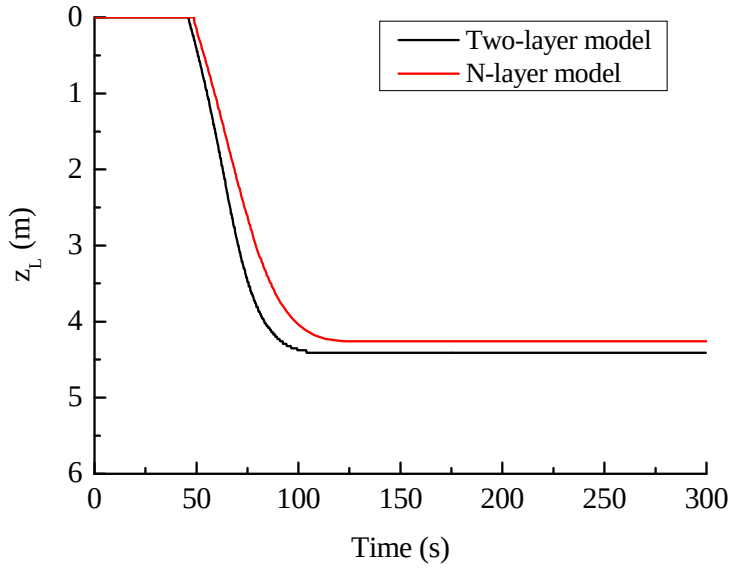

Fig. 6.9 Comparison of time histories of liquefaction front

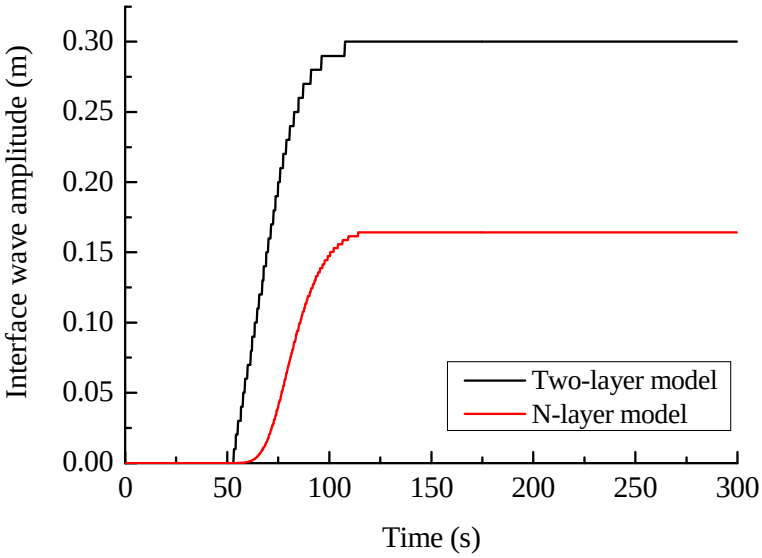

Fig. 6.10 Comparison of interface (between water and liquefied soil) wave amplitude

As shown in Fig. 6.9, the maximum liquefaction depth for the N-layer viscous model is 4.26m, around 3.5% lower than that obtained by the corresponding two-layer

model (4.41m). In this case, the difference in final liquefaction depth is slightly smaller than the difference in interface wave amplitude (approximately 50%, shown in Fig. 6.10). Moreover, the liquefaction starts a little later in the N-layer model.

The multi-layer modelling approach provides the ability to consider different viscosity for each sub-layer as well as varying density of liquefied soil (see the next section). Although the viscosity of liquefied soil layer υ_2 in two-layer model varies with the liquefaction front advances downward as shown in Fig. 6.11, it is still a constant at an instantaneous time and a certain liquefaction depth. In the N-layer model, the viscosity of liquefied soil layer υ_2 varies along with the depth of seabed, which means that both the temporal and spatial changes of viscosity are considered.

Fig. 6.12 illustrates the distribution of liquefied soil viscosity, which varies with the depth of liquefied layer for three different liquefaction depths. The jump of viscosity along depth confirms the presumption of liquefied soil phase transition from visco-elastic to visco-plastic phase. It indicates that the shear strain rate is smaller in the upper part than in the lower. The critical viscosity values at which the phase transition occurs for two-layer model and N-layer model are not same due to the different shear stresses from two models. By comparing Figure 6.11 and Figure 6.12, we can see that the viscosity produced by multi-layer model is not completely the same as that by two-layer model. And the possible minimum viscosity in the two-layer model is lower than that in the multi-layer model.

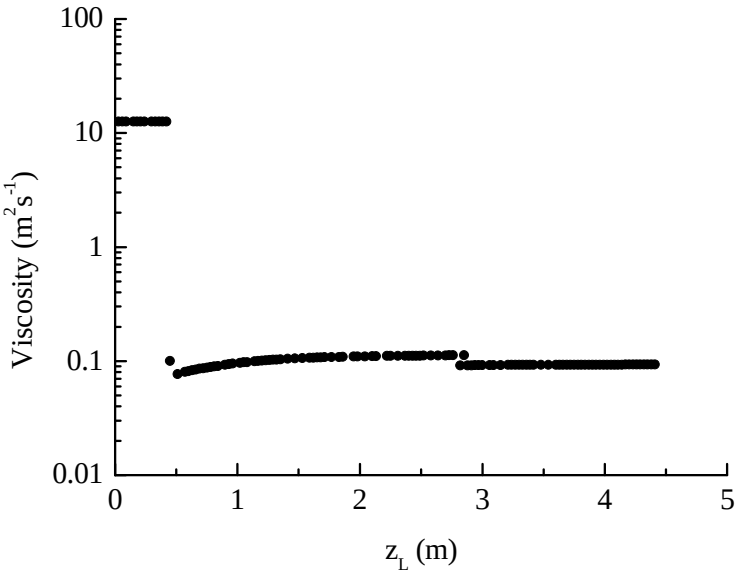

Fig. 6.11 Evolution of liquefied soil viscosity in two-layer model

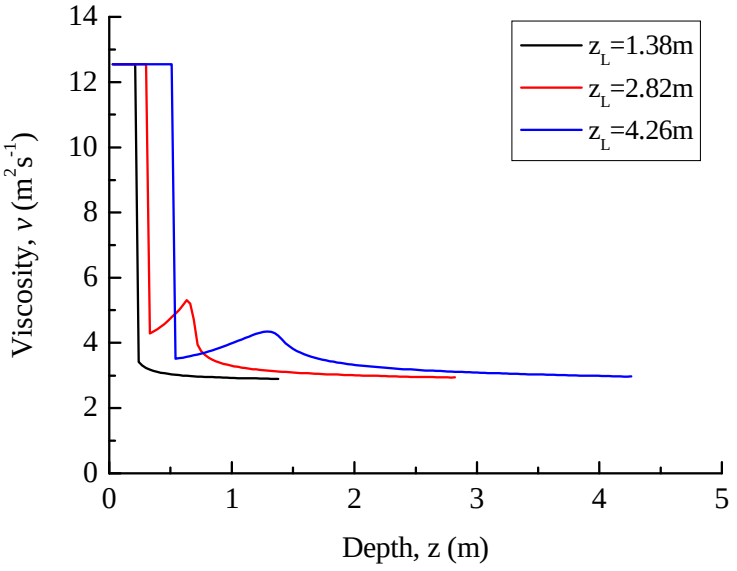

Fig. 6.12 Distribution of liquefied soil viscosity in N-layer model

6.5.3 **Effect of wave and soil characteristics**

As shown in Fig. 6.13, the liquefaction process for shallower water depth begins sooner and the liquefaction front reaches deeper. It also indicates that this relationship between water depth and liquefaction process is not linear. When the water depth is near a certain critical depth, the change is much dramatic, then, the influence gradually weakens. When the water depth increases, the corresponding viscosity in visco-plastic state also see a slight increase (Fig. 6.14). However, there is no discernible difference in the viscosity of visco-elastic state because at this stage the viscosity is independent of the fluid motion.

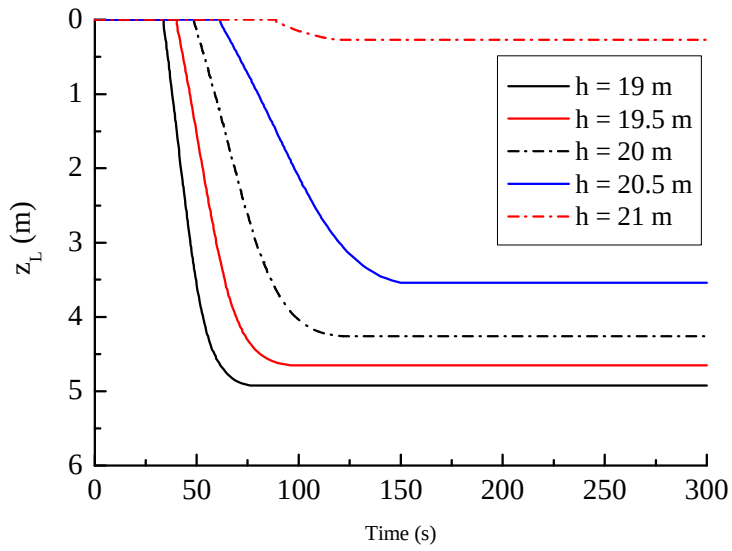

Fig. 6.13 Influence of water depth on liquefaction processes

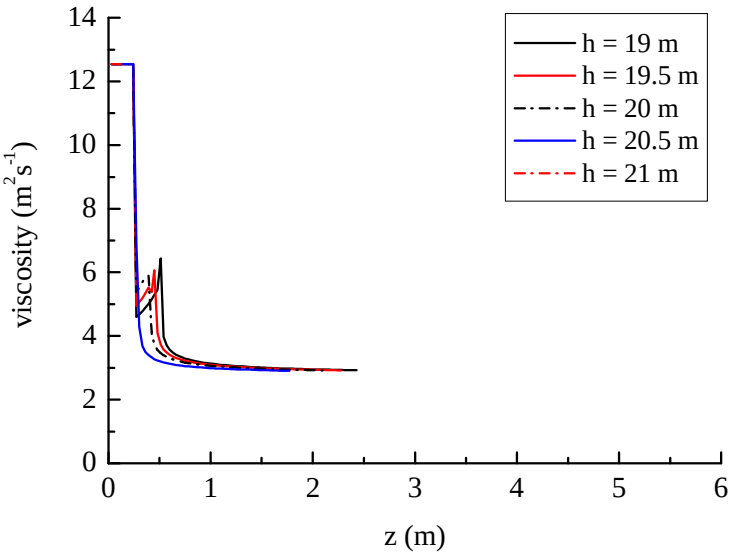

(a) At the time instant for a half the final liquefaction depth

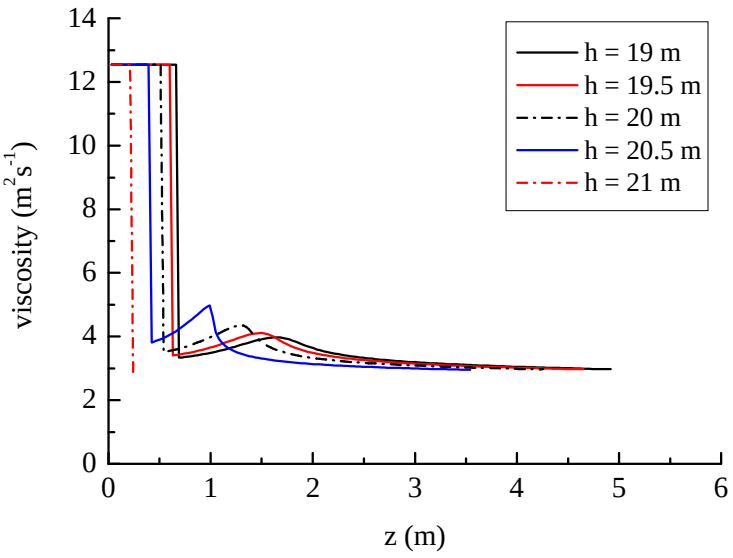

(b) At the time instant for the final liquefaction depth

Fig. 6.14 Influence of water depth on viscosity of liquefied soil

Fig. 6.15 shows that a shorter wave period results in a deeper liquefaction. It is because the wave period affects wave pressure (together with water depth) acted on sub-

liquefied seabed, and also the liquefied soil viscosity though it is not significant as shown in

Fig. 6.16). For porous sub-liquefied soil, wave period affects the partial drainage factor, which controls the dissipation rate of residual pressure (Liu et al., 2009). This is consistent with findings in the two-layer viscid model used in both Chapter 4 and Liu *et al.* (2009).

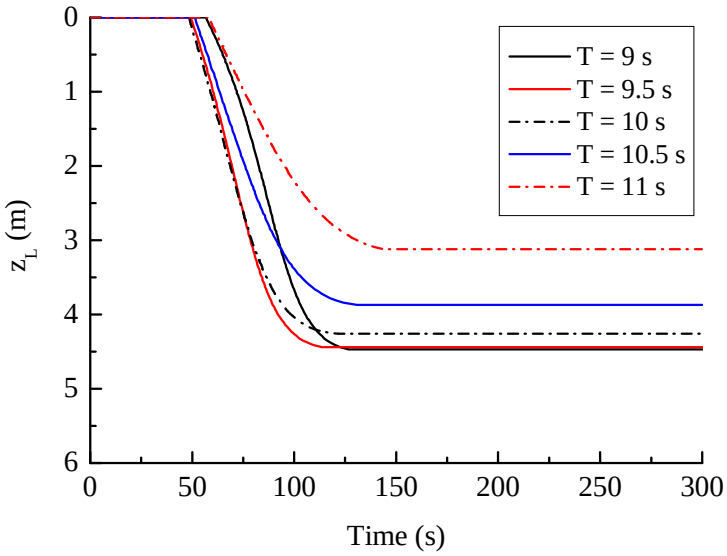

Fig. 6.15 Influence of wave period on liquefaction processes

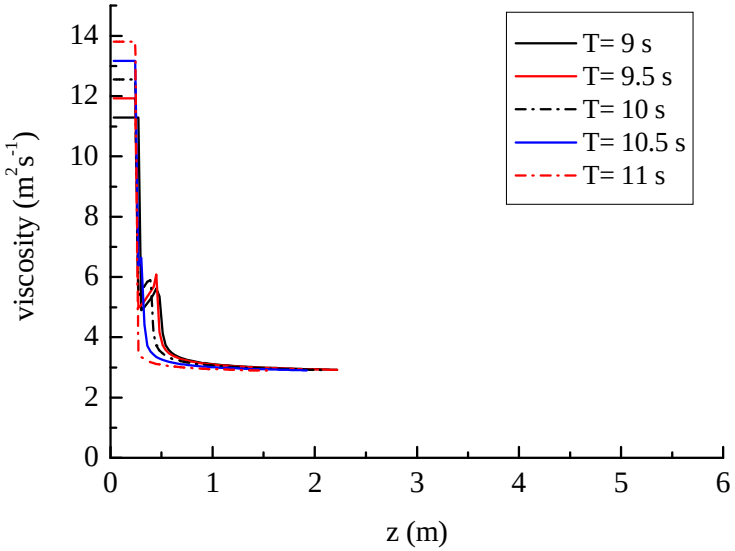

(a) At the time instant for a half the final liquefaction depth

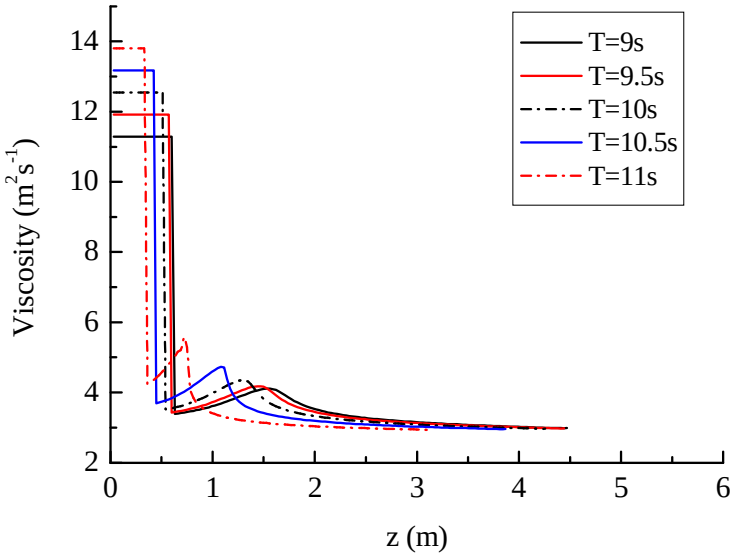

(b) At the time instant for the final liquefaction depth

Fig. 6.16 Influence of wave period on viscosity of the liquefied soil

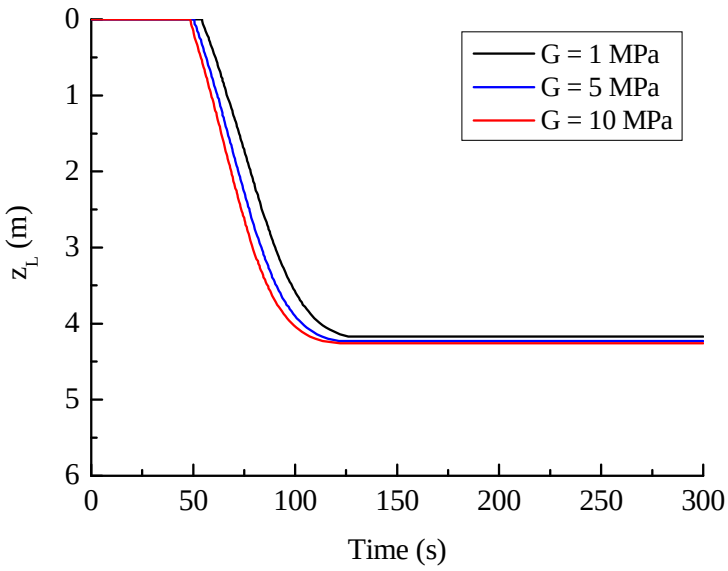

Fig. 6.17 Influence of shear modulus, G on liquefaction

Fig. 6.17 and Fig. 6.18 illustrate the influence of different soil shear modulus, Gon the liquefaction, wave-induced shear stress in poro-elasto seabed. For the considered cases, the shear stresses predicted are not sensitive to soil shear modulus, and consequently there is no significant difference by various G, though the final liquefaction depth in softer seabed is slightly shallower. Based on the analytical solution for finite seabed proposed by Jeng and Hsu (1996), the wave-induced vertical effective stress is shown in Fig. 6.19. The effective stress due to overburden, which acts as a resistance to liquefaction is also depicted for comparison. According to Yamamoto *et al.* (1978), momentary liquefaction occurs when seepage force lifts soil column above and soil particles cease to be in contact. Mathematically, that is the case when wave-induced effective stress surpasses overburden. Fig. 6.19 shows that the overburden effective stress far larger than the wave-induced effective stress in the considered cases, which

indicates that there is no momentary liquefaction happen and the presumption of residual liquefaction mechanism is appropriate.

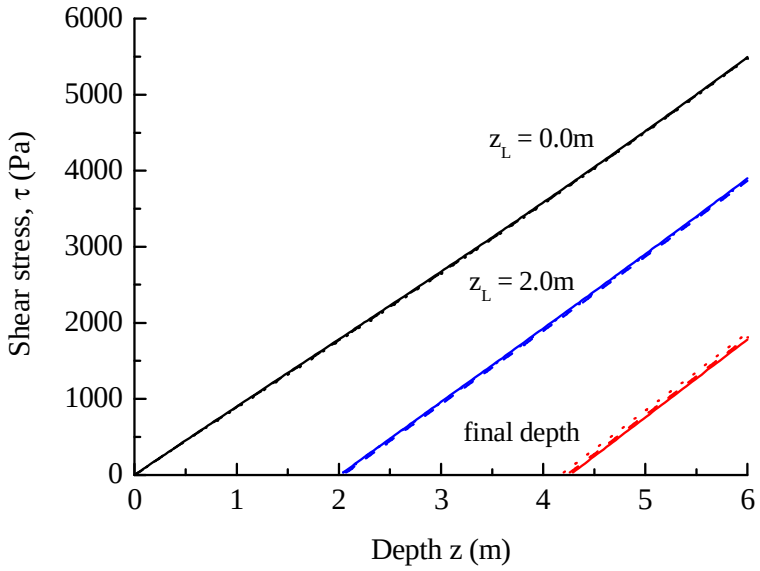

Fig. 6.18 Influence of shear modulus, G on wave-induced shear stress: solid line is for case with $G = 1$ MPa; dash line for case with $G = 5$ MPa and dot line for for case with $G = 10$ MPa.

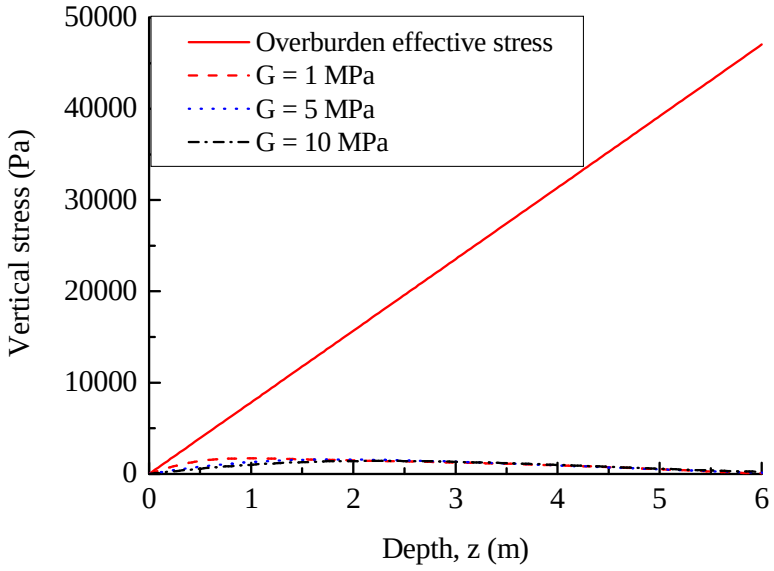

(a) Before liquefaction, $z = 0$ m

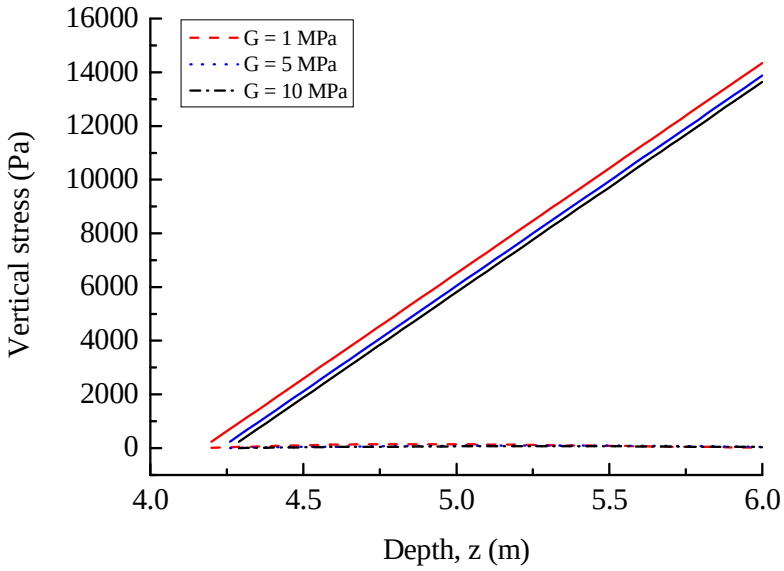

(b) Final liquefaction depth

Fig. 6.19 Influence of shear modulus, G on wave-induced vertical effective stress: solid line is effective stress due to overburden and other curves represent wave-induced effective stress

As shown in Fig. 6.20, the larger hydraulic conductivity results in shallower liquefaction depth. With the increase of permeability to a higher range (beyond 1.75×10^{-4} m/s in this case), the liquefaction depth decreases markedly. This is caused by a greater rate of residual pore pressure dissipation for more permeable soil.

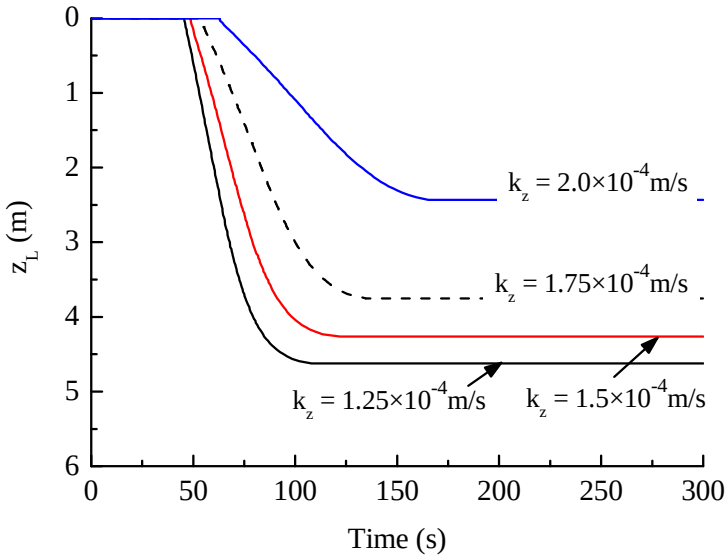

Fig. 6.20 Influence of soil permeability on liquefaction process

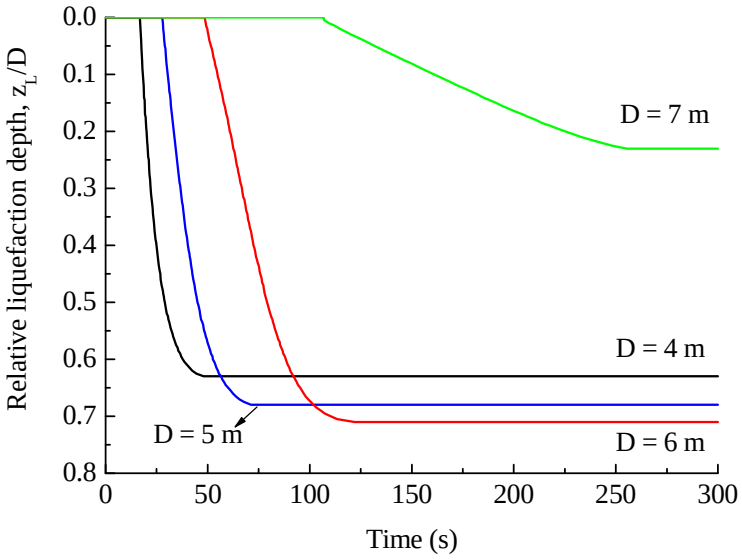

Fig. 6.21 Influence of seabed thickness on liquefaction process

Furthermore, the thickness of seabed affects the liquefaction strongly. In Fig. 6.21, the liquefaction depth increases gradually when seabed becomes thicker until the thickness reaches 6 m; and then, it reverses to decrease sharply with increasing

thickness of seabed. It appears that there exists a critical seabed thickness (6m in this case), at which the final liquefaction depth reach the maximum value if other conditions for wave and soil were held the same. Physically, the generation of excess residual pore pressure mainly depends on soil volume change due to cyclic loading and the drainage condition. When the seabed is thinner than the critical thickness, increasing the thickness means a longer drainage distance (the seabed bottom is assumed to be impermeable to water), which helps to build up residual pore pressure. However, with the seabed becoming thicker and thicker, the shear stress induced by the wave cyclic loading starts to decrease and dominate the liquefaction progress. Fig. 6.21 indicates that a thinner seabed and the corresponding greater soil shear stress results in an earlier commencement of liquefaction. And the time required to reach final liquefaction depth becomes shorter. These two phenomenon is particularly obvious for the case with $D = 7$m.

6.5.4 **Effect of soil poro-plastic parameters α, β, R and M_D**

Error! Reference source not found. to 6.25 illustrate that the liquefaction is very sensitive to parameters α, β. Therefore great care should be taken in their calibration. Unfortunately, Sassa (2001) did not give the identification procedure for these parameters. They seem to have been determined by matching the simulations results with the centrifuge tests. Thus, applying the model parameters to other cases is questionable. Constrained modulus at seabed bottom, M_D and another poro-plastic parameter, R also influence the liquefaction, though not as much as α, β.

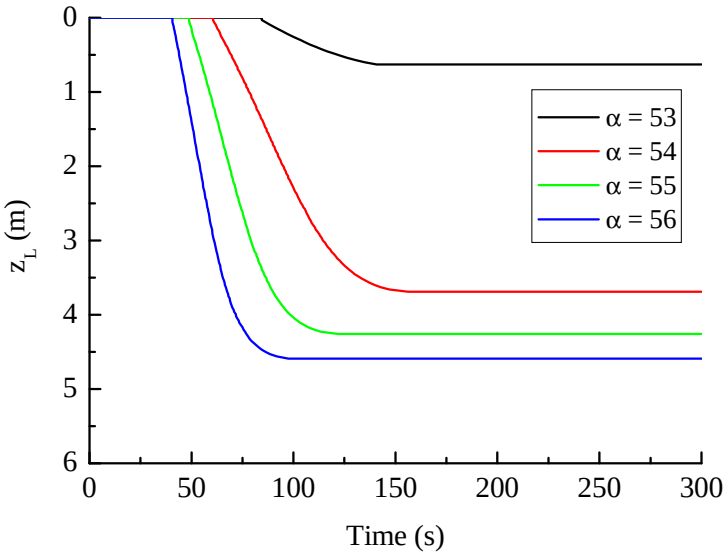

Fig. 6.22 Influence of α on liquefaction process

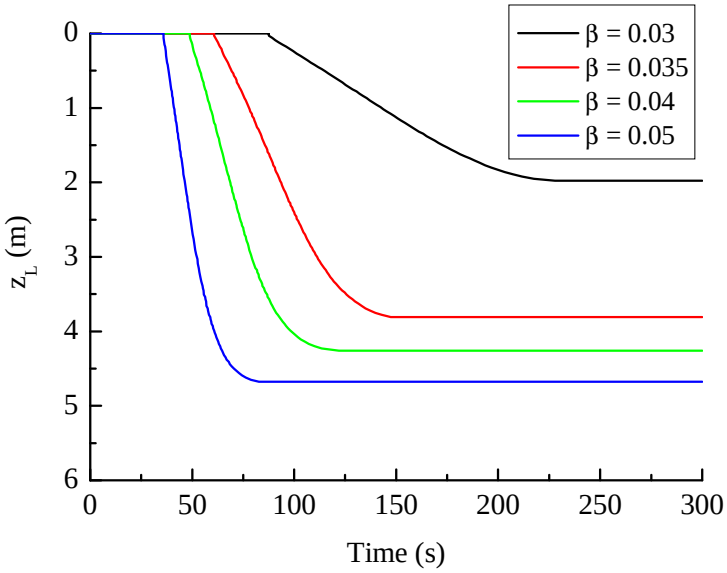

Fig. 6.23 Influence of β on liquefaction process

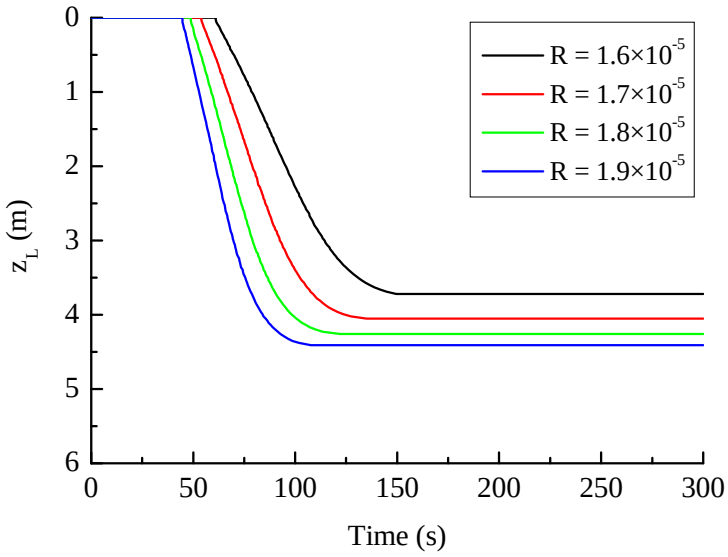

Fig. 6.24 Influence of R on liquefaction process

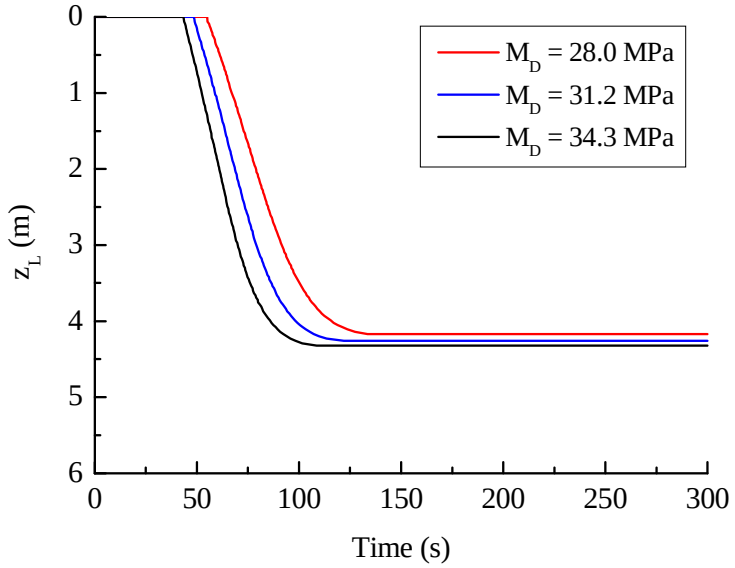

Fig. 6.25 Influence of constrained modulus, M_D on liquefaction

6.6 Summary

In this chapter, a multi-layer viscid fluid system model for simulation of water and liquefied soil is constructed. The number of layers can automatically increase with the advance of liquefaction front. Density of liquefied soil is related to the mass water content. To investigate the effect of varying liquefied soil density on liquefaction, a linearly decreasing water content is assumed. From the series of numerical experiments, the following summary can be drawn:

1) When the water content ratio for liquefied soil is assumed to be constant, there can be significant differences in the predicted liquefaction depth and wave amplitude using the multi-layer and two-layer model. Whether they increase or decrease depends on the specific water content. Moreover, the visco-plastic phase viscosity predicted by multi-layer model is much smaller than that by two-layer model.

2) For the multi-layer model, a continuously increasing liquefied soil density can ease the numerical difficulty in getting the viscosity to converge. This trend of density of liquefied soil has been confirmed experimentally (Sumer *et al.*, 2006). The results of liquefaction depth and interface wave amplitude differ from that predicted by constant water content model. Interface wave amplitude is an important indicator of the liquefied soil motion and controls the mass transport speed. Therefore, it is essential to accommodate the stratification of liquefied soil viscosity and density. In that case, the multi-layer viscid fluid model established here would be very useful.

3) Under the condition of the same wave height, shorter wave period in shallower water can liquefy the underlying seabed more easily. When the water depth increases, the corresponding viscosity in visco-plastic state also sees a slight increase.

4) Softer soil with lower permeability can lead to deeper liquefaction. Based on the simulation results, there seems to be a critical seabed thickness, at which the effect of seabed thickness on liquefaction reverses. Below the critical thickness, the liquefaction depth is smaller due to the relatively short drainage distance in thinner seabed. Beyond the critical thickness, increasing seabed thickness dampens the wave energy and consequently prevents the liquefaction. However, further investigations are needed to clarify which factors influence the critical thickness of seabed and to provide a formula to estimate the critical thickness.

5) Seabed liquefaction is very sensitive to the soil plastic model parameters, especially α, β, which are involved in residual pore pressure build-up equation. Therefore, a reliable identification procedure for them is extremely important.

Chapter 7 Conclusions and Recommendations

7.1 Conclusions

The primary aim of this thesis is to investigate the seabed residual liquefaction progress under progressive wave numerically. To this end, four key investigations have been done. Firstly, a review of literature on wave-induced liquefaction was carried out. Hereafter, a two-layer in-viscid fluid system approach was taken as a starting point to describe the wave-liquefied soil. Secondly, ensemble modelling method was used to examine the seabed liquefaction under random linear wave loading. Following it, the two-layer in-viscid fluid system was developed into viscid fluid system with strain rate dependent viscosity for liquefied soil considered. Finally, this model was further extended to multi-layer system to address the stratification of different properties for each sub-layer of liquefied soil.

7.1.1 Ensemble modelling for the assessment of random wave-induced liquefaction risks

Since liquefaction usually takes place over a short time scale (around $10T$) characterised by a single storm, the simulation is limited to large narrow-band waves for sake of simplicity. Based on the linear wave theory the wave height was numerically generated according to the Rayleigh distribution. All soil material and other parameters in the model were treated as deterministic constants to highlight the effect of randomness of wave height. Two types of ensemble modelling were performed using wave heights randomly sampled from a prescribed Rayleigh distribution, one involving

multiple runs of the liquefaction model using regular wave series and the other with random wave series.

For the first type, up to 275 runs were performed and the histograms of the maximum liquefaction depth and the time to reach the maximum liquefaction depth are produced. The root mean square liquefaction depths determined from the histogram was greater than the liquefaction depth calculated using a single representative wave height H_{rms}. The root mean square time to the maximum liquefaction depth determined by the histogram excluding no liquefaction runs was smaller but comparable to the corresponding value obtained with a single representative wave height H_{rms}.

As for the second type, the histogram of the liquefaction depth and the time to reach the maximum liquefaction depth were also generated. The random wave-induced liquefaction was much deeper than that corresponding to the equivalent regular wave case. Due to the presence of large number of small waves in the time series, the time to the maximum liquefaction is expected to be longer for random waves. The maximum wave height in each wave time series was plotted against the corresponding final liquefaction depth. The strong linear correlation exists between them demonstrated that the extent of liquefaction was controlled by the size and number of largest wave heights in the wave time series. To examine whether the order of appearance of waves of different height in a random wave series will affect the liquefaction time, the relationship between the time when the liquefaction depth reaches the maximum and the time when the maximum wave height occurs was depicted. It implied that the time for the maximum liquefaction depth to be reached was strongly associated with the time of occurrence of the maximum wave height except perhaps when the maximum wave height in the sample is very small. The overall relationship seems to indicate that the

timing of largest waves in the wave time series controls the time for the maximum liquefaction depth to be reached, at least for large liquefaction depth.

In order to further understand the statistical properties of the predicted liquefaction depth, three theoretical distributions including the two parameter Weibull distribution, Rayleigh distribution and Normal distribution were fitted to the numerical results. Regarding the first type running, none of the three theoretical distributions seems to fit the entire range of the final liquefaction depth, which reflected that the system was nonlinear. However, the fit in the larger value range seemed to be better for all three distributions, indicating the usefulness of these theoretical distributions for extreme analysis. For the second type, a much narrower spread in simulated data than any of these theoretical distributions was observed.

As a summary, the ensemble modelling results indicated that random wave-induced excess pore pressure and the maximum liquefaction depth exceeded that for the comparable regular waves. This means that the conventional approach of using a representative wave corresponding to the mean value of random waves to determine liquefaction potential could underestimate the maximum liquefaction depth and produce unsafe design in engineering practice. Therefore, a higher exceedance probability in the wave height distribution instead of mean values such as significant wave height or root-mean-square wave height should be adopted. Alternatively, an ensemble modelling similar to what has been done in this thesis should be carried out so as to provide a probability distribution of the liquefaction depth.

7.1.2 **Two-layer viscid fluid system for wave-liquefied soil interaction**

In Chapter 5, a two-layer viscid fluid system was constructed. Regarding the shear strain rate-dependent viscosity and phase transition of liquefied soil, a visco-elastic–plastic model employed by Oveisy *et al.* (2009) for fluid mud was used as a first approximation. Furthermore, the wave-induced shear stress was estimated by an analytical solution for a seabed with finite thickness. Prior to analysis, the new model was verified by being reduced to two-layer viscid model with a constant liquefied soil viscosity. The same liquefaction results were reproduced. When calculating the liquefied soil viscosity, the shear strain rate and objective of the deformation tensor were averaged through the liquefied soil layer. With the rheological model for liquefied soil being integrated, the computed fluid motion and viscosity compared well with the results in existing literature.

Based on the model established, the significant influence of shear stress solution on liquefaction was confirmed. Shear stress solution for the seabed with finite thickness was slightly greater than that for the seabed with infinite thickness. The relative small difference in shear stress was amplified by the exponential function appears in source term of residual pore pressure build-up equation. The appreciable difference in interface wave amplitude determined by finite and infinite solution is related to the corresponding difference in liquefaction progress.

To examine the effect of strain rate dependent viscosity, water content was inversely determined by the same liquefied soil used in Liu *et al.* (2009). Using the water content, the present model predicted a final liquefaction depth smaller than that by the model with a constant viscosity. The liquefied soil viscosity was observed to experience a transition from visco-elstic to visco-plastic phase. Although the water content was

included in the function of rheological model, it was found to have only non-significant influence on the liquefaction depth even though water content influenced the predicted viscosity much more.

A parametric study was conducted to investigate influence of both wave parameters and soil properties on the liquefaction and liquefied soil viscosity. Under the condition of same wave height, shallower water depth led to smaller wave pressure on surface of sub-liquefied seabed and consequently a shallower liquefaction depth. The relationship between water depth and final liquefaction depth was nonlinear because of the non-linearity of the model. Residual pore pressure in seabed induced by shorter wave period was unlikely to dissipate in one cycle. As a result, the final liquefaction was deeper. Influences of both water depth and wave period on the viscosity of liquefied soil were negligible. More permeable soil created a better drainage condition for the dissipation of excess pore pressure and consequently reduced the liquefaction depth.

The liquefaction progress predicted was also very sensitive to the model parameters which were introduced by Sassa *et al*. (2001) to describe cyclic plasticity of soil. Therefore, a clear identification procedure of these parameters is of great importance in the prediction of liquefaction.

In summary, the two-layer viscid fluid system approach with a visco-elasto-plastic rheological model for liquefied soil is able to predict a varying viscosity. However, the relative difference made by it is not important concerning the final liquefaction depth. Shorter wave in shallower water zone is more likely to cause liquefaction in a less permeable seabed. It implies that seabed morphology and its evolution induced by wave loading should be taken into account. Obviously, the wave height plays an important role as well. Therefore, a multiple dimensional model which can copes with wave

energy attenuation caused by various factors (such as morphology and wave-liquefied soil interaction, etc.) and seabed elevation change is strongly desired.

7.1.3 **Multi-layer viscous fluid system for wave-liquefied soil interaction**

In the two-layer viscous fluid system model, shear strain rate-dependent viscosity of liquefied soil has been confirmed to affect seabed liquefaction progress even though not profound. However, the two-layer fluid system makes a serious approximation that the viscosity is constant through the depth of liquefied soil. This is due to the restriction in the frame of two-layer system that the entire liquefied soil is assumed to be a uniform layer with respect to the viscosity despite the shear strain rate varies along depth. To investigate the effect of stratification of liquefied soil layer, a multi-layer viscous fluid system was constructed in Chapter 6.

Recognizing the water content in rheological model can also affect density of liquefied soil, the density in the multi-layer model was expressed in terms of soil grain density and water content ratio. To allow an automatically increasing number of fluid layers, the related derivation and coding were conducted. Comparison with the model used in Chapter 5 confirmed the performance of the newly constructed multi-layer model.

N-layer model is able to give a distribution of liquefied soil viscosity at every simulation time instant. Using the same parameters, N-layer model produced a different viscosity values relative to two-layer model. In a practical range of water content of liquefied soil, the final liquefaction depths determined by the two models differed a lot. Which depth was deeper and whether the extent of difference was significant depended on the specific water content value used. For the relative denser liquefied soil, the two-

layer model possibly predicted no liquefaction, whilst N-layer model could produce a relative liquefaction depth (i.e., liquefaction depth normalized by seabed thickness) close to 60%. Meanwhile, the liquefaction depth estimated using the N-layer model was sensitive to water content, which was contrary to the finding made by the two-layer model. Moreover, the visco-plastic phase viscosity predicted by multi-layer model was much smaller than that by two-layer model. Therefore, more laboratory experiments need be performed to clarify to what extent the water content of liquefied soil can affect the seabed liquefaction progress.

To investigate the effect of varying liquefied soil density through liquefied soil layer on liquefaction, a linearly decreasing water content pattern was assumed. The continuously increasing liquefied soil density was found to ease the numerical difficulty in achieving a convergent viscosity. The results of liquefied soil viscosity, liquefaction depth and interface wave amplitude differed from that predicted by constant water content model.

Under the condition of same wave height, shorter wave period in shallower water can liquefy the underlying seabed easier. This conclusion was same as that obtained by two-layer model; however, the final liquefaction depth was more sensitive to the associated parameters in N-layer model. Nevertheless, the viscosity of liquefied soil is not sensitive to both wave period and water depth.

A same ‘enhancing’ phenomenon was also observed for the effect of soil parameters on the liquefaction depth. In N-layer model, the increasing hydraulic conductivity decreased the liquefaction depth more effectively. The thickness of seabed was also found to affect liquefaction but the relation was not monotony. There seemed to be a critical seabed thickness, at which the effect of seabed thickness on liquefaction

reverses. Below the critical thickness, the liquefaction depth was smaller due to the relatively short drainage distance in thinner seabed. Beyond the critical thickness, the increasing seabed thickness damped the wave energy and consequently prevented the liquefaction. Soil shear modulus made no notable difference in the final liquefaction depth though the liquefaction front can advance slightly deeper in softer seabed.

Similar to the conclusion drawn by the two-layer model, seabed liquefaction was very sensitive to the soil plastic model parameters, especially α, β and R which are involved in residual pore pressure build-up equation. Therefore, a reliable identification procedure for them is extremely important.

As a conclusion, varying of liquefied soil density and viscosity makes a significant influence on liquefaction progress. The sensitivity of liquefaction to both wave and soil parameters are enhanced by the stratification of liquefied soil viscosity and density. Therefore, it is essential to investigate the properties of liquefied soil in more laboratory and field tests. Since shorter wave in shallower water is more likely to cause liquefaction risk in less permeable softer seabed, theoretical study should pay attention to these factors. A strategy to prevent liquefaction is to improve the drainage condition for excess residual pore pressure within seabed and ensure a sufficient overburden.

7.2 Recommendations for future research

Throughout this study, free seabed progressive liquefaction with a particular emphasis on random linear progressive wave, in-viscous or viscous property of liquefied soil were investigated using both analytical and numerical means. While the present study has extended current knowledge in this area, the following tasks need to be further considered in future studies.

7.2.1 **Experimental works required**

The material parameters, α, β, R used to calculate plastic volumetric strain rate in source term are after Sassa *et al.* (2001). Unfortunately, they were originally determined inversely so that the predicted liquefaction results may consistently reproduced the centrifuge experiments. This means that these parameters cannot be used in other modelling approaches without doubt. Moreover, they cannot be extrapolated to general seabed materials. When we compared the two divisions of equations for the prediction of excess pore pressure build-up in Chapter 2, it has been shown that these parameters in fact related to soil compress coefficient, m_v and the plastic property under cyclic loading. More experiments need be done to construct a general form of this source term and determine the range of parameters for typical seabed materials.

The multi-layer fluid system modelling approach allows varying characteristics of sub-layers of liquefied soil to be specified. In this study, a shear strain-dependent viscosity is accounted for. The other parameter of liquefied soil involved in the linearized Navier-Stokes equations is the density. Sumer *et al.* (2006) conducted small scale experiments to measure the density of liquefied silt soil. A pipe buried in soil was used as a hydrometer and the density of liquefied soil was observed to vary with depth. However, the hydrodynamic model proposed by Sumer *et al.* (2006) based on the balance of liquefies soil gain was unable to capture the variation of density of liquefied soil with soil depth. Therefore, more investigations into the density of liquefied soil and a mathematical model to describe its change along depth would be meaningful.

7.2.2 **Relaxation of some model restrictions**

In this study, wave-induced shear stress was estimated by the solution proposed by Jeng and Hsu (1996) which prescribed that the shear stress vanishes at the water-seabed interface. Since the heavy liquefied soil is of a much greater viscosity relative to seawater, the shear stress due to viscous liquefied soil may affect soil response to wave remarkably. So far, there is no analytical solution for seabed response to progressive wave considering the shear stress at seabed surface. On the other hand, Jeng (2008) examined seabed residual liquefaction under the act of the second-order Stokes wave and stated that nonlinear wave results in much greater residual pore pressure along sediment depth especially in a soft seabed. Moreover, when modelling the interaction of progressive waves propagating over a layer of viscous fluid mud, Zhang and Ng (2006) found that model with nonlinear Navier-Stokes equations compared more favourably with the experimental data than the prediction made by a linear theory. In other words, neglecting the nonlinear convective accelerations in Navier-Stokes equations may not adequate when the density and viscosity of mud increase. Therefore, a numerical model is desired to solve the nonlinear wave propagating over viscous fluid layer and consider the nonzero shear stress due to heavy viscous liquid at surface of seabed when determining the soil shear stress.

In estimating the effect of random wave, three advances can be made. Firstly, the shear stresses solution after Sassa *et al.* (2001) is strictly applicable only to linear harmonic waves. Thus, a solution of seabed response to random linear wave could be employed to replace it. Secondly, if the soil parameters or model parameters are deemed to be uncertain and be included in the ensemble modelling, the full random parameter spaces can be covered. Finally, the temporal scale of liquefaction and densification

should be included. When sediment is subject to the action of a random wave time series, the liquefaction is mainly affected by large waves in the time series. In between the time of large waves the sediment bed can experience densification as the pore pressure within the bed may have time to dissipate. In general situation, neither the liquefaction front nor the densification front will maintain a one way movement (up or down). As a result the time scales for the liquefaction and densification processes may not be easily separated as in the regular wave situation. In this sense, it is essential to determine the liquefaction and densification process simultaneously.

7.2.3 **Extension to multi-dimensions**

The restriction to one-dimensional is a serious bottleneck for the progressive liquefaction model being applied in more coastal engineering problems, such as stability of seabed around a buried pipeline and wind turbines supported on mono-piles. For example, the liquefied soil may solidify under the repeated wave loading and the subsequent liquefaction will be resisted due to the denser soil particle arrangement (Sassa and Sekiguchi, 1999). The implication is that a limited local liquefaction could not be destructive to pipeline. Based on the ideas of this thesis, the liquefied soil and sub-liquefied seabed can be modeled as poro-elasto-plastic and poro-elastic material, respectively. An integrated system of the Navier-Stokes equations and Biot consolidation equations can be established. The Volume-of-fluid (VOF) technique (Hirt and Nichols, 1981; Sassa *et al.*, 2003) can be used to trace the moving interface between the ambient water and the liquefied soil. However, the zone beneath structure may reach liquefied state earlier than the vicinity, i.e., there exist liquefied soil zone wrapped by sub-liquefied soil. An efficient method to handle the arbitrary interface and switch the

different governing equations is unknown yet. Prior to construction of a workable analysis procedure for describing the progressive liquefaction in seabed around structure, these problems required to be resolved.

APPENDIX A: Derivation of Pore Fluid Storage Equation

On the basis of simple plasticity model, Sassa and Sekiguchi (1999) proposed the pore fluid storage equation which was used to describe the process of the build-up of the residual pore pressure in a partially drained soil subjected to cyclic shearing due to fluid waves.

Suppose the volumetric strain increment $\Delta\epsilon_{vol}$ of an element of saturated sand under cyclic loading is sum of an elastic component $\Delta\epsilon_{vol}^{(1)}$ and a plastic component $\Delta\epsilon_{vol}^{(2)}$ as

$$\Delta\epsilon_{vol} = \Delta\epsilon_{vol}^{(1)} + \Delta\epsilon_{vol}^{(2)} \tag{A.1}$$

Since the elastic component $\Delta\epsilon_{vol}^{(1)}$ can be described in term of the increment of the vertical effective stress $\Delta\sigma_v'$, and the coefficient of compressibility of the soil skeleton, m_v, differentiation of the volumetric strain increment $\Delta\epsilon_{vol}$ with respect to time is written as

$$\frac{\partial\Delta\epsilon_{vol}}{\partial t} = m_v\frac{\partial\Delta\sigma_v'}{\partial t} + \frac{\partial\Delta\epsilon_{vol}^{(2)}}{\partial t} \tag{A.2}$$

On the other hand, the mass conservation of an incompressible pore fluid in a deformable soil may be expressed as

$$\frac{\partial\Delta\epsilon_{vol}}{\partial t} = -\frac{k_D}{\gamma_f}\left(\frac{\partial^2 u_e}{\partial x^2} + \frac{\partial^2 u_e}{\partial z^2}\right) \tag{A.3}$$

in which k_D denotes the coefficient of soil hydraulic conductivity, γ_f is the unit weight of the fluid and u_e is the excess pore pressure For a one-dimensional problem, Eq.(A.3) reduces to

$$\frac{\partial \Delta \epsilon_{\text{vol}}}{\partial t} = -\frac{k_D}{\gamma_f}\frac{\partial^2 u_e}{\partial z^2} \tag{A.4}$$

$$\frac{\partial \Delta \epsilon_{\text{vol}}}{\partial t} = -\frac{K}{\mu}\frac{\partial^2 u_e}{\partial z^2} \tag{A.5}$$

where K is the intrinsic permeability coefficient and μ is the dynamic viscosity of the pore fluid (e.g. Rumer (1969)). Substitution of Eq. Eq. (A.2) into Eq. Eq. (A.5) and applying the concept of effective stress yields

$$m_v\left(\frac{\partial \sigma_v}{\partial t} - \frac{\partial u}{\partial t}\right) + \frac{\partial \Delta \epsilon_{\text{vol}}^{(2)}}{\partial t} = -\frac{K}{\mu}\frac{\partial^2 u_e}{\partial z^2} \tag{A.6}$$

herein view of that the time averages of total stress change, $\overline{\sigma_v}$ and transient pore pressure, $\bar{u}_e^{(2)}$ over a wave cycle is zero, the above equation becomes

$$\frac{\partial u_e^{(2)}}{\partial(\omega t)} = \frac{K}{m_v \mu \omega}\frac{\partial^2 u_e^{(2)}}{\partial z^2} + \frac{1}{m_v}\frac{\partial \Delta \epsilon_{\text{vol}}^{(2)}}{\partial(\omega t)} \tag{A.7}$$

With the non-dimensional parameter κz, Eq. (A.7) may be rewritten as

$$\frac{\partial u_e^{(2)}}{\partial(\omega t)} = \frac{K}{m_v \mu \omega}\kappa^2\frac{\partial^2 u_e^{(2)}}{\partial(\kappa z)^2} + \frac{1}{m_v}\frac{\partial \Delta \epsilon_{\text{vol}}^{(2)}}{\partial(\omega t)} \tag{A.8}$$

The plastic component $\Delta \epsilon_{\text{vol}}^{(2)}$ reflects the contractive nature of the loosely packed sand subjected to cyclic shearing. Sassa *et al.* (2001) used Φ and $\mathrm{M}\,\partial \upsilon^{\mathrm{p}} / \partial \xi$ to replace the corresponding coefficient or term on RHS.

APPENDIX B: Lamb's Theory for Wave Propagation in a Two-layer Fluid System

Lamb (1932) presented a solution for a small-amplitude sinusoidal fluid wave propagating in a two-layer fluid of a finite thickness as shown in Fig. 3.2. The wave length is L and the wave period is T. The system is in a gravitational field of *Ng* (*g* is gravity acceleration). For an incompressible fluid, its irrotational motion can be described by the Laplace equations as follows

$$\frac{\partial^2 \phi_1}{\partial x^2} + \frac{\partial^2 \phi_1}{\partial z^2} = 0, \qquad \text{for region } I \tag{B.1}$$

$$\frac{\partial^2 \phi_2}{\partial x^2} + \frac{\partial^2 \phi_2}{\partial z^2} = 0, \qquad \text{for region } II \tag{B.2}$$

where ϕ_1 and ϕ_2 denote velocity potentials for region *I* and *II*, respectively.

Let the vertical displacement of the surface wave $\tilde{m}_0$ and the vertical displacement of the interfacial wave $\tilde{a}_0$ be defined as follows (Fig. 3.2(a)).

$$\tilde{m}_0 = m_0 exp\{i(\kappa x - \omega t)\} \tag{B.3}$$

$$\tilde{a}_0 = a_0 exp\{i(\kappa x - \omega t)\} \tag{B.4}$$

in which κ represents the wave number defined by $2\pi/L$ and ω denotes the wave angular frequency defined by $2\pi/T$. Thus, the velocity potentials ϕ_1 and ϕ_2 can be assumed to take the following forms (Lamb, 1932):

$$\phi_1 = (Acosh\kappa z + Bsinh\kappa z) exp\{i(\kappa x - \omega t)\} \tag{B.5}$$

$$\phi_2 = (Ccoshκz + Dsinhκz)exp\{i(κx - ωt)\} \tag{B.6}$$

The fluid system is subjected to the boundary conditions as following:

a) Free-surface boundary conditions at $z = h$:

$$\frac{\partial \tilde{m}_0}{\partial t} = -\frac{\partial \phi_1}{\partial z} \tag{B.7}$$

$$\tilde{m}_0 = \frac{1}{Ng}\frac{\partial \phi_1}{\partial t} \tag{B.8}$$

b) Interfacial boundary conditions at $z = 0$:

$$\frac{\partial \tilde{a}_0}{\partial t} = -\frac{\partial \phi_1}{\partial z} = -\frac{\partial \phi_2}{\partial z}, \tag{B.9}$$

$$\rho_1 \frac{\partial \phi_1}{\partial t} - \rho_1 Ng\tilde{a}_0 = \rho_2 \frac{\partial \phi_2}{\partial t} - \rho_2 Ng\tilde{a}_0. \tag{B.10}$$

c) Bottom boundary condition at $z = z_L$:

$$\frac{\partial \phi_2}{\partial z} = 0. \tag{B.11}$$

Introducing (B.5) and (B.6) into (B.7), (B.8), (B.9), (B.10), (B.11), yields the relations between the coefficients for solutions:

$$κAsinhκh + κBcoshκh = -iωm_0 \tag{B.12}$$

$$-iω(Acoshκh + Bsinhκh) = m_0 \tag{B.13}$$

$$κB = κD = iωa_0 \tag{B.14}$$

$$(\rho_2 C - \rho_1 D)i\omega = (\rho_1 - \rho_2)Nga_0 \tag{B.15}$$

$$Csinh\kappa z_L + Dcosh\kappa z_L = 0 \tag{B.16}$$

Therefore, the parameters A through D appearing in Eq. (B.5) and Eq. (B.6) can be determined as:

$$A = ia_0\left\{\frac{(\rho_1 - \rho_2)Ng}{\rho_1\omega} - \frac{\rho_2\omega}{\rho_1\kappa tanh(\kappa z_L)}\right\} \tag{B.17}$$

$$B = ia_0\frac{\omega}{\kappa} \tag{B.18}$$

$$C = -ia_0\frac{\omega}{\kappa tanh(kz_L)} \tag{B.19}$$

$$D = B = ia_0\frac{\omega}{\kappa} \tag{B.20}$$

The dispersion relationship for the two-layer fluid is also derived as

$$\left[1 - \left(\frac{Ng\kappa}{\omega^2}\right)^2\right] tanh(\kappa h)tanh(\kappa z_L) = \frac{\rho_2}{\rho_1}\left[1 - \frac{Ng\kappa}{\omega^2}tanh(\kappa h)\right]\left[1 + \frac{Ng\kappa}{\omega^2}tanh(\kappa z_L)\right] \tag{B.21}$$

It is instructive to note that under specific conditions of $z_L = 0$, Eq. (B.21) yields the dispersion relationship for the one-layer fluid:

$$\omega^2 = Ng\kappa_0 tanh(\kappa_0 h) \tag{B.22}$$

where κ_0 denotes the wave number for the one-layer fluid.

The theory as described above provides the expressions for the wave-induced pressure oscillation in the system under consideration. Using the linearized Bernoulli equation, the fluid pressure oscillation $\tilde{u}_0$ at depth $z = 0$ may be expressed as follows:

$$\tilde{u}_0 = \lim_{z \to +0} \rho_1 \frac{\partial \phi_1}{\partial t} \tag{B.23}$$

Hence, the amplitude of $\tilde{u}_0$ may then be expressed as follows (Fig. 3.2).

$$u_0 = -\frac{\rho_2 \omega^2 + (\rho_2 - \rho_1) N g \kappa tanh(\kappa z_L)}{\kappa tanh(\kappa z_L)} a_0 \tag{B.24}$$

where, a_0 is the amplitude of vertical displacement at $z = 0$.

The amplitude of oscillatory pore pressure $u_e^{(1)}$at depth $z_L \leq z < 0$ may be derived by using the relation $\tilde{u}_e^{(1)} = \rho_2 \partial \phi_2 / \partial\, t$ as follows.

$$u_e^{(1)} = \frac{\rho_2 \omega^2 [cosh(\kappa z) - sinh(\kappa z) tanh(\kappa z_L)]}{\rho_2 \omega^2 + (\rho_2 - \rho_1) N g \kappa tanh(\kappa z_L)} u_0 \tag{B.25}$$

The expression for the amplitude of fluid pressure fluctuation, u_L at $z = z_L$ may then be derived by replacing z in Eq. (B.25) by z_L. Namely,

$$u_L = \frac{\rho_2 \omega^2}{\rho_2 \omega^2 cosh(\kappa z_L) + (\rho_2 - \rho_1) N g \kappa sinh(\kappa z_L)} u_0 \tag{B.26}$$

The amplitude of the vertical displacement of the surface, m_0, at $z = h$ may be related to the amplitude of the vertical displacement of the fluid-soil interface, a_0, at $z = 0$. From Eq. (B.8), it reads

$$m_0 = \frac{\omega^2}{cosh(\kappa h)[\omega^2 - Ng\kappa sinh(\kappa h)]} a_0 \tag{B.27}$$

APPENDIX C: Poro-elastic Solutions for Wave-induced Soil Stress in Seabed of Infinite Thickness

Based on the assumptions that the pore fluid is incompressible and Darcy law governs the isotropic flow, Madsen (1978) and Yamamoto *et al.* (1978) devoloped a closed-form solution for the response of a semi-infinite, homogeneous poro-elastic medium under progressive-wave loading using poro- elasticity theory.

The coordinate system and sign convention adopted here are illustrated in Fig. C. 1, where σ_x' and σ_z' denote the effective normal stresses in the x and z directions, respectively. And the horizontal shear stress is represented by τ_{zx}. Let u_e be the excess pore pressure, the boundary conditions at the top of the bed are

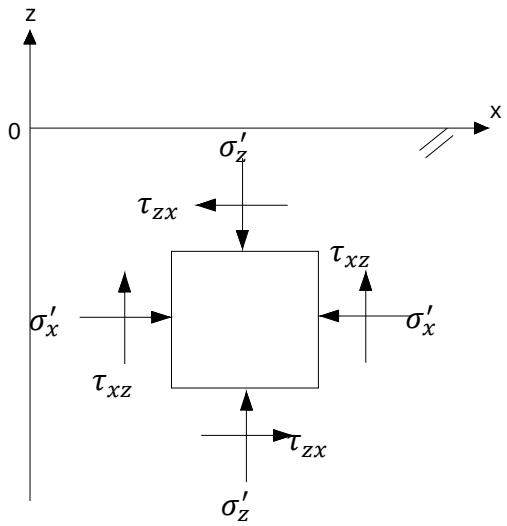

Fig. C. 1 Sign convention for stresses

$$\tilde{u}_0 = \tilde{\sigma}_z = u_0 cos(\kappa x - \omega t) \qquad \text{On } z = 0 \qquad \text{(C.1)}$$

$$\sigma_z' = 0 \qquad \text{On } z = 0 \qquad \text{(C.2)}$$

$$\tilde{\tau}_{zx} = 0 \qquad \text{On } z = 0 \qquad \text{(C.3)}$$

Here u_0 is the amplitude of the pressure oscillation at the soil surface. The solutions derived are (for $z < 0$):

$$\Delta\sigma_x' = u_0 \kappa z exp(\kappa z) cos(\kappa x - \omega t) \tag{C.4}$$

$$\Delta\sigma_z' = -u_0 \kappa z exp(\kappa z) cos(\kappa x - \omega t) \tag{C.5}$$

$$\Delta\tau_{zx} = u_0 \kappa z exp(\kappa z) sin(\kappa x - \omega t) \tag{C.6}$$

$$\Delta u = u_e^{(1)} = u_0 exp(\kappa z) cos(\kappa x - \omega t) \tag{C.7}$$

The associated change in the maximum shear stress is expressed by

$$\Delta\tau_{max} = \sqrt{\left(\frac{\Delta\sigma_z' - \Delta\sigma_x'}{2}\right)^2 + (\ \Delta\tau_{zx})^2} \tag{C.8}$$

$$\Delta\tau_{max} = u_0 \kappa |z| exp(\kappa z) \tag{C.9}$$

APPENDIX D: Coefficients Used in the Finite Solution for Wave-induced Soil Stress

Coefficients C_j in Eq. (5.48) and Eq. (5.49) can be expressed as

$C_j = D_j/D_0$ for $j = 1, \cdots, 6$

where

$$\begin{aligned} D_j = {} & C_{j0} + C_{j1}\, exp(-2\kappa_0 z) \\ & + C_{j2}\, exp[-(\kappa_0 + \delta)z] \\ & + C_{j3}\, exp(-4\kappa_0 z) \\ & + C_{j4}\, exp(-2\delta z) \\ & + C_{j5}\, exp[-2(\kappa_0 + \delta)z] \\ & + C_{j6}\, exp[-(3\kappa_0 + \delta)z] \\ & + C_{j7}\, exp[-(4\kappa_0 + 2\delta)z] \end{aligned} \qquad \text{For } j = 1, \cdots, 6 \qquad \text{(D.1)}$$

The common denominator D_0 can be calculated by inserting the following coefficients into Eq. (D.1)

$$C_{00} = (\delta - \kappa_0)^2(\delta - \delta\mu + \kappa_0\mu)B_1 \qquad \text{(D.2)}$$

$$C_{01} = -2\delta[(\kappa_0^2\mu - \delta^2 + \delta^2\mu)^2 + \kappa_0^4(1-2\mu)^2 + 2\kappa_0^2 z^2(1-\mu)^2(\delta^2-\kappa_0^2)^2] + 4\kappa_0^2 z(\delta^4-\kappa_0^4)(1-2\mu)(1-\mu) \tag{D.3}$$

$$C_{02} = -8\delta\kappa_0^2(1-2\mu)[\kappa_0 z(\delta^2-\kappa_0^2)(1-\mu) - \delta^2(1-\mu) + \kappa_0^2\mu] \tag{D.4}$$

$$C_{03} = (\delta+\kappa_0)^2(\delta - \delta\mu - \kappa_0\mu)B_2 \tag{D.5}$$

$$C_{04} = C_{03} \tag{D.6}$$

$$C_{05} = C_{01} - 8\kappa_0^2 z(\delta^4-\kappa_0^4)(1-2\mu)(1-\mu) \tag{D.7}$$

$$C_{06} = C_{02} + 16\delta\kappa_0^3 z(\delta^2-\kappa_0^2)(1-\mu)(1-2\mu) \tag{D.8}$$

$$C_{07} = C_{00} \tag{D.9}$$

The final expression of coefficients C_1 to C_6 can be obtained from $\mathrm{C_j} = \mathrm{D_j}/\mathrm{D_0}$ using Eq. (D.1) in conjunction with the coefficients

$$C_{11} = 2\kappa_0^2 z(\delta+\kappa_0)(\delta - \delta\mu - \kappa_0\mu) \tag{D.10}$$

$$C_{12} = 4\delta\kappa_0^3 z(1-2\mu)(\delta^2 - \delta^2\mu - \kappa_0^2\mu) \tag{D.11}$$

$$C_{15} = 2\kappa_0^2 z(\delta-\kappa_0)(\delta - \delta\mu + \kappa_0\mu)B_4 \tag{D.12}$$

$$C_{20} = C_{00} \tag{D.13}$$

$$C_{21} = C_{03} + (\delta+\kappa_0)^2(\delta - \delta\mu - \kappa_0\mu)B_5 \tag{D.14}$$

$$C_{22} = 4\delta\kappa_0^2(1-2\mu)[2\delta^2(1-\mu) - 2\kappa_0^2\mu - \kappa_0 z(1-\mu)(\delta^2-\kappa_0^2)] \quad \text{(D.15)}$$

$$C_{24} = C_{03} \quad \text{(D.16)}$$

$$C_{25} = C_{00} + (\delta-\kappa_0)^2(\delta - \delta\mu + \kappa_0\mu)B_6 \quad \text{(D.17)}$$

$$C_{31} = 2\kappa_0^2 z(\delta-\kappa_0)(\delta - \delta\mu + \kappa_0\mu)B_3 \quad \text{(D.18)}$$

$$C_{35} = 2\kappa_0^2 z(\delta+\kappa_0)(\delta - \delta\mu - \kappa_0\mu)B_4 \quad \text{(D.19)}$$

$$C_{36} = -C_{21} \quad \text{(D.20)}$$

$$C_{41} = C_{25} - 2C_{00} \quad \text{(D.21)}$$

$$C_{45} = C_{21} - 2C_{03} \quad \text{(D.22)}$$

$$C_{46} = 4\delta\kappa_0^2(1-2\mu)[2\kappa_0^2\mu - 2\delta^2(1-\mu) - \kappa_0 z(1-\mu)(\delta^2-\kappa_0^2)] \quad \text{(D.23)}$$

$$C_{47} = -C_{20} \quad \text{(D.24)}$$

$$C_{51} = -4\kappa_0^2 z(1-2\mu)B_3 \quad \text{(D.25)}$$

$$C_{52} = -2\kappa_0^2 z(\delta+\kappa_0)(1-2\mu)(\delta - \delta\mu - \kappa_0\mu) \quad \text{(D.26)}$$

$$C_{56} = -2\kappa_0^2 z(\delta-\kappa_0)(1-2\mu)(\delta - \delta\mu + \kappa_0\mu) \quad \text{(D.27)}$$

$$C_{62} = -C_{56} \quad \text{(D.28)}$$

$$C_{65} = -4\kappa_0^2 z(1-2\mu)B_4 \quad \text{(D.29)}$$

$$C_{66} = -C_{52} \quad \text{(D.30)}$$

The six B coefficients in Eq. (D.2)-Eq. (D.30) are given by

$$B_1 = \kappa_0^2\mu - (1-\mu)(\delta^2 + \delta\kappa_0 + \kappa_0^2) \tag{D.31}$$

$$B_2 = -\delta^2 + \delta\kappa_0 - \kappa_0^2 + \delta^2\mu - \delta\kappa_0\mu + 2\kappa_0^2\mu \tag{D.32}$$

$$B_3 = (\delta^3 z - \kappa_0^2 - \delta\kappa_0^2 z)(1-\mu) + \kappa_0^2\mu \tag{D.33}$$

$$B_4 = (\delta^3 z + \kappa_0^2 - \delta\kappa_0^2 z)(1-\mu) - \kappa_0^2\mu \tag{D.34}$$

$$B_5 = 2\delta\kappa_0\mu(\delta - \kappa_0)(1-\mu) \tag{D.35}$$

$$B_6 = 2\delta\kappa_0\mu(\delta + \kappa_0)(1-\mu) \tag{D.36}$$

There are also zero-value coefficients, such as

$$C_{10} = C_{13} = C_{14} = C_{16} = C_{17} = 0 \tag{D.37}$$

$$C_{23} = C_{26} = C_{27} = 0 \tag{D.38}$$

$$C_{30} = C_{32} = C_{33} = C_{34} = C_{37} = 0 \tag{D.39}$$

$$C_{40} = C_{42} = C_{44} = 0 \tag{D.40}$$

$$C_{50} = C_{53} = C_{54} = C_{55} = C_{57} = 0 \tag{D.41}$$

$$C_{60} = C_{61} = C_{63} = C_{64} = C_{67} = 0 \tag{D.42}$$

APPENDIX E: Coefficients Used in the Navier-Stokes Equation for Two-layer Fluid System

The coefficients $A-H,$ the amplitude of interface wave a_2 and wave number κ can be solved from Eq. (E.1) to (E.10) by substitution and iteration methods. As follows:

$$Ae^{\kappa h}+Be^{-\kappa h}+Ce^{\lambda_1 h}+De^{-\lambda_1 h}=-i\omega a_1 \tag{E.1}$$

$$M_1(Ae^{\kappa h}-Be^{-\kappa h})-2\rho_1\nu_1\lambda_1\left[Ce^{\lambda_1 h}-De^{-\lambda_1 h}\right]=\rho_1 g a_1 \tag{E.2}$$

$$2\kappa^2(Ae^{\kappa h}+Be^{-\kappa h})+(\lambda_1^2+\kappa^2)\left(Ce^{\lambda_1 h}+De^{-\lambda_1 h}\right)=0 \tag{E.3}$$

$$A+B+C+D=-i\omega a_2 \tag{E.4}$$

$$A+B+C+D=Ee^{\kappa z_L}+Fe^{-\kappa z_L}+Ge^{\lambda_2 z_L}+He^{\lambda_2 z_L} \tag{E.5}$$

$$\kappa A-\kappa B+\lambda_1 C-\lambda_1 D=\kappa Ee^{\kappa z_L}-\kappa Fe^{-\kappa z_L}+\lambda_2 Ge^{\lambda_2 z_L}-\lambda_2 He^{\lambda_2 z_L} \tag{E.6}$$

$$\begin{aligned}M_1(A-B)-2\rho_1\nu_1\lambda_1(C-D)&\\ =M_2(Ee^{\kappa z_L}-Fe^{-\kappa z_L})-2\rho_2\nu_2\lambda_2\left(Ge^{\lambda_2 z_L}-He^{\lambda_2 z_L}\right)&\\ -(\rho_2-\rho_1)ga_2&\end{aligned} \tag{E.7}$$

$$\begin{aligned}\rho_1\nu_1[2\kappa^2(A+B)+(\lambda_1^2+\kappa^2)(C+D)]&\\ =\rho_2\nu_2\left[2\kappa^2(Ee^{\kappa z_L}+Fe^{-\kappa z_L})\right.&\\ \left.+(\lambda_1^2+\kappa^2)\left(Ge^{\lambda_2 z_L}+He^{\lambda_2 z_L}\right)\right]&\end{aligned} \tag{E.8}$$

$$\kappa(E-F)+\lambda_2(G-H)=0 \tag{E.9}$$

$$E + F + G + H = 0 \tag{E.10}$$

The coefficients A, B, C, D can be solved from (E.1), (E.2), (E.3) and (E.4). As follows:

(E.3)-(E.1) $\times 2\kappa^2$:

$$(\lambda_1^2 - \kappa^2)\left(Ce^{\lambda_1 h} + De^{-\lambda_1 h}\right) = 2i\omega a_1 \kappa^2 \tag{E.11}$$

Since

$$(\lambda_1^2 - \kappa^2) = -i\omega \nu_1^{-1} \tag{E.12}$$

So

$$Ce^{\lambda_1 h} + De^{-\lambda_1 h} = -2\nu_1 a_1 \kappa^2 \tag{E.13}$$

And

(E.3)-(E.1)$\times$ $(\lambda_1^2 + \kappa^2)$:

$$(\kappa^2 - \lambda_1^2)(Ae^{\kappa h} + Be^{-\kappa h}) = i\omega a_1(\lambda_1^2 + \kappa^2) \tag{E.14}$$

$$Ae^{\kappa h} + Be^{-\kappa h} = \nu_1 a_1(\lambda_1^2 + \kappa^2) \tag{E.15}$$

Then

$$\begin{cases} Ae^{\kappa h} = \nu_1 a_1(\lambda_1^2 + \kappa^2) - Be^{-\kappa h} \\ Ce^{\lambda_1 h} = -2\nu_1 a_1 \kappa^2 - De^{-\lambda_1 h} \end{cases} \tag{E.16}$$

$$\begin{cases} A = -Be^{-2\kappa h} + \nu_1 a_1(\lambda_1^2 + \kappa^2)e^{-\kappa h} \\ C = -De^{-2\lambda_1 h} - 2\nu_1 a_1 \kappa^2 e^{-\lambda_1 h} \end{cases} \tag{E.17}$$

Substitute Eq. (E.16), (E.17) into Eq. (E.2) and Eq. (E.4), yields

$$(1-e^{-2\kappa h})B+\left(1-e^{-2\lambda_1 h}\right)D = (\lambda_1^2-\kappa^2)\nu_1 a_2+2\nu_1 a_1\kappa^2 e^{-\lambda_1 h}-(\lambda_1^2+\kappa^2)\nu_1 a_1 e^{-\kappa h} \tag{E.18}$$

$$2M_1 e^{-\kappa h}B-4\rho_1\nu_1\lambda_1 e^{-\lambda_1 h}D = M_1(\lambda_1^2+\kappa^2)\nu_1 a_1+4\rho_1\nu_1^2\kappa^2\lambda_1 a_1-\rho_1 g a_1 \tag{E.19}$$

B, D, can be solved from Eq. (E.18) and (E.19) as

$$B=\frac{\left(1-e^{-2\lambda_1 h}\right)b_1+b_2 e^{-\lambda_1 h}\left(b_3 a_2+b_4 e^{-\lambda_1 h}-b_5 e^{-\kappa h}\right)}{(1-e^{-2\kappa h})b_2 e^{-\lambda_1 h}+2M_1(1-e^{-2\lambda_1 h})e^{-\kappa h}} \tag{E.20}$$

$$D=-\frac{(1-e^{-2\kappa h})b_1-2M_1 e^{-\kappa h}\left(b_3 a_2+b_4 e^{-\lambda_1 h}-b_5 e^{-\kappa h}\right)}{(1-e^{-2\kappa h})b_2 e^{-\lambda_1 h}+2M_1(1-e^{-2\lambda_1 h})e^{-\kappa h}} \tag{E.21}$$

where:

$$b_1=M_1(\lambda_1^2+\kappa^2)\nu_1 a_1+4\rho_1\nu_1^2\kappa^2\lambda_1 a_1-\rho_1 g a_1 \tag{E.22}$$

$$b_2=4\rho_1\nu_1\lambda_1 \tag{E.23}$$

$$b_3=(\lambda_1^2-\kappa^2)\nu_1 \tag{E.24}$$

$$b_4=2\nu_1 a_1\kappa^2 \tag{E.25}$$

$$b_5=(\lambda_1^2+\kappa^2)\nu_1 a_1 \tag{E.26}$$

$$M_1=\frac{i\rho_1\omega}{\kappa}-2\rho_1\nu_1\kappa \tag{E.27}$$

Use the same method

$$\begin{cases} Be^{-\kappa h} = \nu_1 a_1(\lambda_1^2 + \kappa^2) - Ae^{\kappa h} \\ De^{-\lambda_1 h} = -2\nu_1 a_1 \kappa^2 - Ce^{\lambda_1 h} \end{cases} \tag{E.28}$$

$$\begin{cases} B = -Ae^{2\kappa h} + \nu_1 a_1(\lambda_1^2 + \kappa^2)e^{\kappa h} \\ D = -Ce^{2\lambda_1 h} - 2\nu_1 a_1 \kappa^2 e^{\lambda_1 h} \end{cases} \tag{E.29}$$

$$\begin{aligned} &(1 - e^{2\kappa h})A + \left(1 - e^{2\lambda_1 h}\right)C \\ &\qquad = (\lambda_1^2 - \kappa^2)\nu_1 a_2 + 2\nu_1 a_1 \kappa^2 e^{\lambda_1 h} - (\lambda_1^2 + \kappa^2)\nu_1 a_1 e^{\kappa h} \end{aligned} \tag{E.30}$$

$$\begin{aligned} &2M_1 e^{\kappa h} A - 4\rho_1 \nu_1 \lambda_1 e^{\lambda_1 h} C \\ &\qquad = M_1(\lambda_1^2 + \kappa^2)\nu_1 a_1 + 4\rho_1 \nu_1^2 \kappa^2 \lambda_1 a_1 + \rho_1 g a_1 \end{aligned} \tag{E.31}$$

A, C, can be solved from Eqs. (E.30) and (E.31) as

$$A = \frac{\left(1 - e^{2\lambda_1 h}\right)b_6 + b_2 e^{\lambda_1 h}\left(b_3 a_2 + b_4 e^{\lambda_1 h} - b_5 e^{\kappa h}\right)}{(1 - e^{2\kappa h})b_2 e^{\lambda_1 h} + 2M_1(1 - e^{2\lambda_1 h})e^{\kappa h}} \tag{E.32}$$

$$C = -\frac{(1 - e^{2\kappa h})b_6 - 2M_1 e^{\kappa h}\left(b_3 a_2 + b_4 e^{\lambda_1 h} - b_5 e^{\kappa h}\right)}{(1 - e^{2\kappa h})b_2 e^{\lambda_1 h} + 2M_1(1 - e^{2\lambda_1 h})e^{\kappa h}} \tag{E.33}$$

where

$$b_6 = M_1(\lambda_1^2 + \kappa^2)\nu_1 a_1 + 4\rho_1 \nu_1^2 \kappa^2 \lambda_1 a_1 + \rho_1 g a_1 \tag{E.34}$$

from Eqs. (E.9), (E.10) yields:

$$G = -\frac{(\lambda_2 + \kappa)E + (\lambda_2 - \kappa)F}{2\lambda_2} \tag{E.35}$$

$$H = -\frac{(\lambda_2 - \kappa)E + (\lambda_2 + \kappa)F}{2\lambda_2} \tag{E.36}$$

for

$$Ee^{\kappa z_L} + Fe^{-\kappa z_L} + Ge^{\lambda_2 z_L} + He^{\lambda_2 z_L} = -i\omega a_2 \tag{E.37}$$

$$\kappa Ee^{\kappa z_L} - \kappa Fe^{-\kappa z_L} + \lambda_2 Ge^{\lambda_2 z_L} - \lambda_2 He^{\lambda_2 z_L} = \kappa(A - B) + \lambda_1(C - D) \tag{E.38}$$

substitute Eqs. (E.35), (E.36) into Eqs. (E.37), (E.38) yields,

$$\begin{cases} EF_{11} \cdot E + EF_{10} \cdot F = -i\omega a_2 \\ EF_{21} \cdot E - EF_{20} \cdot F = \kappa(A - B) + \lambda_1(C - D) \end{cases} \tag{E.39}$$

let

$$EF_{11} = e^{\kappa z_L} - \frac{\lambda_2 + \kappa}{2\lambda_2} e^{\lambda_2 z_L} - \frac{\lambda_2 - \kappa}{2\lambda_2} e^{-\lambda_2 z_L} \tag{E.40}$$

$$EF_{10} = e^{-\kappa z_L} - \frac{\lambda_2 - \kappa}{2\lambda_2} e^{\lambda_2 z_L} - \frac{\lambda_2 + \kappa}{2\lambda_2} e^{-\lambda_2 z_L} \tag{E.41}$$

$$EF_{21} = \kappa e^{\kappa z_L} - \frac{\lambda_2 + \kappa}{2\lambda_2} e^{\lambda_2 z_L} - \frac{\lambda_2 - \kappa}{2\lambda_2} e^{-\lambda_2 z_L} \tag{E.42}$$

$$EF_{20} = e^{-\kappa z_L} + \frac{\lambda_2 - \kappa}{2\lambda_2} e^{\lambda_2 z_L} - \frac{\lambda_2 + \kappa}{2\lambda_2} e^{-\lambda_2 z_L} \tag{E.43}$$

from Eq. (E.39), E, F can be solved as:

$$E = \frac{EF_{10}[\kappa(A - B) + \lambda_1(C - D)] - i\omega a_2 EF_{20}}{EF_{11}EF_{20} + EF_{21}EF_{10}} \tag{E.44}$$

$$F = \frac{EF_{11}[\kappa(A-B)+\lambda_1(C-D)]+i\omega a_2 EF_{21}}{EF_{11}EF_{20}+EF_{21}EF_{10}} \tag{E.45}$$

let

$$A = A_{10}a_2 + A_{11} \tag{E.46}$$

$$B = B_{10}a_2 + B_{11} \tag{E.47}$$

$$C = C_{10}a_2 + C_{11} \tag{E.48}$$

$$D = D_{10}a_2 + D_{11} \tag{E.49}$$

$$E = E_{10}a_2 + E_{11} \tag{E.50}$$

$$F = F_{10}a_2 + F_{11} \tag{E.51}$$

$$G = G_{10}a_2 + G_{11} \tag{E.52}$$

$$H = H_{10}a_2 + H_{11} \tag{E.53}$$

then

$$A_{10} = \frac{b_2 b_3 e^{\lambda_1 h}}{(1-e^{2\kappa h})b_2 e^{\lambda_1 h} + 2M_1(1-e^{2\lambda_1 h})e^{\kappa h}} \tag{E.54}$$

$$A_{11} = \frac{\left(1-e^{2\lambda_1 h}\right)b_6 + b_2 e^{\lambda_1 h}\left(b_4 e^{\lambda_1 h} - b_5 e^{\kappa h}\right)}{(1-e^{2\kappa h})b_2 e^{\lambda_1 h} + 2M_1(1-e^{2\lambda_1 h})e^{\kappa h}} \tag{E.55}$$

$$B_{10} = \frac{b_2 b_3 e^{-\lambda_1 h}}{(1-e^{-2\kappa h})b_2 e^{-\lambda_1 h} + 2M_1(1-e^{-2\lambda_1 h})e^{-\kappa h}} \tag{E.56}$$

$$B_{11} = \frac{\left(1 - e^{-2\lambda_1 h}\right) b_1 + b_2 e^{-\lambda_1 h}\left(b_4 e^{-\lambda_1 h} - b_5 e^{-\kappa h}\right)}{(1 - e^{-2\kappa h}) b_2 e^{-\lambda_1 h} + 2M_1 (1 - e^{-2\lambda_1 h}) e^{-\kappa h}} \tag{E.57}$$

$$C_{10} = -\frac{-2M_1 b_3 e^{\kappa h}}{(1 - e^{2\kappa h}) b_2 e^{\lambda_1 h} + 2M_1 (1 - e^{2\lambda_1 h}) e^{\kappa h}} \tag{E.58}$$

$$C_{11} = -\frac{(1 - e^{2\kappa h}) b_6 - 2M_1 e^{\kappa h}\left(b_4 e^{\lambda_1 h} - b_5 e^{\kappa h}\right)}{(1 - e^{2\kappa h}) b_2 e^{\lambda_1 h} + 2M_1 (1 - e^{2\lambda_1 h}) e^{\kappa h}} \tag{E.59}$$

$$D_{10} = -\frac{-2M_1 b_3 e^{-\kappa h}}{(1 - e^{-2\kappa h}) b_2 e^{-\lambda_1 h} + 2M_1 (1 - e^{-2\lambda_1 h}) e^{-\kappa h}} \tag{E.60}$$

$$D_{11} = -\frac{(1 - e^{-2\kappa h}) b_1 - 2M_1 e^{-\kappa h}\left(b_4 e^{-\lambda_1 h} - b_5 e^{-\kappa h}\right)}{(1 - e^{-2\kappa h}) b_2 e^{-\lambda_1 h} + 2M_1 (1 - e^{-2\lambda_1 h}) e^{-\kappa h}} \tag{E.61}$$

$$E_{10} = \frac{EF_{10}[\kappa(A_{10} - B_{10}) + \lambda_1 (C_{10} - D_{10})] - i\omega EF_{20}}{EF_{11} EF_{20} + EF_{21} EF_{10}} \tag{E.62}$$

$$E_{11} = \frac{EF_{10}[\kappa(A_{11} - B_{11}) + \lambda_1 (C_{11} - D_{11})]}{EF_{11} EF_{20} + EF_{21} EF_{10}} \tag{E.63}$$

$$F_{10} = \frac{EF_{11}[\kappa(A_{10} - B_{10}) + \lambda_1 (C_{10} - D_{10})] + i\omega EF_{21}}{EF_{11} EF_{20} + EF_{21} EF_{10}} \tag{E.64}$$

$$F_{11} = \frac{EF_{11}[\kappa(A_{11} - B_{11}) + \lambda_1 (C_{11} - D_{11})]}{EF_{11} EF_{20} + EF_{21} EF_{10}} \tag{E.65}$$

$$G_{10} = -\frac{(\lambda_2 + \kappa) E_{10} + (\lambda_2 - \kappa) F_{10}}{2\lambda_2} \tag{E.66}$$

$$G_{11} = -\frac{(\lambda_2 + \kappa) E_{11} + (\lambda_2 - \kappa) F_{11}}{2\lambda_2} \tag{E.67}$$

$$H_{10} = -\frac{(\lambda_2 - \kappa)E_{10} + (\lambda_2 + \kappa)F_{10}}{2\lambda_2} \tag{E.68}$$

$$H_{11} = -\frac{(\lambda_2 - \kappa)E_{11} + (\lambda_2 + \kappa)F_{11}}{2\lambda_2} \tag{E.69}$$

substitute into Eq. (E.8)

$$\begin{aligned} -\{&\rho_1\nu_1[2\kappa^2(A_{10} + B_{10}) + (\lambda_1^2 + \kappa^2)(C_{10} + D_{10})] \\ &- \rho_2\nu_2\big[2\kappa^2(E_{10}e^{\kappa z_L} + F_{10}e^{-\kappa z_L}) \\ &+ (\lambda_1^2 + \kappa^2)\big(G_{10}e^{\lambda_2 z_L} + H_{10}e^{\lambda_2 z_L}\big)\big]\}a_2 \\ &= \rho_1\nu_1[2\kappa^2(A_{11} + B_{11}) + (\lambda_1^2 + \kappa^2)(C_{11} + D_{11})] \\ &- \rho_2\nu_2\big[2\kappa^2(E_{11}e^{\kappa z_L} + F_{11}e^{-\kappa z_L}) \\ &+ (\lambda_1^2 + \kappa^2)\big(G_{11}e^{\lambda_2 z_L} + H_{11}e^{\lambda_2 z_L}\big)\big] \end{aligned} \tag{E.70}$$

a_2 can be expressed as:

$$a_2 = -\frac{\begin{matrix}\rho_1\nu_1[2\kappa^2(A_{11} + B_{11}) + (\lambda_1^2 + \kappa^2)(C_{11} + D_{11})] \\ -\rho_2\nu_2\big[2\kappa^2(E_{11}e^{\kappa z_L} + F_{11}e^{-\kappa z_L}) + (\lambda_1^2 + \kappa^2)\big(G_{11}e^{\lambda_2 z_L} + H_{11}e^{\lambda_2 z_L}\big)\big]\end{matrix}}{\begin{matrix}\rho_1\nu_1[2\kappa^2(A_{10} + B_{10}) + (\lambda_1^2 + \kappa^2)(C_{10} + D_{10})] \\ -\rho_2\nu_2[2\kappa^2(E_{10}e^{\kappa z_L} + F_{10}e^{-\kappa z_L}) + (\lambda_1^2 + \kappa^2)(G_{10}e^{\lambda_2 z_L} + H_{10}e^{\lambda_2 z_L})]\end{matrix}} \tag{E.71}$$

let,

$$a_2 = f(\kappa) \tag{E.72}$$

use Eq. (E.7)

$$
\begin{aligned}
M_1[A_{10}f(\kappa) + A_{11} - B_{10}f(\kappa) - B_{11}] \\
&- 2\rho_1\nu_1\lambda_1[C_{10}f(\kappa) + C_{11} - D_{10}f(\kappa) - D_{11}] \\
&+ (\rho_2 - \rho_1)gf(\kappa) \\
&= M_2\{[E_{10}f(\kappa) + E_{11}]e^{\kappa z_L} - [F_{10}f(\kappa) + F_{11}]e^{-\kappa z_L}\} \\
&- 2\rho_2\nu_2\lambda_2\{[G_{10}f(\kappa) + G_{11}]e^{\lambda_2 z_L} \\
&- [H_{10}f(\kappa) + H_{11}]e^{\lambda_2 z_L}\}
\end{aligned}
\tag{E.73}
$$

APPENDIX F: Coefficients Used in the Navier-Stokes Equation for N-layer Fluid System

The coefficients A_j, B_j, C_j, D_j, the amplitude of interface wave a_j and wave number κ can be solved from Eq. (F.1) to Eq. (F.10). As follows:

$$A_1 sinh\kappa h + B_1 cosh\kappa h + C_1 + D_1 exp(-\lambda_1 h) = -i\omega a_1 \tag{F.1}$$

$$M_1(A_1 cosh\kappa h + B_1 sinh\kappa h) - 2\rho_1 \nu_{e,1}\lambda_1[C_1 - D_1 exp(-\lambda_1 h)] = \rho_1 g a_1 \tag{F.2}$$

$$2A_1\kappa^2 sinh\kappa h + 2B_1\kappa^2 cosh\kappa h + (\lambda_1^2 + \kappa^2)[C_1 + D_1 exp(-\lambda_1 h)] = 0 \tag{F.3}$$

$$B_j + D_j + C_j\, exp(-\lambda_j d_j) = -i\omega a_{j+1} \tag{F.4}$$

$$A_{j+1} sinh\kappa d_{j+1} + B_{j+1} cosh\kappa d_{j+1} + C_{j+1} + D_{j+1} exp(-\lambda_{j+1} d_{j+1}) = B_j + D_j + C_j\, exp(-\lambda_j d_j) \tag{F.5}$$

$$\kappa A_{j+1} cosh\kappa d_{j+1} + \kappa B_{j+1} sinh\kappa d_{j+1} + C_{j+1}\lambda_{j+1} - D_{j+1}\lambda_{j+1} exp(-\lambda_{j+1} d_{j+1}) = \kappa A_j + C_j\lambda_j\, exp(-\lambda_j d_j) - \lambda_j D_j \tag{F.6}$$

$$M_j A_j - 2\rho_j \nu_{e,j} \lambda_j \left[C_j exp\left(-\lambda_j d_j\right) - D_j\right] = M_{j+1}\left(A_{j+1} cosh\kappa d_{j+1} + B_{j+1} sinh\kappa d_{j+1}\right) - 2\rho_{j+1}\nu_{e,j+1}\lambda_{j+1}\left[C_{j+1} - D_{j+1} exp\left(-\lambda_{j+1} d_{j+1}\right)\right] - \left(\rho_{j+1} - \rho_j\right) g a_{j+1} \quad \text{(F.7)}$$

$$\rho_j \nu_{e,j}\left\{2\kappa^2 B_j + \left(\lambda_j^2 + \kappa^2\right)\left[C_j exp\left(-\lambda_j h\right) + D_j\right]\right\} = \rho_{j+1}\nu_{e,j+1}\left\{2\kappa^2\left(A_{j+1} sinh\kappa d_{j+1} + B_{j+1} cosh\kappa d_{j+1}\right) + \left(\lambda_{j+1}^2 + \kappa^2\right)\left[C_{j+1} + D_{j+1} exp\left(-\lambda_{j+1} d_{j+1}\right)\right]\right\} \quad \text{(F.8)}$$

$$\kappa A_N - \lambda_N D_N + \lambda_N C_N exp(-\lambda_N d_N) = 0 \quad \text{(F.9)}$$

$$B_N + D_N + C_N exp(-\lambda_N d_N) = 0 \quad \text{(F.10)}$$

The seawater-liquefied soil system is meshed into N layer, where $j = 1$ for seawater, and $j = 2, \cdots, N$ for liquefied soil.

If $j \neq 1$ and $j \neq N$

For Eqs. (F.5) and (F.8), let

$$E1 = B_j + D_j + C_j\, exp\left(-\lambda_j d_j\right) \quad \text{(F.11)}$$

$$E2 = \rho_j \nu_j\left\{2\kappa^2 B_j + \left(\lambda_j^2 + \kappa^2\right)\left[C_j exp\left(-\lambda_j h\right) + D_j\right]\right\} \quad \text{(F.12)}$$

$$F_1 = A_{j+1} sinh\kappa d_{j+1} + B_{j+1} cosh\kappa d_{j+1} \quad \text{(F.13)}$$

Then,

$$F_1 + C_{j+1} + D_{j+1}exp\left(-\lambda_{j+1}d_{j+1}\right) = E1 \tag{F.14}$$

$$\rho_{j+1}\nu_{j+1}\left\{2\kappa^2 F_1 + \left(\lambda_{j+1}^2 + \kappa^2\right)\left[C_{j+1} + D_{j+1}exp\left(-\lambda_{j+1}d_{j+1}\right)\right]\right\} = E2 \tag{F.15}$$

(F.14) $\times\ \rho_{j+1}\nu_{j+1} \times 2\kappa^2$ −(F.15)

$$\begin{aligned}\rho_{j+1}\nu_{j+1}\left(\kappa^2 - \lambda_j^2\right)\left[C_{j+1} + D_{j+1}exp\left(-\lambda_{j+1}d_{j+1}\right)\right] \\ = 2\kappa^2\rho_{j+1}\nu_{j+1}E1 - E2\end{aligned} \tag{F.16}$$

$$C_{j+1} + D_{j+1}exp\left(-\lambda_{j+1}d_{j+1}\right) = \frac{2\kappa^2\rho_{j+1}\nu_{j+1}E1 - E2}{\rho_{j+1}\nu_{j+1}\left(\kappa^2 - \lambda_j^2\right)} \tag{F.17}$$

For Eqs. (F.6) and (F.7), Let

$$E3 = \kappa A_j + C_j\lambda_j\, exp\left(-\lambda_j d_j\right) - \lambda_j D_j \tag{F.18}$$

$$E4 = M_j A_j - 2\rho_j\nu_j\lambda_j\left[C_j exp\left(-\lambda_j d_j\right) - D_j\right] \tag{F.19}$$

$$F_2 = A_{j+1}cosh\kappa d_{j+1} + B_{j+1}sinh\kappa d_{j+1} \tag{F.20}$$

Then,

$$\kappa F_2 + C_{j+1}\lambda_{j+1} - D_{j+1}\lambda_{j+1}exp\left(-\lambda_{j+1}d_{j+1}\right) = E3 \tag{F.21}$$

$$\begin{aligned}M_{j+1}F_2 - 2\rho_{j+1}\nu_{j+1}\lambda_{j+1}\left[C_{j+1} - D_{j+1}exp\left(-\lambda_{j+1}d_{j+1}\right)\right] \\ - \left(\rho_{j+1} - \rho_j\right)ga_{j+1} = E4\end{aligned} \tag{F.22}$$

$M_{j+1} \times$ (F.21)$-\kappa \times$(F.22)

$$\begin{aligned}\left(\lambda_{j+1}M_{j+1}+2\kappa\rho_{j+1}v_{j+1}\lambda_{j+1}\right)\left[C_{j+1}-D_{j+1}exp\left(-\lambda_{j+1}d_{j+1}\right)\right]\\+\kappa\left(\rho_{j+1}-\rho_j\right)ga_{j+1}=M_{j+1}E3-\kappa E4\end{aligned}\tag{F.23}$$

$$C_{j+1}-D_{j+1}exp\left(-\lambda_{j+1}d_{j+1}\right)=\frac{M_{j+1}E3-\kappa E4-\kappa\left(\rho_{j+1}-\rho_j\right)ga_{j+1}}{\lambda_{j+1}M_{j+1}+2\kappa\rho_{j+1}v_{j+1}\lambda_{j+1}}\tag{F.24}$$

So far,

$$\begin{cases}C_{j+1}+D_{j+1}exp\left(-\lambda_{j+1}d_{j+1}\right)=\dfrac{2\kappa^2\rho_{j+1}v_{j+1}E1-E2}{\rho_{j+1}v_{j+1}\left(\kappa^2-\lambda_j^2\right)}\\C_{j+1}-D_{j+1}exp\left(-\lambda_{j+1}d_{j+1}\right)=\dfrac{M_{j+1}E3-\kappa E4-\kappa\left(\rho_{j+1}-\rho_j\right)ga_{j+1}}{\lambda_{j+1}M_{j+1}+2\kappa\rho_{j+1}v_{j+1}\lambda_{j+1}}\end{cases}\tag{F.25}$$

From Eq. (F.25), C_{j+1} and D_{j+1} can be expressed as

$$\begin{aligned}C_{j+1}=\frac{1}{2}\Bigg[&\frac{M_{j+1}E3-\kappa E4-\kappa\left(\rho_{j+1}-\rho_j\right)ga_{j+1}}{\lambda_{j+1}M_{j+1}+2\kappa\rho_{j+1}v_{j+1}\lambda_{j+1}}\\&+\frac{2\kappa^2\rho_{j+1}v_{j+1}E1-E2}{\rho_{j+1}v_{j+1}\left(\kappa^2-\lambda_j^2\right)}\Bigg]\end{aligned}\tag{F.26}$$

$$\begin{aligned}D_{j+1}=-\frac{1}{2exp\left(-\lambda_{j+1}d_{j+1}\right)}\Bigg[&\frac{M_{j+1}E3-\kappa E4-\kappa\left(\rho_{j+1}-\rho_j\right)ga_{j+1}}{\lambda_{j+1}M_{j+1}+2\kappa\rho_{j+1}v_{j+1}\lambda_{j+1}}\\&-\frac{2\kappa^2\rho_{j+1}v_{j+1}E1-E2}{\rho_{j+1}v_{j+1}\left(\kappa^2-\lambda_j^2\right)}\Bigg]\end{aligned}\tag{F.27}$$

For Eq. (F.28) and Eq. (F.29)

$$A_{j+1}sinh\kappa d_{j+1}+B_{j+1}cosh\kappa d_{j+1}+C_{j+1}+D_{j+1}exp\left(-\lambda_{j+1}d_{j+1}\right)=E1\tag{F.28}$$

$$\kappa A_{j+1} cosh\kappa d_{j+1} + \kappa B_{j+1} sinh\kappa d_{j+1} + C_{j+1}\lambda_{j+1} - D_{j+1}\lambda_{j+1} exp\left(-\lambda_{j+1} d_{j+1}\right) = E3 \tag{F.29}$$

$\kappa cosh\kappa d_{j+1}$ ×(F.28)− $sinh\kappa d_{j+1}$ ×(F.29)

Then

$$\kappa B_{j+1}\left(cosh^2\kappa d_{j+1} - sinh^2\kappa d_{j+1}\right) = G1_{j+1} \tag{F.30}$$

Let

$$G1_{j+1} = \kappa cosh\kappa d_{j+1} E1 - sinh\kappa d_{j+1} E3 - \left(\kappa cosh\kappa d_{j+1} - \lambda_{j+1} sinh\kappa d_{j+1}\right) C_{j+1} - \left(\kappa cosh\kappa d_{j+1} + \lambda_{j+1} sinh\kappa d_{j+1}\right) D_{j+1} exp\left(-\lambda_{j+1} d_{j+1}\right) \tag{F.31}$$

Note C_{j+1}, D_{j+1} has been expressed in terms of Ei_j $(i = 1\sim4)$.

$$B_{j+1} = \frac{G1_{j+1}}{\kappa\left(cosh^2\kappa d_{j+1} - sinh^2\kappa d_{j+1}\right)} \tag{F.32}$$

$\kappa sinh\kappa d_{j+1}$ ×(F.28)− $cosh\kappa d_{j+1}$ ×(F.29)

Then

$$\kappa A_{j+1}\left(sinh^2\kappa d_{j+1} - cosh^2\kappa d_{j+1}\right) = G2_{j+1} \tag{F.33}$$

Let

$$G2_{j+1} = \kappa sinh\kappa d_{j+1} E1 - cosh\kappa d_{j+1} E3 - \left(\kappa sinh\kappa d_{j+1} - \lambda_{j+1} cosh\kappa d_{j+1}\right) C_{j+1} - \left(\kappa sinh\kappa d_{j+1} + \lambda_{j+1} cosh\kappa d_{j+1}\right) D_{j+1} exp\left(-\lambda_{j+1} d_{j+1}\right) \tag{F.34}$$

$$A_{j+1} = \frac{G2_{j+1}}{\kappa\left(sinh^2\kappa d_{j+1} - cosh^2\kappa d_{j+1}\right)} \tag{F.35}$$

$$\begin{cases} A_{j+1} = \dfrac{G2_{j+1}}{\kappa\left(sinh^2\kappa d_{j+1} - cosh^2\kappa d_{j+1}\right)} \\ B_{j+1} = \dfrac{G1_{j+1}}{\kappa\left(cosh^2\kappa d_{j+1} - sinh^2\kappa d_{j+1}\right)} \end{cases} \tag{F.36}$$

So far, A_{j+1}, B_{j+1}, C_{j+1}, D_{j+1} are expressed in terms of Ei_j $(i = 1\sim4)$ and a_{j+1}, which in turn can be expressed by A_j, B_j, C_j, D_j, and a_{j+1}.

For the case of $N = 2$, $j = 1$, A_j, B_j, C_j, D_j can be expressed by a_{j+1} via the manipulation of Eq. (F.1)-(F.3) and (F.4). The additional equation of Eq. (F.9) and Eq. (F.10) can be used to 1) express wave number κ in terms of a_{j+1}; 2) another one non-linear equation, which includes only one unknown κ can be solved numerically.

If N>2, taking N=3 for example, since A_3, B_3, C_3, D_3 are expressed in terms of A_2, B_2, C_2, D_2, and a_3, the relationship between a_3 and a_2 must be constructed using the kinematic Eq. (F.4) on the interface between $j = 2$ and 3. Then condition at bottom, Eq. (F.9) and Eq. (F.10) can be used to express a_2 in terms of κ, and κ is solved.

Therefore, the following works need be done:

1) Express A_1, B_1, C_1, D_1;

2) Get the relationship between a_j and a_{j+1} (a_j is in terms of A_j, B_j, C_j, D_j);

3) When $j = N$, express a_N in terms of κ. As for the non-linear complex equation of κ, it is already in Eq. (F.9) and Eq. (F.10).

1) Express A_1, B_1, C_1, D_1

(F.3) $-2\kappa^2$ ×(F.1)

$$(\lambda_1^2 - \kappa^2)[C_1 + D_1 exp(-\lambda_1 d_1)] = i\omega a_1 2\kappa^2 \tag{F.37}$$

Since

$$(\lambda_1^2 - \kappa^2) = -i\omega v_1^{-1} \tag{F.38}$$

So

$$C_1 + D_1 exp(-\lambda_1 d_1) = -2\kappa^2 v_1 a_1 \tag{F.39}$$

(F.3) $-(\lambda_1^2 + \kappa^2)$ ×(F.1) gets

$$(\kappa^2 - \lambda_1^2)(A_1 sinh\kappa d_1 + B_1 cosh\kappa d_1) = (\kappa^2 + \lambda_1^2) i\omega a_1 \tag{F.40}$$

Then

$$A_1 sinh\kappa d_1 + B_1 cosh\kappa d_1 = (\kappa^2 + \lambda_1^2) v_1 a_1 \tag{F.41}$$

So

$$\begin{cases} A_1 = \dfrac{(\kappa^2 + \lambda_1^2) v_1 a_1 - B_1 cosh\kappa d_1}{sinh\kappa d_1} \\ C_1 = -2\kappa^2 v_1 a_1 - D_1 exp(-\lambda_1 d_1) \end{cases} \tag{F.42}$$

Substituting them into Eq. (F.2) and Eq. (F.4) results

$$M_1(sinh\kappa d_1 - coth\kappa d_1 cosh\kappa d_1)B_1 + 2\rho_1\nu_1\lambda_1 exp(-\lambda_1 h)D_1 = \rho_1 g a_1 - M_1\nu_1 a_1(\kappa^2 + \lambda_1^2)coth\kappa d_1 - 4\rho_1\nu_1^2\lambda_1 a_1\kappa^2 \quad \text{(F.43)}$$

$$B_1 + D_1[1 - exp(-2\lambda_1 d_1)] = \nu_1(\lambda_1^2 - \kappa^2)a_2 + 2\nu_1 a_1\kappa^2 exp(-\lambda_1 h) \quad \text{(F.44)}$$

$M_1(sinh\kappa d_1 - coth\kappa d_1 cosh\kappa d_1)$ ×Eq. (F.44) −(F.43)

$$D_1 = -\frac{\begin{matrix} M_1[2\nu_1 a_1\kappa^2 exp(-\lambda_1 d_1) - i\omega a_2] - 4\rho_1\nu_1^2\lambda_1\kappa^2 a_1 sinh\kappa d_1 \\ -M_1 cosh\kappa d_1(\lambda_1^2 + \kappa^2)\nu_1 a_1 + \rho_1 g a_1 sinh\kappa d_1 \end{matrix}}{M_1[1 - exp(-2\lambda_1 d_1)] + 4\rho_1\nu_1\lambda_1 sinh\kappa d_1 exp(-\lambda_1 d_1)} \quad \text{(F.45)}$$

$[1 - exp(-2\lambda_1 d_1)] \times$ (F. 43) $- 2\rho_1\nu_1\lambda_1 exp(-\lambda_1 h)$ ×(F.44)

$$B_1 = -\frac{\begin{matrix} [i\omega a_2 - 2\nu_1 a_1\kappa^2 exp(-\lambda_1 d_1)]4\rho_1\nu_1\lambda_1 sinh\kappa d_1 exp(-\lambda_1 d_1) \\ -[1 - exp(-2\lambda_1 d_1)] \\ \left[\begin{matrix} -4\rho_1\nu_1^2\lambda_1\kappa^2 a_1 sinh\kappa d_1 \\ -M_1 cosh\kappa d_1(\lambda_1^2 + \kappa^2)\nu_1 a_1 + \rho_1 g a_1 sinh\kappa d_1 \end{matrix}\right] \end{matrix}}{M_1[1 - exp(-2\lambda_1 d_1)] + 4\rho_1\nu_1\lambda_1 sinh\kappa d_1 exp(-\lambda_1 d_1)} \quad \text{(F.46)}$$

2) Relationship between a_j and a_{j+1}

From Eq. (F.4), yields

$$a_{j+1} = -\frac{B_j + D_j + C_j\, exp(-\lambda_j d_j)}{i\omega} \quad \text{(F.47)}$$

3) When $j = N$, express a_N in terms of κ

Since a_N appears in both C_N and D_N, manipulation can be used to retain only one of them to simplify the derivation.

(F.9) $-\lambda_N$ ×(F.10)

$$\kappa A_N - \lambda_N B_N - 2\lambda_N D_N = 0 \tag{F.48}$$

$N = j + 1$, so

$$A_N = \frac{G2_N}{\kappa(sinh^2\kappa d_N - cosh^2\kappa d_N)} \tag{F.49}$$

$$B_N = \frac{G1_N}{\kappa(cosh^2\kappa d_N - sinh^2\kappa d_N)} \tag{F.50}$$

$$D_N = -\frac{1}{2exp(-\lambda_N d_N)}\left[\frac{M_N E3_N - \kappa E4_N - \kappa(\rho_N - \rho_{N-1})ga_N}{\lambda_N M_N + 2\kappa\rho_N\nu_N\lambda_N} - \frac{2\kappa^2\rho_N\nu_N E1_N - E2_N}{\rho_N\nu_N(\kappa^2 - \lambda_N^2)}\right] \tag{F.51}$$

Substituting $A_N\ B_N\ D_N$ into Eq. (F.48) yields

$$\frac{G2_N}{sinh^2\kappa d_N - cosh^2\kappa d_N} - \frac{\lambda_N G1_N}{\kappa(cosh^2\kappa d_N - sinh^2\kappa d_N)} + \frac{\lambda_N}{exp(-\lambda_N d_N)}\left[\frac{M_N E3_N - \kappa E4_N}{\lambda_N M_N + 2\kappa\rho_N\nu_N\lambda_N} - \frac{2\kappa^2\rho_N\nu_N E1_N - E2_N}{\rho_N\nu_N(\kappa^2 - \lambda_N^2)}\right] - \frac{\lambda_N}{exp(-\lambda_N d_N)}\frac{\kappa(\rho_N - \rho_{N-1})g}{\lambda_N M_N + 2\kappa\rho_N\nu_N\lambda_N}a_N \tag{F.52}$$

Then

$$a_N = \frac{exp(-\lambda_N d_N)(M_N + 2\kappa\rho_N\nu_N)}{\kappa(\rho_N - \rho_{N-1})g}\left[\frac{G2_N}{sinh^2\kappa d_N - cosh^2\kappa d_N}\right.$$
$$\left. - \frac{\lambda_N G1_N}{\kappa(cosh^2\kappa d_N - sinh^2\kappa d_N)}\right] + \frac{M_N E3_N - \kappa E4_N}{\kappa(\rho_N - \rho_{N-1})g} \quad \text{(F.53)}$$
$$- \frac{\lambda_N(M_N + 2\kappa\rho_N\nu_N)(2\kappa^2\rho_N\nu_N E1_N - E2_N)}{\kappa(\rho_N - \rho_{N-1})g\rho_N\nu_N(\kappa^2 - \lambda_N^2)}$$

Eq. (F.10) is the target complex function. Its real and imaginary parts should satisfy the conditions:

$$real[B_N + D_N + C_N exp(-\lambda_N d_N)] = 0 \quad \text{(F.54)}$$

$$imag[B_N + D_N + C_N exp(-\lambda_N d_N)] = 0 \quad \text{(F.55)}$$

to solve the wave number κ.

References

Aydan, O. 1995. Mechanical and numerical modeling of lateral spreading of liquefied soil. *In: Proceedings of First International Conference on Earthquake Geotechnical Engineering, Tokyo, Japan***,** 881-887.

Biot, M. A. 1941. General theory of three-dimensional consolidation. *Journal of Applied Physics,* 12**,** 155-164.

Biot, M. A. 1956. Theory of propagation of elastic waves in a fluid-saturated porous solid. *Journal of the Acoustical Society of America,* 12**,** 168-178.

Bjerrum, J. 1973. Geotechnical problem involved in foundations of structures in the North Sea. *Geotechnique,* 23**,** 319–358.

Cheng, L., Sumer, B. M. & Fredsoe, J. 2001. Solution of pore pressure build up due to progressive waves. *International Journal for Numerical and Analytical Methods in Geomechanics,* 25**,** 885-907.

Dalrymple, R. A. & Liu, P. L. 1978. Waves over muds, a two-layer fluid model. *Journal Physical Oceanography,* 8**,** 1121–1131.

De Alba, P., Seed, H. & Chan, C. 1976. Sand liquefaction in large-scale simple shear tests. *Journal of Geotechnical Division, ASCE,* 102**,** 909-928.

Demars, K. R. & Vanover, E. A. 1985. Measurement of wave-induced pressures and stresses in a sand bed. *Marine Geotechnology,* 6**,** 29-59.

Farina, L. 2002. On ensemble prediction of ocean waves. *Tellus series a-dynamic meteorology and oceanography,* 54**,** 148-158.

Finn, W., Yogendrakumar, M., Ledbetter, R. & Yoshida, N. 1991. Analysis of liquefaction induced displacements. *In: Proceedings of 7th International Conference on Computer Methods and Advances in Geomechanics, Cairns, Australia***,** 913-921.

Gade, H. G. 1958. Effects of a non-rigid, impermeable bottom on plane surface waves in shallow water. *Journal Marine Research,* 16**,** 61-82.

Gatmiri, B. 1990. A simplified finite element analysis of wave-induced effective stress and pore pressures in permeable sea beds. *Geotechnique,* 40**,** 15-30.

Gomyo, M., Sakai, K., Takayama, T., Terauchi, K. & Takahashi, S. 1995. Site investigation on the stability of rubble-mound breakwaters. *Proceeding of Coastal Engineering, JSCE,* 42, No.2**,** 901-905.

Hamada, M. & Wakamatsu, K. 1998. Liquefaction-induced ground displacement triggered by quaywall movement. *Soils and Foundations,* 2**,** 85-96.

Hirt, C. W. & Nichols, B. D. 1981. Volume of fluid (VOF) method for the dynamics of free boundaries. *J. Comput. Phys.,* 39**,** 201-225.

Hoffschildt, M., Bidlot, J.-R., Hansen, B. & Janssen, P. a. E. M. 1999. Potential Benefit of Ensemble Forecasts for Ship Routing. *ECMWF Technical Memorandum no 287,* Reading, UK.

Hsu, J. R. C. 1990. Short-crested waves. *In Handbook of coastal and ocean engineering (ed. J. B. Herbich),* 1, chap. 3**,** 95-174.

Hsu, J. R. C., Jeng, D. S. & P., T. C. 1993. Short-crested wave-induced soil response in a porous seabed of infinite thickness. *International Journal of Numerical and Analytical Methods in Geomechanics,* 17**,** 553-576.

Huynh, N. T., M, I., T, K. & A, W. 1990. An experimental study on rheological properties of mud in the coastal waters. *Proc. Coastal Eng., JSCE,* 37**,** 225-229 (in Japanese).

Hwang, J.-I., Kim, C.-Y., Kim, M.-M. & Chung, C.-K. 2006. Viscous fluid characteristics of liquefied soils and behavior of piles subjected to flow of liquefied soils. *Soil Dynamics and Earthquake Engineering,* 26**,** 313-323.

Ishihara, K. & Yamazaki, A. 1984. Analysis of wave-induced liquefaction in seabed deposit of sand. *Soils Found,* 24**,** 85-100.

Janssen, P. a. E. M. 2000. Potential benefits of ensemble prediction of waves. *ECMWF Newsletter* 86**,** 3-6.

Jeng, D.-S. 2003. Wave-induced seafloor dynamics. *Appl. Mech. Rev.,* 56**,** 407-429.

Jeng, D.-S. 2008. Effects of Wave Non-Linearity on Residual Pore Pressures in Marine Sediments. *The Open Civil Engineering Journal,* 2**,** 63-74.

Jeng, D.-S. & Zhang, H. 2005. An integrated model for waveinduced seabed response in a three-dimensional domain II. *Ocean Engineering,* 32**,** 1950-1967.

Jeng, D. S. 1997. Wave-induced seabed instability in front of a breakwater. *Ocean Engineering,* 24**,** 887-917.

Jeng, D. S. & Cha, D. H. 2003. Effects of dynamic soil behaviour and wave nonlinearity on the wave-induced pore pressure and effective stresses in porous seabed. *Ocean Engineering,* 30**,** 2065-2089.

Jeng, D. S. & Hsu, J. R. C. 1996. Wave-induced soil response in a nearly saturated sea-bed of finite thickness. *Géotechnique,* 46**,** 427-440.

Jeng, D. S. & Lin, Y. S. 1996. Finite element modelling for water waves-seabed interaction. *Soil Dynamics and Earthquake Engineering,* 15**,** 283-300.

Jeng, D. S. & Lin, Y. S. 1997. Non-linear wave induced response of porous seabeds: A finite element analysis. *International Journal for Numerical and Analytical Methods in Geomechics,* 21**,** 15-42.

Jeng, D. S. & Lin, Y. S. 1999. Pore pressures on a submarine pipeline in a crossanisotropic non-homogeneous seabed under wave loading. *Canadian Geotechnical Journal,* 36**,** 563-572.

Jeng, D. S. & Rahman, M. S. 2001. Wave-induced oscillatory soil response: Difference between quasi-static and dynamic solutions. *Computer Methods and Advances in Geomechanics,A. A. Balkema,* 2**,** 1103-1106.

Jeng, D. S., Seymour, B., Gao, F. P. & Wu, Y. X. 2007a. Ocean waves propagating over a porous seabed: Residual and oscillatory mechanisms. *Science in China series e-technological sciences,* 50**,** 81-89.

Jeng, D. S., Seymour, B. R. & Li, J. 2007b. A new approximation for pore pressure accumulation in marine sediment due to water waves. *International Journal for numerical and analytical methods in Geomechanics,* 31**,** 53-69.

Jiang, Q. & Watanabe, A. 1995. Rheological properties of soft mud and a numerical model for its motion under waves. *Coastal Engineering in Japan, JSCE,* 38**,** 195-214.

Kessel, T. V. & Kranenburg, C. 1996. Gravity current of fluid mud on sloping bed. *Journal of Hydraulic Engineering, ASCE,* 122**,** 710-717.

Kioka, W., Hossain, M. & Kashihara, K. 1998. Long-period oscillations in a harbour with fluid mud bottom. *Proc. 26th Coastal Engineering Conf., ASCE,* Copenhagen 3**,** 3655–3667.

Lamb, H. 1932. Hydrodynamics. *Cambridge University Press***,** 738.

Lee, K. L. & Focht, J. A. 1975. Liquefaction potential at Ekofisk Tank in North Sea. *J. Geotechnical Engineering Division, ASCE,* No. 101**,** 1-18.

Li, X., Zhang, J. & Zhang, H. 2002. Instability of wave propagation in saturated poroelastoplastic media. *International Journal for Numeircal and Analytical methods in Geomechanics,* 26**,** 563-578.

Liu, H. & Jeng, D.-S. 2006. Response of a Porous Seabed Under Random Wave Loading. *ASME Conference Proceedings,* 2006**,** 85-93.

Liu, H. & Jeng, D.-S. 2007. A semi-analytical solution for random wave-induced soil response and seabed liquefaction in marine sediments. *Ocean Engineering,* 34**,** 1211-1224.

Liu, P. L. F. 1973. Damping of water waves over porous bed. *Journal of the Hydraulics Division, A.S.C.E,* 99**,** 2263-2271.

Liu, Z., Jeng, D. S., Chan, A. H. C. & Luan, M. 2009. Wave-induced progressive liquefaction in a poro-elastoplastic seabed: A two-layered model. *International Journal for numerical and analytical methods in Geomechanics,* 33**,** 591-610.

Longuet-Higgins, M. S. 1952. On the statistical distributions of the heights of sea waves. *J. Marine Res.,* 11**,** 245-265.

Maa, J. P.-Y. & Mehta, A. J. 1990. Soft mud response to water waves. *Journal of Waterway, Port, Coastal and Ocean Engineering,* ASCE 116.

Macpherson, H. 1980. The attenuation of water waves over a non-rigid bed *Journal of Fluid Mechanics,* 97**,** 721-742.

Madga, W. 1990. On one dimensional model of pore pressure generation in a highly saturated sandbed due to cyclic loading acting on a sand surface. I: Theoretical description and numerical approach. *Internal Report No. 5, SFB-205, TP A13,* Kusteningenieurwesen, University Hannover**,** 1-42.

Madsen, O. S. 1978. Wave-induced pore pressures and effective stresses in a porous bed. *Geotechnique,* 28, No. 4**,** 377-393.

Maeno, Y. & Hasegawa, T. 1987. In-situ measurements of wave-induced pore pressure for predicting properties of seabed deposits. *Coast. Eng. Japan,* 30**,** 99-115.

Maeno, Y., Sakai, T. & Mase, H. 1989. Influences of wave steepness on wave-induced liquefaction in sand layer. *Proc of 6th Symp on Coastal and Ocean Management. Coastal Zone,* 89**,** 3945-3957.

Maeno, Y. H. & Hasegawa, T. 1985. Evaluation of wave-induced pore pressure in sand layer by wave steepness. *Coastal Engineering in Japan,* 28**,** 31-44.

Mcdougal, W. G., Tsai, Y. T., Liu, P. L.-F. & Clukey, E. C. 1989. Wave-induced pore water pressure accumulation in marine soils. *Trans. ASME J. Offshore Mech. Arctic Eng,* 111**,** 1–11.

Mei, C. & Foda, M. 1981. Wave-induced response in a fluid-filled poro-elastic solid with a free surface-a boundary layer theory. *Geophys. J. R. Astron. Soc,* 66**,** 597-631.

Miyamoto, J., Sassa, S. & Sekiguchi, H. 2000. Wave-induced liquefaction and flow deformation in sand beds. *Proc. Coastal Engng,JSCE 47,* No. 2**,** 921–925.

Miyamoto, J., Sassa, S. & Sekiguchi, H. 2004. Progressive solidification of a liquefied sand layer during continued wave loading. *Géotechnique,* 54**,** 617-629.

Montassar, S. & Buhan, D. P. 2006. A numerical model to investigate the effects of propagating liquefied soils on structures. *Computers and Geotechnics,* 33**,** 108-120.

Moshagen, H. & Torum, A. 1975. Wave induced pressures in permeable seabeds. *Journal ofWaterways, Harbour and Coastal Engineering Division, A.S.C.E,* 101**,** 49-57.

Nago, H., Maeno, S. & Matsumoto, T. 1993. Liquefaction and densification of loosely deposited sand bed under wave pressure variation. *International Offshore and Polar Engineering Conference, Singapore***,** 578–584.

Nakamura, H., Onishi, R. & Minamide, H. 1973. On the seepage in the seabed due to waves. *Proceedings of 20th Coastal Engineering Conference, J.S.C.E***,** 421-428.

Nataraja, M. & Gill, H. 1983. Ocean wave-induced liquefaction analysis. *J. Geotech. Eng. Div.. Am. Soc. Civ. Eng,* 109**,** 573–590.

Nataraja, M., Singh, H. & Maloney, D. 1980. Ocean wave-induced liquefaction analysis: a simplified procedure. *Proc of Int Symp on Soils under Cyclic and Transient Loadings.***,** 509-516.

Okusa, S. 1985. Wave-induced stress in unsaturated submarine sediments. *Geotechnique,* 35**,** 517–532.

Oveisy, A., Hall, K., Soltanpour, M. & Shibayama, T. 2009. A two-dimensional horizontal wave propagation and mud mass transport model. *Continental Shelf Research,* 29**,** 652-665.

Phillips, R. & Sekiguchi, H. 1992. Generation of water wave trains in drum centrifuge. *Proceedings of International Symposium on Technology in Ocean Engineering (Techno-Ocean' 92),* 1**,** 29-34.

Prevost, J. H., Eide, O. A. & Anderson, K. H. 1975. Discussion on "Wave induced pressures in permeable seabeds". *101,* 1**,** 464-465.

Putnam, J. A. 1949. Loss of wave energy due to percolation in a permeable sea bottom. *Transactions, American Geophysical Union,* 30**,** 349-356.

Rahman, M. 1991. Wave-induced instability of seabed: Mechanism and conditions. *Mar. Geotech,* 10.

Rahman, M. S., El-Zahaby, K. & Booker, J. 1994. A semi-analytical method for the wave-induced seabed response. *International Journal for Numerical and Analytical Methods in Geomechanics,* 26**,** 213-236.

Rumer, R. R. 1969. Resistance to flow through porous media. *Flow through porous media (ed. R. J. M. De Wiest)***,** 91-108.

Sakai, T. 1999. Introduction to wave-seabed interaction. *New Coastal Engineering in Global Environment***,** 357-358.

Sakai, T., Hatanaka, K. & Mase, H. 1992. Wave-induced effective stress in seabed and its momentary liquefaction. *J. Waterw., Port, Coastal, Ocean Eng,* 118**,** 202-206.

Sakakiyama, T. & Bijker, E. W. 1988. Mass transport velocity in mud layer due to progressive waves. *Coastal and Ocean Eng., ASCE,* 115**,** 614-633.

Sassa, S., Miyamoto, J. & Sekiguchi, H. 2003. The dynamics of liquefied sediment flow undergoing progressive solidification. *Advances in Natural and Technological Hazards Research,* 19**,** 95-102.

Sassa, S. & Sekiguchi, H. 1999. Wave-induced liquefaction of beds of sand in a centrifuge. *Geotechnique,* 49**,** 621-638.

Sassa, S. & Sekiguchi, H. 2001. Analysis of wave-induced liquefaction of sand beds. *Geotechnique,* 51**,** 115-126.

Sassa, S., Sekiguchi, H. & Miyamoto, J. 2001. Analysis of progressive liquefaction as a moving-boundary problem. *Geotechnique,* 51**,** 847-857.

Sawicki, A. & Mierczyński, J. 2009. On the behaviour of liquefied soil. *Computers and Geotechnics,* 36**,** 531-536.

Seed, H. B. & Rahman, M. S. 1978. Wave-induced pore pressure in relation to ocean floor stability of cohesionless soil. *Mar. Geotechnol,* 3**,** 123-150.

Sekiguchi, H., Kita, K. & Okamoto, O. 1995. Response of poro-elastoplastic beds to standing waves. *Soils and Foundations,* 35**,** 31-42.

Sekiguchi, H. & Phillips, R. 1991. Generation of water waves in a drum centrifuge. *Proceedings of the International Conference Centrifuge***,** 343-350.

Shibayama, T., An, N.N 1993. A visco-elastic–plastic model for wave-mud interaction. *Coastal Engineering in Japan,* 36**,** 67–89.

Shibayama, T., Aoki, T. & Sato, S. 1989. Mud mass transport rate due to waves: A visco-elastic model. *Proc. of 23rd IAHR.*

Sleath, J. F. A. 1970. Wave-induced pressures in beds of sand. *Journal of Hydraulics Division, A.S.C.E.,* 96**,** 367-378.

Soltanpour, M. & Samsami, F. 2011. A comparative study on the rheology and wave dissipation of kaolinite and natural Hendijan Coast mud, the Persian Gulf. *Ocean Dynamics,* 61**,** 295-309.

Sumer, B. M. 2005. Liquefaction around marine structures. *LIMAS, an EU research program Hydrodynamics VI : theory and applications, proceedings of the 6th International Conference on Hydrodynamics***,** 15-19.

Sumer, B. M., Fredsøe, J., Christensen, S. & Lind, M. T. 1999. Sinking/floatation of pipelines and other objects in liquefied soil under waves. *Coastal Engineering,* 38**,** 53-90.

Sumer, B. M., Hatipoglu, F., Fredsøe, J. & Hansen, N.-E. O. 2004. Floatation of pipelines in soils liquefied by waves. *Report.*

Sumer, B. M., Hatipoglu., F., Fredsøe., J. & Hansen, N.-E. O. 2006. Critical Flotation Density of Pipelines in Soils Liquefied by Waves and Density of Liquefied Soils. *Journal of waterway, Port, Coastal, and Ocean Engineering, ASCE,* 132**,** 252-265.

Takahashi, S., Shimosako, K., Yamamoto, K. & Miura, H. 1994. Small-scale experiments on a boiling sand bed and its wave absorbing effects. *Proc. Coastal Engng, JSCE* 41**,** 611-615.

Tayfun, M. A. 1981. Distribution of crest-to-trough wave height. *Port, Coast. and Oc. Eng., ASCE,* 107**,** 149-156.

Teh, T. C., Palmer, A. C. & Damgaard, J. S. 2003. Experimental study of marine pipelines on unstable and liquefied seabed. *Coastal Eng.,* 50.

Thomas, S. D. 1995. A finite element model for the analysis of wave-induced stresses, displacements and pore pressure in an ansaturated seabed. II: Model Verification. *Computers and Geotechnics,* 17**,** 107-132.

Ting, F. C. K. 1992. On forced internal waves in a rectangular trench. *Journal of Fluid Mechanics,* 235**,** 255-283.

Towhata, I., Orense, R. & Toyota, H. 1999. Mathematical principles in prediction of lateral ground displacement induced by seismic liquefaction. *Soils Foundat,* 39**,** 1-19.

Tsai, C. P. 1995. Wave-induced liquefaction potential in a porous seabed in front of a breakwater. *Ocean Engineering,* 22**,** 1-18.

Tsotsos, S., Georgiadis, M. & Damaskindou, A. 1989. Numerical analysis of liquefaction potential of partially drained seafloor. *Coastal Eng,* 13**,** 117-128.

Tsui, Y. T. & Helfrich, S. C. 1983. Wave-induced pore pressures in submerged sand layer. *Journal of Geotechnical Engineering, A.S.C.E.,* 109**,** 603-618.

Tsuruya, H., Nakano, S. & Takahama, J. 1987. Interaction between surface waves and a multi-layered mud bed. *Rep. No. 5, Port and Harbor Research Institute, Ministry of Transport, Japan.*

Tzang, S. Y. 1992. Water wave-induced soil fluidization in a cohesionless fine-grained seabed. *PhD Dissertation, University of California at Berkeley***,** 137.

Umehara, Y., Zen, K. & Hamada, K. 1985. Evaluation of soil liquefaction potentials in partially drained conditions. *Soils Found,* 25**,** 57-72.

Uzuoka, R., Yashima, A., Kawakami, T. & Konrad, J.-M. 1998. Fluid dynamics based prediction of liquefaction induced lateral spreading. *Computers and Geotechnics,* 22**,** 243-82.

Verruijt, A. 1969. Elastic storage of aquifers. *Flow Through Porous Media,* (Ed. De Wiest, R. J. M.), Academic Press, New York**,** 331-376.

Walter, H. M. 1968. Sea spectra simplified. *dissertation*.

Wang, Z., Luan, M., Liu, Z. & Wang, D. 2005. Numerical analysis of dynamic response of seabed under random wave loading. *Frontiers in Offshore Geotechnics: ISFOG 2005,* Taylor & Francis, London**,** 589–594.

Yamamoto, T., Koning, H. L., Sellmeijer, H. & Hijum, E. V. 1978. On the response of a poro-elastic bed to water waves. *Journal of Fluid Mechanics,* 87**,** 193-206.

Yamamoto, T. & Takahashi, S. 1985. Wave damping by soil motion. *Journal Water-way, Port, Coastal and Ocean Engineering, ASCE,* 110**,** 62-77.

Yang, Q. S. & Poorooshasb, H. B. 1997. Seabed response to wave loading. *International Offshore and Polar Engineering Conference, Honolulu,* 1**,** 689-695.

Zen, K., H, Yamazaki & Lee, I. H. 1991. wave-induced liquefaction and instability of breakwaters. *Proc. Int. Symp. Geo-coast'91, Yokohama,* 1**,** 673-678.

Zen, K. & Yamazaki, H. 1990. Mechanism of wave-induced liquefaction and densification in seabed. *Soils Found,* 30**,** 90–104.

Zhang, D. & Ng, C. 2006. A Numerical Study on Wave-Mud Interaction. *China Ocean Engineering,* 20**,** 383-394.

Zhang, H. & Jeng, D.-S. 2005. An integrated model for wave-induced seabed response in a three-dimensional domain I. *Ocean Engineering,* 32**,** 701-729.

Zhang, Q. & Zhao, Z. 1999. Wave-mud interaction: wave attenuation and mud mass transport. *Coast Sed,* 99**,** 1867-1880.

Zienkiewicz, O. C., Chang, C. T. & Bettess, P. 1980. Drained, undrained, consolidating and dynamic behavior assumptions in soils. *Geotechnique,* 30**,** 385-395.